Atom Trap Trace Analysis of ^{39}Ar

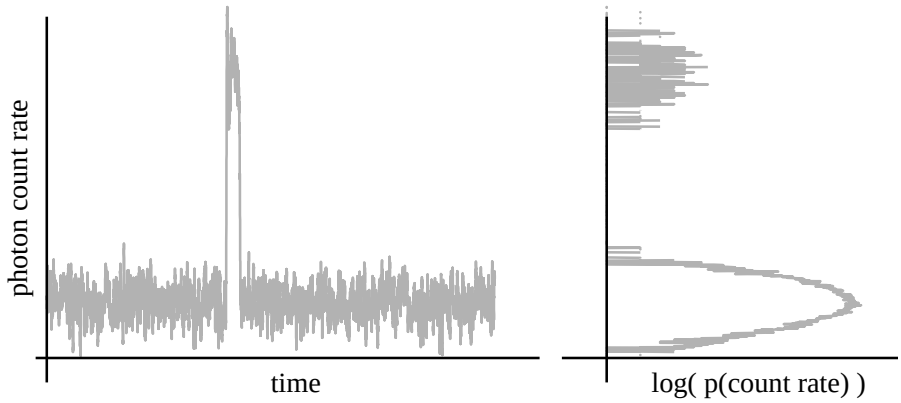

Joachim Welte

Issued 2011

Dissertation

submitted to the

Combined Faculties of the Natural Sciences and Mathematics

of the Ruperto-Carola-University of Heidelberg, Germany

for the degree of

Doctor of Natural Sciences

Put forward by

Joachim Welte

born in: Karlsruhe, Germany

Oral examination: December 14, 2011

Atom Trap Trace Analysis of ^{39}Ar

Referees: Prof. Dr. Markus K. Oberthaler
Prof. Dr. Werner Aeschbach-Hertig

Entwurf und Umsetzung eines Systems zum Einzelatomnachweis von Argon-39

Der Nachweis von ^{39}Ar in natürlichen Wasserproben kann zur radiometrischen Altersbestimmung auf Zeitskalen von 50 bis 1000 Jahren vor heute verwendet werden [1]. Diese experimentelle Forschungsarbeit stellt den Aufbau einer Atomstrahl- und Fallenapparatur vor, welche ^{39}Ar-Atome mittels der laserkühlungsbasierten Methode "Atom Trap Trace Analysis" ([2]) einfängt und nachweist. Auf diese Art könnten die bestehenden Beschränkungen des indirekten Nachweises über Zerfallsprodukte ("low-level counting", [3]) bezüglich Probengröße und Messdauer aufgehoben werden.
Im Rahmen dieser Arbeit wurde das Hyperfeinstrukturspektrum des Kühlübergangs $1s_5$-$2p_9$ experimentell bestimmt. Desweiteren wurde ein optisch kollimierter, hochintensiver Strahl kalter metatabiler Argonatome erzeugt und der Nachweis einzelner ^{39}Ar-Atome über Fluoreszenzmessung realisiert.
Bislang wurden ^{39}Ar-Zählraten von 1 Atom in ungefähr 4 Stunden für atmosphärisches Argon erreicht. Neueste Verbesserungen deuten außerdem darauf hin, dass Zählraten von 1 Atom/h möglich sind.

Design and realization of a detection system for single argon-39 atoms

Detection of ^{39}Ar in natural water samples can be employed for radiometric dating on a timescale of 50 to 1000 years before present [1]. This experimental work comprises the setup of an atomic beam and trap apparatus that captures and detects ^{39}Ar atoms by the laser-cooling technique "Atom Trap Trace Analysis" ([2]). With this approach, the limitations of low-level counting [3], regarding sample size and measurement time, could be overcome.
In the course of this work, the hyperfine structure spectrum of the cooling transition $1s_5$-$2p_9$ has been experimentally determined. A high intensity, optically collimated beam of slow metastable argon atoms has been set up and fluorescence detection of individual ^{39}Ar atoms in a magneto-optical trap is realized.
^{39}Ar count rates of 1 atom in about 4 hours have been achieved for atmospheric argon. Recent improvements further suggest that even higher count rates of 1 atom/hour are within reach.

Contents

Preface

The following work condenses what I (and my colleagues) have been working on during the last couple of years. First, as a diploma student, doing preliminary measurements on the former argon beam machine and later, setting up the new experiment which is presented in the following.
The first chapter is dedicated to a general introduction and motivation of the thesis topic. The age of a water sample is defined and several methods for its determination are described. Their applicability to different water systems and different time scales is discussed and specific focus is put on dating of groundwater with ^{39}Ar. Basic information on argon is provided, and the requirements for a successful realization of ^{39}Ar atom trap trace analysis are discussed.
Chapter 2 summarizes the work done to determine the hyperfine structure spectrum of the designated cooling transition in ^{39}Ar. In order to measure this spectrum, Doppler-free saturation spectroscopy was performed in an enriched sample. 40 spectral lines were observed, most of which were identified with cross-over transitions between several atomic resonances. This dataset served to derive the hyperfine constants of the lower and the upper hyperfine multiplet and the -mainly mass induced- isotopic shift.
The third chapter then describes the setup of the laser system. In each stage of the apparatus several repumper frequencies have to be provided for efficient manipulation of ^{39}Ar. Although, σ-polarized light is used to pump atoms between stretched magnetic states, polarization imperfections prevent the transitions from being perfectly closed. The repumper sidebands are generated according to the results from the previous chapter. Self-built tapered amplifier diode lasers are used to provide the necessary laser power.
In Chapter 4, the atomic beam apparatus is described in detail together with results from calculations and measurements for each stage. A vacuum system has been set up that maintains different pressures in different parts of the experiment. It can be divided in 5 parts: sample reservoir, metastable atom beam source, transversal collimation stage, longitudinal slower, and magneto-optical trap.
The fifth chapter summarizes calculations and results related to single atom detection. Fluorescence light from the magneto-optical trap is imaged onto a detector and single atoms can be identified by discrete steps in the detector signal level. In order to realize this, a high-NA objective has been designed and built, and stray light suppression methods were implemented. Results from ^{39}Ar measurements are presented and its detection serves for optimization of the apparatus.
In the last chapter, the results are summarized. As still some work needs to be done, several improvements are suggested.
The appendix compiles constants, symbols, and formulae used for the various calculations throughout the whole thesis.

Acknowledgments

As always in experimental physics I am not the only one deeply committed to this project. All those people, colleagues, friends and also competitors contributed much to the achievements made. Thus, I whole-heartedly acknowledge their work.
This project would not have been possible without the commitment of both Prof. Markus K. Oberthaler and Prof. Werner Aeschbach-Hertig.
Markus, as my direct supervisor, provided a lot of input from the atom optical side. Either in countless discussions or with helpful passing remarks. Even though the motivation might drop sometimes, he always finds the right words to keep things going. I consider myself lucky to have had the opportunity to work in his group. Danke!
Werner, on the other side of the Heidelberg ATTA collaboration, always had an open ear for all kinds of questions related to environmental physics, the groundwater dating community and possible applications of ^{39}Ar-dating. And, furthermore, he contributes equally to this project by supervising the set-up of the degassing/purification system. Danke!
But, being frank, the largest tribute is due to my dear former diploma student (and since quite a while PhD colleague) and friend Florian Ritterbusch. Without him, we would not be where we are now. And, on a very personal level, I would have probably starved or gotten seriously ill due to malnutrition. Vielen Dank!
Again, on the other side of the collaboration, Thomas Reichelt does a great job with the degassing and purification system. Hopefully soon, we will be able to actually merge our expertises by measuring real samples. And, again from a very personal perspective, I really enjoyed our conference bicycle trip along the Côte d'Azur. Auch Dir vielen Dank!
During the course of our experimental set-up several diploma students largely contributed to the ongoing progress of this experiment. First, Anna Wonneberger started to work on novel methods of water sample preparation for ATTA. Danke!
Isabelle Steinke did a great job with the ^{39}Ar spectroscopy. Danke!
Matthias Henrich designed and built most of the laser system. Great job! Besides this, he is a good friend and agreed to proof-read my thesis. Vielen Dank für alles! And, never forget: "Up and atom."
Christoph Kaup is still traveling around (the world?) after having wound and Monte-Carlo-simulated the Zeeman slower and counted countless single atoms. Rest assured, I envy you! Auf jeden Fall, danke für Deine Mitarbeit!
Gong Cheng did a fine job during his two months of exchange here in Heidelberg. Thank you, and maybe we will meet in Hefei.
I would also like to thank Fabienne Haupert. Not only for being a true friend, but also for countless discussions on physics and private matters, all the lunch breaks,... to keep it short: just for being there. Danke.
Jiří Tomkovič: we fought our battles (mostly with the purpose of scientific progress, but still...), we suffered together, and still we're friends. Vielen Dank.
Christian Gross: I certainly have to thank for quite some scientific input, but also for being

on the other end of the rope and belaying me. And -not to be forgotten- always pushing the limit further...Danke.
Jürgen Schölles has guided me by with patience, inspiration and solutions. On the professional level mostly related to electronics but on the personal level for introducing me to yoga and having a sympathetic ear. Namasté.
Furthermore, I would like to thank all other members of the Matterwave group that I got to know during the course of my PhD, extra thanks go to Philippe Bräunig for proof reading.
Winfried Schwarz and Mario Trieloff provided us with enriched samples for spectroscopy and optimization of the apparatus. Vielen Dank!
Werner Lamade and the rest of the fine-mechanical workshop of the KIP: For finding well-suited solutions for all the mechanical problems and always facing the physicists' stubbornness. Danke!
All other service units at the Kirchhoff Institute for Physics.
Ursula Scheurich from the glass workshop, who produced countless source tubes in different geometries. Danke hierfür!
I further gratefully acknowledge financial support from the "Landesstiftung Baden-Württemberg", the "Deutsche Forschungsgemeinschaft (DFG)" and the "Landesgraduiertenförderung Baden-Württemberg".
The "Heidelberg Graduate School for Fundamental Physics" has always provided an excellent platform for scientific exchange. I am happy that I could contribute as a student representative. Thanks to all academic members and especially all members of the Central Office. I wish all the best and that the application for extension might be successful.
Liebe Eltern, liebe Schwestern, ich möchte Euch einfach dafür danken, wie sehr Ihr mich auf meinen bisherigen Weg unterstützt habt.
Liebe Freunde, dafür danke ich Euch natürlich auch. Und vor allem auch dafür, dass Ihr es mir bislang nicht zu übel genommen habt, wenn ich mich mal wieder monatelang mit Verweis auf meine ach so wichtige Tätigkeit nicht gemeldet habe. Die kommenden Jahre werden ja vielleicht etwas entspannter.
Liebe Susanne, ich freue mich immer wieder darüber, dass die Dinge zwischen uns so sind, wie sie sind...

1. Introduction

The evolution of the human race and mankind's continued existence on earth strongly depend on influences from all spheres of the natural environment. However, the natural environment does not only exert influence. Rather, both mankind and environment are intertwined by mutual influence.
Climate on earth is one of the most powerful mechanisms governing the prosperity of all highly developed life forms. But, the ever-ongoing climate change is predicted to have serious consequences in the near future. Increasing mean surface temperatures will most probably gravely change the face of the earth, especially regarding the distribution of freshwater [4].
Furthermore, the growth of world population and steadily increasing water demand per capita will drastically reduce freshwater availability in the next decades [5]. Therefore, water management and especially groundwater management will become more and more important in the course of this century. But already nowadays, clean water can be effectively regarded as one of world's most precious resources.
Besides this striking connection between mankind and the hydrosphere, there are several others which are not that obvious. The ocean, for example, serves as buffer for huge amounts of CO_2 which would otherwise remain in the atmosphere and could further enhance climate change by the greenhouse effect. Hence, the full impact of industrialization and the release of large quantities of formerly fossil carbon will probably be delayed or smoothed out by the mean ocean circulation time [6].
Also, aquatic archives such as groundwater and ice can provide valuable insights into the past, present and future development of climate. Successfully reconstructed paleoclimate information can be used to motivate, support and validate models of the processes behind climate change. These models may then indicate potential climate control levers.
In order to get a grasp of the complexity of these interactions, the hydrological cycle has to be well understood. In this context the issue of determining "water ages" arises, where "age" refers to the time elapsed since last equilibration with the atmosphere. It is of interest as most aquatic systems have spatially and temporarily varying composition which can be due to changing environmental conditions such as pressure, temperature, pH, chemical reactions (in the water, in the surrounding rock or between water and rock), and physical processes like e.g. fractionation or radioactivity.
For the case of the above-mentioned paleoclimate reconstruction with water archives, isotopes with known production rates, input functions and decay mechanisms are well-suited for age determination. However, there is only a limited number of isotopes available for practical dating purposes. Of these, radioisotopes provide the most reliable results. But, since half-lives have to match the time scale of the processes to be observed (fig. 1.1, [7, 8]) and concentrations have to be in a detectable range (compare fig. 1.2) each radioisotope is applicable only to a limited time span.
The most recent decades of human influence on the environment are covered by several

anthropogenically produced radioisotopes and instable molecules as can be seen in fig. 1.1. For the time range from about 30.000 years BP[1] to 1000 years BP the radiocarbon method is mostly applied for dating. In between, from about 1000 years BP to the 1950s, there is a "dating-gap" that can be bridged by one and only one isotope so far, namely ^{39}Ar, given the need for quantitative results. ^{32}Si also covers this period of time, but as silicon is omnipresent both in atmosphere (dust particles) and in aquifers reliable water ages can hardly be derived.

^{39}Ar is an isotope of the atmosphere's third most abundant component[2], the noble gas argon. It decays with a half-life of 269 years and has a natural abundance of $8.5 \cdot 10^{-16}$ upon total atmospheric argon. Chemical inertness, only few subterranean sources and insensitivity to human influence make ^{39}Ar an ideal conservative tracer.

The major limitation in the wide application of ^{39}Ar-dating is its low concentration, which severely complicates its detection. Nevertheless, it has been detected in natural water samples with different methods ([3, 9]). However, all these methods incorporate very involved experimental effort, large sample sizes, or long measurement times up to several weeks. Thus, ^{39}Ar-dating has not yet unfolded its full potential as a standard dating technique.

Groundwater dating with ^{39}Ar has first been proposed in 1968 by H.H. Loosli and H. Oeschger, both pioneers in the field of environmental physics [1]. 7 years later, in 1975, ice core ages proved that a dating method with ^{39}Ar can actually yield age information. Successful low level counting measurements with groundwater [10] and ocean water [11] followed shortly thereafter. Since then, numerous measurements of ^{39}Ar ages have been conducted at the facility in Bern.

In the course of the experimental work underlying this thesis, a detection scheme for rare isotopes based on the excellent isotopic selectivity of laser transitions is employed for the radioactive isotope ^{39}Ar. This relatively new approach called "Atom Trap Trace Analysis" (ATTA) has first been realized for krypton isotopes (^{81}Kr and ^{85}Kr) at the "Argonne National Laboratory" in Argonne/USA [2]. Currently, several more krypton ATTA experiments are in progress.

A further ATTA apparatus for radiokrypton dating is being set-up at the "National Laboratory for Physical Sciences at the Microscale" in Hefei/China. The experiment at the "Centre for Science and Peace Research" in Hamburg/Germany focuses on the detection of ^{85}Kr for monitoring purposes in the framework of the "Non-Proliferation Treaty". Experiments at the Columbia University/New York City and the Union College in Schenectady/USA aim for the detection of ^{85}Kr in purified Xe, which is employed in dark matter detectors. ATTA has also been implemented for ^{41}Ca [12, 13] but has not yet reached natural abundance level.

However, relative ^{39}Ar abundances are by orders of magnitude lower than those of the afore mentioned isotopes and thus require a significantly enhanced overall detection performance. This demanding experimental challenge of successfully detecting ^{39}Ar at natural levels is addressed in the following. Yet, it has to be mentioned that the group at ANL recently also achieved detection of ^{39}Ar at natural abundance with a count rate of 13 atoms in 60 hours [14].

On the one hand the study will briefly illustrate the background in environmental physics to which this work is directly related. On the other hand, detailed insights will be given into the setup of the experimental apparatus. Additionally, it comprises investigations on

[1] BP: before present

[2] Depending on the geographical location, water vapor might be more abundant than argon.

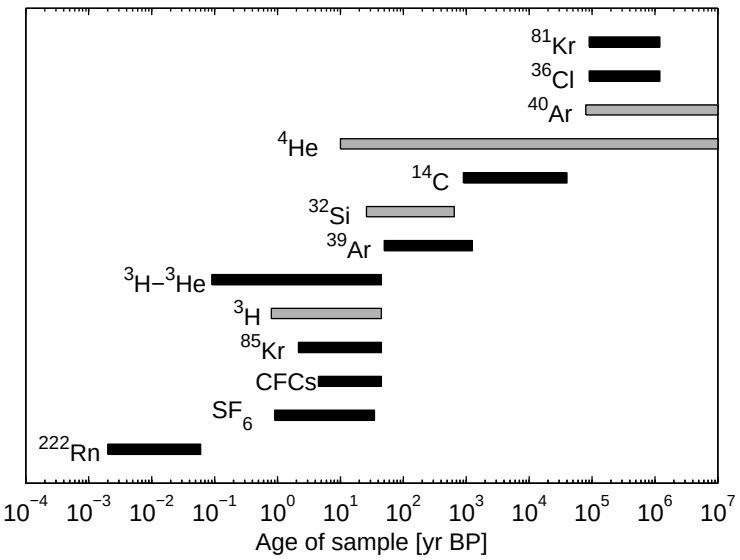

Figure 1.1.: Dating ranges of different isotopes. The time is given in years before present. Black color indicates reliable dating whereas gray color indicates less reliability.

the hyperfine structure of the destined cooling transition in ^{39}Ar, which is mandatory for efficient laser cooling.
In order to achieve maximum efficiency, the optimum implementation of each step of the setup has to be found. For obvious reasons, all parameters have to be in an experimentally accessible range, hence extensive calculations are required and are presented in the corresponding sections. The data obtained from the experiment is discussed on the basis of these calculations and provides an estimation of the expected detection efficiency, sample size and detection time.
The apparatus features an efficient source for metastable atoms, a two dimensional collimation stage, a 2D magneto-optical lens, a longitudinal Zeeman slower, and a magneto-optical trap with fluorescence detection on the single atom level, which are all described in detail in separate sections. Further information is provided on the setup of a high power laser system for the generation and amplification of the necessary sidebands.

1.1. Dating with environmental radioisotopes

1.1.1. Isotopes and dating mechanisms

Mostly, once the relative concentration of a certain isotope has been measured, the age can be reconstructed by one specific method, depending on the isotope used. Here, only those isotopes and methods applicable to water samples are discussed.
For isotopes with known initial concentration c_0 and half-life $T_{1/2}$, and no or negligible sources in the water reservoir (aquifer, ice, meromictic lake) the age t can be reconstructed from the radioactive decay curve:

$$c(t) = c_0 \cdot e^{-\frac{\ln(2)\cdot t}{T_{1/2}}} \Rightarrow t = \ln\left(\frac{c_0}{c(t)}\right) \cdot \frac{T_{1/2}}{\ln 2}. \tag{1.1}$$

This applies to ^{39}Ar as well as to ^{14}C, ^{32}Si, ^{36}Cl, ^{81}Kr and ^{222}Rn. As the ^{3}H concentration did not increase monotonically (there was the prominent "bomb peak" in the mid-sixties), simple reconstruction from radioactive decay does not work for this tracer.
However, given the known input function, ^{3}H dating can still work to some extent. This also applies to tracers such as ^{85}Kr, SF_6 and CFCs.
Another work-around for ^{3}H dating is ^{3}H-^{3}He dating. Tritium and stable ^{3}He form a mother-daughter pair and ages can be determined from the ratio between these isotopes. Still, it has to be admitted that there are subterranean sources for ^{3}He, so additional measurements are needed to identify the tritiogenic ^{3}He component [15].
Tracers such as ^{4}He and ^{40}Ar accumulate in the groundwater by decay series in the aquifer material. ^{4}He is produced in the U/Th decay series and ^{40}Ar is the stable product of ^{40}K decay. Given the long lifetimes of the mother isotopes (^{230}Th: 75380 a, ^{40}K: 1.27 Ga), the production rate is quasi-constant. Hence, these isotopes accumulate linearly over time. Still, the production rate has to be determined which renders these methods problematic.
As already mentioned, the time span of 50 BP to 1000 BP is of special interest as it covers phenomena such as industrialization, growing human population, climate change, and the "little ice age" between 1550 AD and 1850 AD. Fig. 1.1 indicates that three isotopes can be applied, namely ^{32}Si, ^{4}He and ^{39}Ar. Of those only ^{39}Ar provides reliable results.
The shortcomings of ^{4}He have been discussed. ^{32}Si has another important deficit besides of being omnipresent in aquifers: Its half-life is not known very accurately [16, 17]. Early estimates ranged around $300-600$ years while recent data suggests $132-178$ years [18, 19]. Hence, ^{39}Ar dating really is the only applicable technique in this period.

1.1.2. Existing detection techniques

Detection of ^{39}Ar at atmospheric concentration has already been accomplished and used for water dating by the use of two methods. Low level counting (LLC) has been performed in the underground laboratory of the university of Bern/Switzerland since the mid-seventies of last century [3]. This radiometric method counts the ^{39}Ar activity in extracted gas samples.
Although the method itself works well, there are two major drawbacks in application. Firstly, as the decays of ^{39}Ar are counted in a proportional counter, any background from other radionuclides and high-energetic particles has to be suppressed. Therefore, the laboratory is located 30 m below surface and the counters are lead-shielded. Secondly, the small concentration in water and the half-life of 269 years lead to a small natural activity in water. For surface water the specific activity is ≈ 20 decays/year/liter. Thus, weeks of measurement and several tons of water are necessary which does not allow for e.g. dating of ice cores samples or routine ocean sampling, where the available sample size is limited to liters.
Both limits are (partially) overcome by accelerator mass spectrometry (AMS) [9]. In conventional AMS, the ECR[3] source and the subsequent positive-ion accelerator would lead to a large background of the ^{39}K isobar. Hence, a gas-filled spectrograph and a position sensitive detector serve for separation. With AMS, the water sample size has been reduced to 20 liters and the measurement time to about 5 hours for 14 % accuracy in a surface sample.

[3] Electron Cyclotron Resonance

The basic problem is the limited availability of measurement time on AMS facilities. Besides this, the sample size is still not low enough for clearly resolved measurements of e.g. rarely available antarctic ice cores.

1.1.3. Exemplary applications with ^{39}Ar

Regardless of the difficulties of ^{39}Ar dating between 50 BP to 1000 BP, several successful attempts have been made in the past. The following section presents some exemplary applications that bridge the dating gap and provides further insight into environmental processes that might be investigated.

Groundwater dating

Noble gas temperatures[4] from water samples allow for reconstruction of paleo-temperatures when combined with the corresponding age signal. This has been realized for multiple water reservoirs such as e.g. groundwater [21, 22, 23] or speleothems [24]. Multi-tracer studies are ideally suited for this purpose as they yield the age composition of the water sample.

Ice dating

Ice reservoirs such as polar ice, continental glaciers or cave ice form ideal reservoirs as mixing does not occur. Polar ice cores, however, are not readily available due to the costly extraction [25]. Nevertheless, ^{39}Ar measurements on Greenland ice have been performed [11]. There are also examples where age information was derived from continental glaciers by ^{32}Si [26], but as mentioned afore, contaminations by dust particles may yield misleading results.

Oceanography

^{39}Ar dating also finds application in oceanography. Vertical and horizontal age profiles support general models for the thermohaline circulation which is pictorially described by the "Great Conveyor Belt". Exemplary studies feature both data from LLC [27, 28] and from AMS measurements [9].

[4] Solubilities of noble gases depend differently on temperature. By measuring the concentration ratio between several noble gases in a water sample, the surface temperature can be reconstructed [20, 7].

Applications from other scientific fields

An application of ^{39}Ar detection to medical sciences, not related to any age determination, is presented in [29]. The Hiroshima and Nagasaki atomic bombings led to grave health effects on the population of these cities. The full impact can be understood best by a reconstruction of the fast neutron field. This has been achieved by detection of ^{39}Ar in gravestone samples from the Hiroshima site.
The detection of weakly interacting massive particles is one goal of dark matter research. This could be achieved with a liquid argon detector where scintillations due to ionizing particles can be detected. However, it demands highly pure argon with the lowest ^{39}Ar concentrations possible (ideally $\leq 10^{-18}$). Thus, ^{39}Ar detection of concentrations below this limit would help to identify proper sources for "old" argon [30].

1.1.4. Relative and absolute age precision

The statistical error on the age is the key figure for the time range that can be covered with the current ^{39}Ar count rate. This error Δt is governed by the number of atoms detected, N_{det}, whose expectation value is the product of detection rate $r(t)$ and detection time t_{det}. The detection rate for a sample with age t follows an exponential decay curve with mean lifetime $\tau = T_{1/2}/\ln(2) = 388\text{a}$,

$$r(t) = r_0 \cdot e^{-\frac{t}{\tau}}. \tag{1.2}$$

This can be easily solved for t,

$$t = -\tau \cdot \ln\left(\frac{r(t)}{r_0}\right), \tag{1.3}$$

and the error on the age is likewise obtained:

$$\Delta t = \Delta r(t) \cdot \left|\frac{\mathrm{d}}{\mathrm{d}r(t)} t\right| = \tau \cdot \frac{\Delta r(t)}{r(t)} = \tau \cdot \frac{\Delta N_{det}}{N_{det}}. \tag{1.4}$$

Under the assumption of purely statistical errors due to counting[5], $\Delta N_{det} = \sqrt{N_{det}}$, the absolute error on the age depends only on the mean lifetime τ and the number of detected atoms N_{det},

$$\Delta t = \frac{\tau}{\sqrt{N_{det}}}. \tag{1.5}$$

This expression can be solved for N_{det} as function of age and age error,

$$N_{det} = \left(\frac{\tau}{\Delta t}\right)^2 \overset{t \neq 0}{=} \left(\frac{\tau}{t} \cdot \frac{t}{\Delta t}\right)^2. \tag{1.6}$$

The introduction of t/t in the right part of the previous expression allows to compute $N_{det}(t)$ for constant relative error, $\Delta t/t = \text{const}$. The measurement time to achieve the desired relative precision is derived with the help of eq. 1.2,

$$t_{det} = \frac{N_{det}}{r(t)} = e^{\frac{t}{\tau}} \cdot r_0^{-1} \cdot \left(\frac{\tau}{t} \cdot \frac{t}{\Delta t}\right)^2. \tag{1.7}$$

[5] The smaller the sample size becomes, the more dominant are errors due to the statistical nature of radioactive decay.

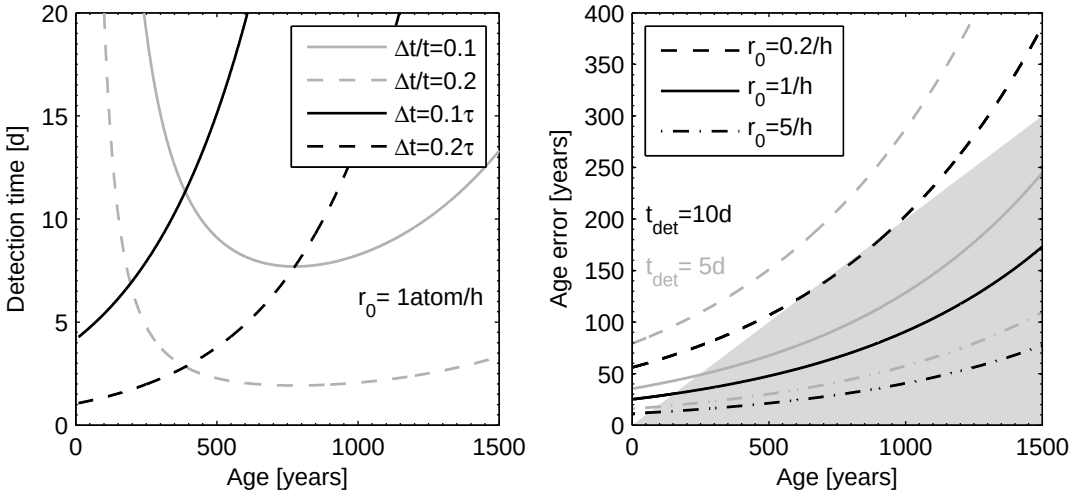

Figure 1.2.: Relation between count rate, detection time, sample age and age error. Left-hand: Required detection time computed for a recent sample count rate of $r_0 = 1$ atom/h and different values of relative and absolute error. Right-hand: Absolute error Δt on the age attainable with different count rates and measurement times. The shaded area indicates precision below 20%.

For constant absolute error, $\Delta t/\tau = \text{const}$, a similar result is obtained:

$$t_{det} = e^{\frac{t}{\tau}} \cdot r_0^{-1} \cdot \left(\frac{\tau}{\Delta t}\right)^2 . \tag{1.8}$$

Fig. 1.2 illustrates the effect of count rate, detection time and sample age on the standard error of the derived age. This allows for an estimate of the necessary count rate in a recent sample. The calculations indicate that 1 atom/hour is already sufficient to achieve 20% relative precision for the greater part of the age range with 10 days of measurement time. Higher precision then either demands higher count rates or -if there is no room for further improvement- longer measurement time.

1.2. Properties of argon

The presence of a non-reactive component in atmospheric air was first observed in 1784 by H. Cavendish. It was isolated and studied about 110 years later by Lord Rayleigh [31]. The name "argon" originates from Greek language where it means "inactive".
Its large abundance in air is due to the production of ^{40}Ar by e$^-$-capture or e$^+$-emission of ^{40}K which is omni-present in earth's crust. ^{39}Ar is mainly produced by spallation-induced reactions in the upper atmosphere, but underground production can also occur [32]:

$$\begin{aligned}
\text{atmospheric production:}\quad & \mathrm{n} + {}^{40}\mathrm{Ar} \rightarrow 2\mathrm{n} + {}^{39}\mathrm{Ar} \\
\text{underground production:}\quad & \mathrm{n} + {}^{38}\mathrm{Ar} \rightarrow \gamma + {}^{39}\mathrm{Ar} \\
& \mathrm{n} + {}^{39}\mathrm{K} \rightarrow \mathrm{p} + {}^{39}\mathrm{Ar} \\
& \mathrm{n} + {}^{42}\mathrm{Ca} \rightarrow \alpha + {}^{39}\mathrm{Ar}
\end{aligned}$$

Today's main technical application for argon is as a shielding gas for welding. Argon is also commonly employed in plasma reactors. In physics, it can be used e.g. for dark matter search (see above), studying gas discharge dynamics, and for atomic beam physics.
Multiple experiments with argon atomic beam apparatuses have been already and are still conducted in the past decades. There are examples from various field of physics such as quantum mechanics [33, 34], lithography [35], matterwave optics [36], antimatter research [37] and many more. Magneto-optical trapping of argon has also been realized in the past and temperatures below 100 µK have been reached [38, 39, 40].

1.2.1. Physical properties

Argon is a noble gas and therefore chemically inert. Due to its closed shell configuration, it does not undergo chemical reactions. After nitrogen and oxygen it is the third most abundant component of earth's atmosphere with a relative concentration of about 1% in air. Most of this argon is the stable isotope ^{40}Ar but there are a number of other stable and radioactive isotopes, see tab. 1.1. The half-life of ^{39}Ar was determined by enriched samples from ^{39}K(n,p)^{39}Ar. A detailed discussion can be found in [41] and results in $T_{1/2} = 269 \pm 3$ a.
The stable isotopes have zero nuclear spin due the even number of neutrons and protons whereas odd isotopes have an odd number of neutrons and therefore possess nuclear spin. Thus, the fine structure levels of the even isotopes split up in the odd isotopes via hyperfine coupling of the total angular momentum and the nuclear spin.

Table 1.1.: Compilation of relevant isotopes of argon, data taken from [42]. Dashes indicate unavailable data.

Isotope	Mass [m_u]	Nat. ab.	Nucl. spin I	μ_I [μ_N]	$T_{1/2}$	Decay
^{35}Ar	34.975257	–	3/2	0.633	1.77 s	EC to ^{35}Cl
^{36}Ar	35.96754552	0.003365(30)	0	0	–	–
^{37}Ar	36.966776	–	3/2	1.15	35.0 d	EC to ^{37}Cl
^{38}Ar	37.9627325	0.000632(5)	0	0	–	–
^{39}Ar	38.962314	$8.5 \cdot 10^{-16}$	7/2	−1.3	268 a	β^- to ^{39}K
^{40}Ar	39.9623837	0.996003(30)	0	0	–	–
^{41}Ar	40.964501	–	7/2	–	1.82 h	β^- to ^{41}K
^{42}Ar	41.9650	–	0	0	33 a	β^- to ^{42}K
^{43}Ar	42.9657	–	–	–	5.4 m	β^- to ^{43}K
^{44}Ar	43.963650	–	0	0	11.87 m	β^- to ^{44}K

1.2.2. Optical transitions

Purely laser based, isotopically selective detection schemes for atoms usually employ cycling transitions. Hence, fig. 1.3 serves to illustrate both the fine structure splitting of the lowest three states of argon and the transitions between these states. In principle, transitions from the ground state to either $1s_2$ or $1s_4$ would be best suited for laser cooling.
These transitions, however, are found in the deep UV spectrum. So far, there exist no

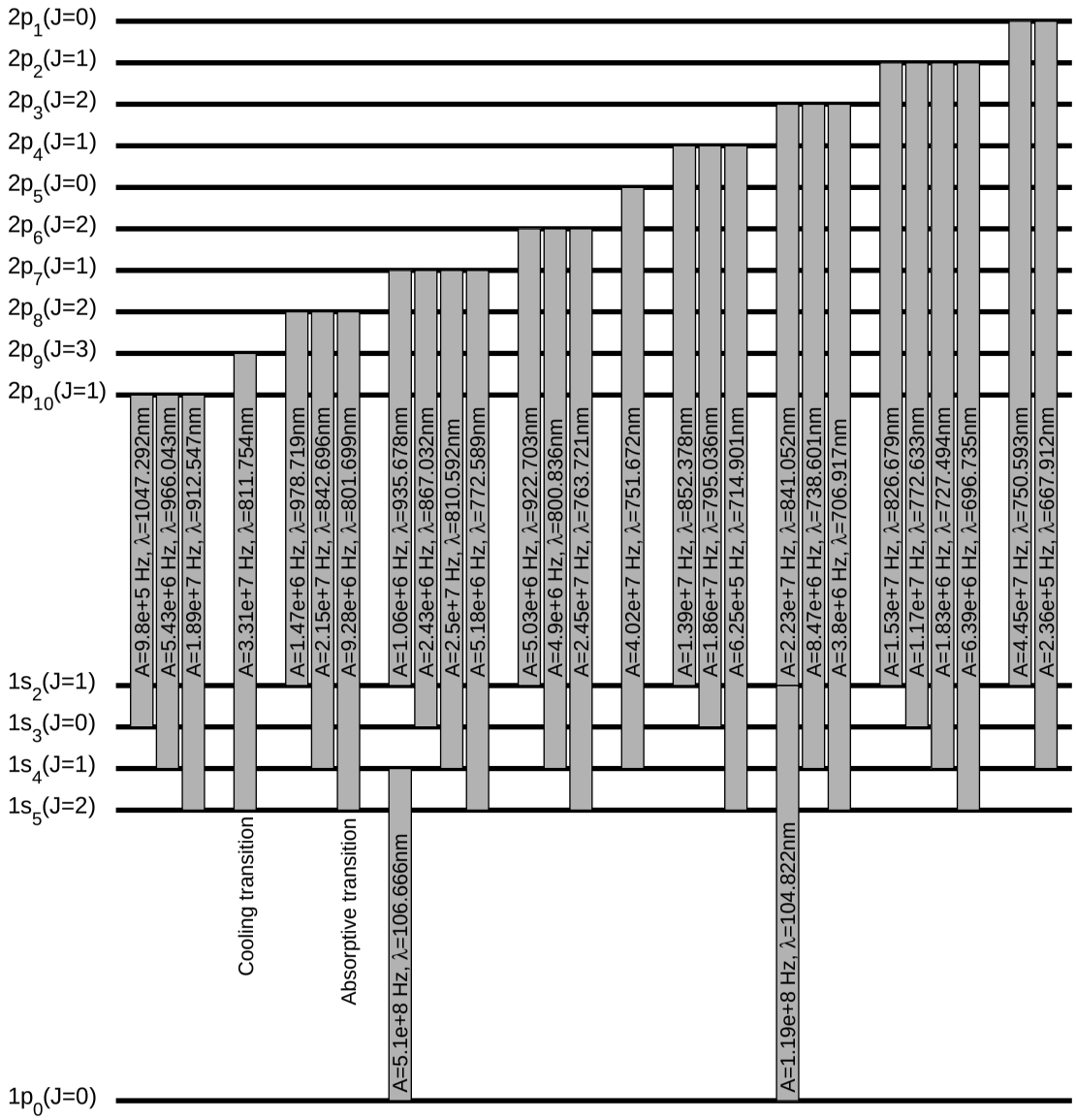

Figure 1.3.: ^{40}Ar transition scheme for the s-/p-multiplets. For cooling of stable isotopes the closed $1s_5$-$2p_9$ transition is most favorable. Transitions like e.g. $1s_5$-$2p_8$ can be used for pumping ^{40}Ar to the ground state, thus suppressing its fluorescence in the detection region.

readily available lasers in this wavelength range (105nm or 107nm). Free-electron lasers could in principle be employed but cannot yet be considered as standard tools. Therefore, atom optical manipulation of argon atoms is until now only possible with metastable atoms.
Metastable atoms are excited atoms that cannot decay to lower-lying states, because the corresponding transitions are dipole-forbidden. In argon, both the $1s_3$ and the $1s_5$ level form such a metastable state. Excitation of atoms to these states can be achieved by either optically pumped transitions or electron impact in discharges, see sec. 4.2. In discharges, the population of $1s_5$ is typically higher than for $1s_3$ (about a factor 6, [43]) while in purely optical schemes it depends on the frequency of the incident light.
For stable isotopes, a cycling transition from the $1s_5$ level is given by $1s_5$-$2p_9$. Atoms are excited from $J = 2$ to $J = 3$ and can only decay back to $J = 2$. With a correspondingly detuned laser, atoms can be slowed down and also trapped by adding magnetic fields.

1.3. Requirements for ^{39}Ar-ATTA

1.3.1. Hyperfine structure

As mentioned above, odd isotopes of argon have nuclear spin which leads to further splitting of the fine structure levels. This hyperfine splitting of the cooling transition remained unknown until recently, when it was first spectroscopically examined by this workgroup, see chapter 2. Knowledge of the shifted energy levels and the additionally necessary frequencies for repumping is crucial for designing an apparatus for cooling and trapping of ^{39}Ar. Fortunately, the shifted transitions were found not to coincide with transitions of the stable isotopes.

1.3.2. Atomic beam apparatus

Efficiency is the key to achieve the highest possible ^{39}Ar count rate. The basic idea is that the efficiency from the atomic beam source to the detector has to be maximized. First, metastable atoms have to be produced at a high rate. This is realized by high sample throughput and large excitation efficiency.
Then, both transversal and longitudinal velocity components have to be reduced. Transversally to minimize beam divergence and longitudinally to maximize trapping efficiency. Given the predicted metastable ^{39}Ar flow, detection has to be possible on the single atom level. Therefore, suppression of background light and high numerical aperture detection optics are implemented.
Furthermore, the size of available natural samples is limited. Hence, sample recycling can reduce the sample consumption. In order to guarantee for sample purity, the recycling scheme features a getter pump that prevents degradation due to outgassing from the vacuum chamber.

1.3.3. Laser system

Having identified the right frequencies for laser cooling by hyperfine structure spectroscopy, different frequencies for different stages of the atomic beam apparatus need to be generated. In each of these stages further sideband frequencies for optical repumping are necessary. Available laser power can be a limiting factor for the performance of atomic physics experiments. This, clearly, must not be the case when highest efficiency is demanded. Therefore, a tapered amplifier laser system was developed. It provides up to 1 W of optical power for each stage of the atomic beam apparatus which is until now absolutely sufficient. Each of the TA's built simultaneously amplifies cooler and repumper sidebands and thus provides perfect overlap of all necessary laser frequencies. Details of the laser system are discussed in chapter 3.

2. Hyperfine structure of $1s_5$-$2p_9$ in ^{39}Ar

Any successful detection of ^{39}Ar atoms by means of laser cooling crucially depends on knowledge of the hyperfine structure (HFS) of the cooling transition $1s_5$-$2p_9$. This has been measured for the first time in the course of the Heidelberg ATTA experiment [44]. However, it has to be admitted that a wrong calibration of the frequency scale resulted in the derived hyperfine constants being systematically too large by a factor of about 1.005. The ATTA group at ANL repeated the measurement and found supposably more correct results [45]. During the discussion related to the disagreement in results, the calibration with the help of a Fabry-Pérot interferometer (FPI) [46] was identified as the cause of the error. A more refined calculation of the FPI free spectral range -taking into account the special setup with a lens in-between the mirrors- strongly improved the agreement between the derived sets of parameters. Therefore, the following section reviews the existing publication [44] and gives corrected values for the parameters in question. It also features some unpublished results from data analysis.

2.1. Theoretical basics

In order to illustrate the means that are used for data analysis an insight into theory of HFS is provided in the following[1]. The isotopic shift between the different argon isotopes is also briefly discussed as it leads to shifts between the centers-of-mass of the HFS pattern for different isotopes.
The emergence of hyperfine structure is a direct effect of the interaction between magnetic dipole moment (and electric quadrupole moment) of an atom and its electrons. It is only present in atoms with a non-vanishing nuclear magnetic moment. Stable argon isotopes have even numbers of both neutrons and protons and consequently cannot show hyperfine splitting. The splitting leads to further substructure of the fine structure levels which is by about four orders of magnitude smaller than the fine structure splitting itself.
According to [47] the nuclear magnetic dipole moment $\vec{\mu}_I$ interacts with the magnetic field of the electrons, the resulting interaction energy is approximately[2]

$$V_{magn} = -\mu_I \cdot H(0) \cdot cos\left(\vec{\mu}_I, \mathbf{H(0)}\right) \tag{2.1}$$

where $\mathbf{H(0)}$ denotes the magnetic field of the electrons at the position of the nucleus. For ^{39}Ar, the nuclear magnetic moment is $\mu_I = -1.3$ and the nuclear spin is $I = +7/2$, [42].

[1] In the available literature better-suited approaches to a full understanding of this topic can be found. One of the most valuable resources in this context is [47] where an insight into both theoretical and experimental methods is provided. The interested reader is therefore kindly asked to refer to this volume which is also available in English.

[2] The nuclear magnetic dipole moment is approximated as that of a point-like dipole.

According to perturbation theory the energy shift ΔE_{magn} is obtained by the average of $H(0)$ over time, $\overline{H(0)}$. This leads to

$$\Delta E_{magn} = A \cdot \frac{C}{2} \tag{2.2}$$

$$\text{with the magnetic hyperfine constant } \; A = \frac{\mu_I \overline{H(0)}}{IJ}$$

$$\text{and the Casimir constant } \; C = F(F+1) - I(I+1) - J(J+1)$$

where J denotes the total electron angular momentum quantum number, I the nuclear spin and F the total atomic angular momentum quantum number.
The hyperfine constant B arises when corrections due to the electro-static interaction between nucleus and electrons are considered and the finite size of the nucleus comes into play. From this, the energy shift ΔE_{el} is computed to be

$$\Delta E_{el} = \frac{B}{4} \cdot \frac{\frac{3}{2}C(C+1) - 2I(I+1)J(J+1)}{I(2I-1)J(2J-1)} \tag{2.3}$$

$$\text{with the quadrupole coupling constant } \; B = e \cdot Q \cdot \overline{\varphi_{JJ}(0)}$$

$e \cdot Q$ is the quadrupole moment of the nucleus and $\varphi_{JJ}(0)$ is the vector gradient of the electric field of the electron shell at the position of the nucleus. The subscript $_{JJ}$ denotes the rotational symmetry of the electric field around the J-axis.
The combination of both magnetic interaction and electric interaction leads to the HFS formula

$$\Delta E = \frac{A}{2}C + \frac{B}{4}\frac{\frac{3}{2}C(C+1) - 2I(I+1)J(J+1)}{I(2I-1)J(2J-1)}. \tag{2.4}$$

In the case of the $1s_5$-$2p_9$ transition in ^{39}Ar with $I(^{39}Ar) = +7/2$, $J(1s_5) = 2$ and $J(2p_9) = 3$, the metastable state splits up into five levels from $F_s = 3/2$ to $11/2$ and the excited state splits up into seven levels from $F_p = 1/2$ to $13/2$. Each of the F states is degenerated and splits up in a magnetic field into $2F + 1$ m_F states.
The isotopic shift between argon isotopes is mainly mass-related. For heavier nuclei also volume effects start to become more important. This mass-induced shift can be understood in terms of Bohr's model such that the mass of the electron has to be substituted by the reduced mass. A spectral line -as difference between two levels- is therefore shifted by

$$\Delta\nu = \frac{m_e}{m_p} \cdot \frac{M_2 - M_1}{M_2 \cdot M_1} \tag{2.5}$$

between isotope 2 and isotope 1. For the $1s_5$-$2p_9$ transition and the difference between ^{36}Ar and ^{40}Ar the formula yields the "normal mass shift" (NMS) $\Delta\nu \approx -563.08$ MHz. The difference to the observed shift ([48], -450.1 MHz) can be explained by two contributions. One is the correlation between the movements of the different electrons, the "specific mass-shift". The other one actually accounts for volume effects, thus changes in the nuclear charge distribution. Both additional contributions depend on the electronic wave functions of the ground and excited state.
The calculated NMS between ^{39}Ar and ^{40}Ar is -130.1 MHz. Simply using the same factor as above (450.1/563.08) leads to $\Delta\nu \approx -104$ MHz, which may serve as a first estimate.

Table 2.1.: Isotopic shifts for different argon isotopes and two transitions. Eq. (2.6) yields the shift of ^{39}Ar relative to ^{40}Ar and holds as the value for calculation from ^{36}Ar and ^{38}Ar is the same within the errors. The measured value agrees with the calculated value within the errors.

Isotope	Transition	$\Delta\nu$ [MHz]	ref.
36-40	$1s_5 - 2p_6$	$-494.9 \pm .6$	[49]
38-40	$1s_5 - 2p_6$	$-229.5 \pm .4$	
39-40	$1s_5 - 2p_6$	-107.1 ± 7.0	
36-40	$1s_5 - 2p_9$	$-450.1 \pm .9$	[48]
38-40	$1s_5 - 2p_9$	-208.1 ± 1.5	
39-40	$1s_5 - 2p_9$	-97.4 ± 6.4	Eq.(2.6) for ^{36}Ar
39-40	$1s_5 - 2p_9$	-97.1 ± 6.4	Eq.(2.6) for ^{38}Ar
39-40	$1s_5 - 2p_9$	$-94.6 \pm .4$	This experiment

2.2. Estimation of parameters

A first crude approximation of the expected spectrum can be obtained from available literature values for the coefficients A and B of different noble gas isotopes. For the $1s_5$ level in ^{39}Ar the coefficients have already been measured [49]. However, they come with relatively large uncertainties. For the $2p_9$ level no such data is available. Therefore it has been tried to compute A_p and B_p from correlations between the few data for ^{39}Ar levels ([50, 49]) and data for ^{37}Ar ([51]) and ^{21}Ne [52, 53, 54, 55, 56, 57], respectively[3]. The estimates can be seen in fig. 2.1 and are also listed in tab. 2.2 together with experimental results.
The isotopic shift was estimated from the ratio of the shifts of other isotopes between the $1s_5 - 2p_9$ ([49]) and the $1s_5$-$2p_6$ transition ([48]) with help of the following empirical relation:

$$\Delta\nu_{40}^{39}(1s_5 - 2p_9) = \frac{\Delta\nu_{40}^{iso}(1s_5 - 2p_9)}{\Delta\nu_{40}^{iso}(1s_5 - 2p_6)}\Delta\nu_{40}^{39}(1s_5 - 2p_6) \tag{2.6}$$

where $\Delta\nu_{40}^{iso}(1s_5 - 2p_{6/9})$ denotes the isotopic shift of the transition $1s_5 - 2p_{6/9}$ in the isotope ^{iso}Ar relative to the frequency of the same transition in ^{40}Ar. The corresponding data is given in Table 2.1.
The estimated values can be used to calculate the expected spectrum. This needs to be done as especially the tuning range of the spectroscopy laser has to match the width of the spectrum. The calculation yields a minimum tuning range of $f_{Ar-40} \pm 2$GHz.

[3] In this context the question may arise why the B coefficients of two isotopes of different elements should at all be correlated. But it has to be kept in mind that neon and argon are both noble gases, thus they are similar in electronic structure. The fact that they are neighbors in the periodic table is also helpful as it means that they are especially similar.

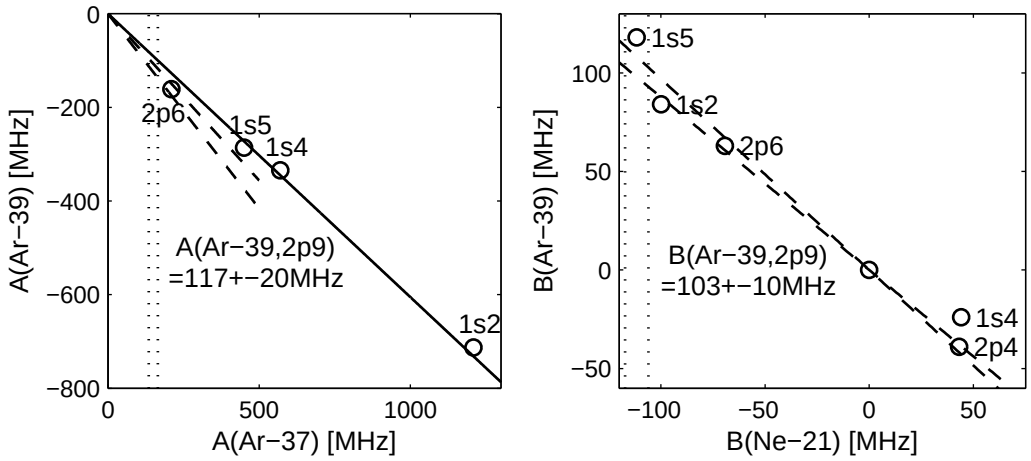

Figure 2.1.: Prior to the measurement the hyperfine coefficients A and B of the $2p_9$ level are estimated from correlations between the coefficients of different states in ^{39}Ar and ^{37}Ar and ^{21}Ne, respectively. The A_s coefficients for the lower level of different argon isotopes seem well correlated thus this is assumed to be true for A_p. Similarly, B_p is obtained. Dotted lines indicate intervals for the parameters of the correlated isotope.

2.3. Experimental determination

2.3.1. Sample preparation

The gas sample is extracted from 410 mg potassium-rich mineral (HD-B1 biotite with ≈8% K, [58]) which has been irradiated in a neutron reactor. Neutron exposure at the GKSS Research Centre Geesthacht (fast neutron flux: 10^{12} $s^{-1}cm^{-2}$) for 20 days leads to the production of ^{39}Ar by ^{39}K(n,p)^{39}Ar. The neutron irradiation also induces production of short lived radioisotopes. Therefore, an additional period of ≈25 days is necessary after which these have decayed sufficiently. The irradiated sample is vacuum-melted, the gas purified and subsequently transferred via a zeolite-filled cold finger at lN_2 temperature to the specially designed spectroscopy cell. For further details of sample preparation, neutron irradiation, argon extraction and cleaning see [59]. The mineral also contains ^{40}Ar from in situ ^{40}K decay ($T_{1/2} \approx 1.3$ Ga) leading to $^{39}Ar/^{40}Ar \approx 0.8$ as determined via mass spectrometry from a simultaneously irradiated HD-B1 sample.
A quartz glass cell attached to a metal glass adapter is used for spectroscopy. The cell is cleaned by employing a similar scheme as reported in [60]. First the cell is rinsed with sodium hydroxide solution and deionized water. Then, it is subjected to an ultrasonic bath of deionized water at 35°C for 5-10 minutes. Finally it is flushed with methanol and deionized water. This procedure is repeated several times.
Subsequently the cell is attached to the vacuum system and baked out during evacuation (120°C for 12 hours). In the next step an argon gas discharge is used to clean the cell more thoroughly before filling it with the actual sample. This is done with commercially available argon of atmospheric isotopic composition. The RF discharge used to populate the metastable levels operates at a pressure of 10^{-2} mbar and causes implantation of argon atoms into the cell walls [61]. Consequently this argon is desorbed from the cell walls when the discharge is operated at substantially lower pressures ($\approx 10^{-4}$ mbar).

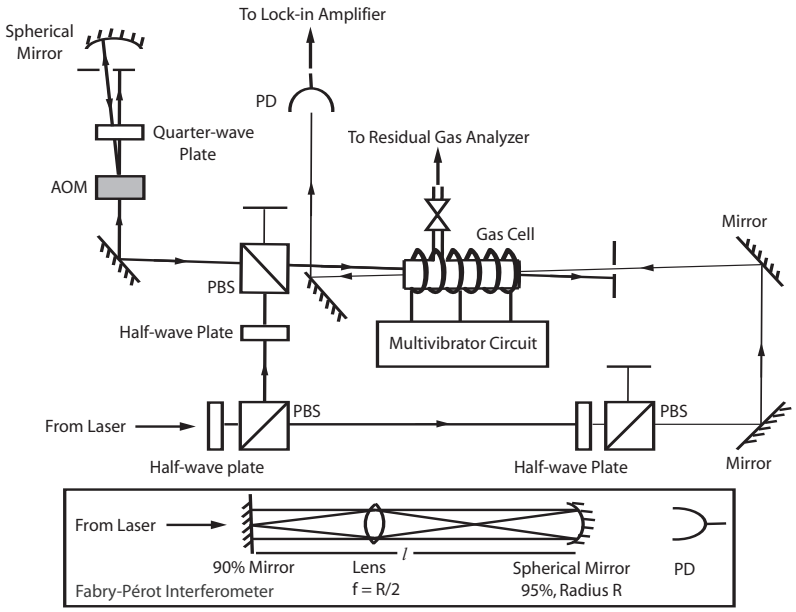

Figure 2.2.: The experiment is set up as Doppler-free saturation spectroscopy. The pump beam ($I = 3 \cdot I_{sat}$) enters the cell from the left side after being frequency-modulated at 22 kHz with an amplitude of 10 MHz. The probe beam ($I = 0.7 \cdot I_{sat}$) counter-propagates and is detected on a fast photodiode. The Fabry-Pérot interferometer (FPI) has half the free spectral range of a confocal FPI due to the lens/mirror combination.

The degassing problem is overcome by running a high power gas discharge (up to 80 Watts) for about half an hour followed by controlled evacuation with a turbo molecular pump down to pressures of 10^{-6} mbar or less. Laser spectroscopy of the $1s_5 - 2p_9$ transition in ^{40}Ar is used to deduce the pressure during outgassing. This procedure is repeated until the pressure increase by degassing is negligible. During the evacuations the gas from the cell is analyzed with a commercially available residual gas analyzer which allows for obtaining quantitative information on its composition.

2.3.2. Optical setup

A setup for modulation transfer Doppler-free saturation spectroscopy [62] in an argon gas discharge cell as depicted in fig. 2.2 is employed. The RF plasma discharge is powered by a multivibrator circuit with vacuum tubes that operates at high peak voltages (up to 600V, [63]). This high voltage allows for plasma ignition even at low densities since the acceleration forces on the charged particles are sufficiently strong.
The pump beam is frequency modulated by a double pass AOM. The photodiode signal of the transmitted spectroscopy beam is demodulated using a lock-in amplifier. This leads to a signal (derivative of the absorption profile) at frequencies where both beams are resonant with the same velocity class of atoms. By modulating only the pump beam the derivative of the broad Doppler valley is suppressed. A setup where both beams are simultaneously modulated would lead to an undesired spectrally varying offset on the spectroscopy signal. Since the laser linewidth is ≈ 0.6 MHz and the gas pressure is low ($< 10^{-3}$ mbar) the predominant line broadening mechanisms are power broadening and modulation broadening.

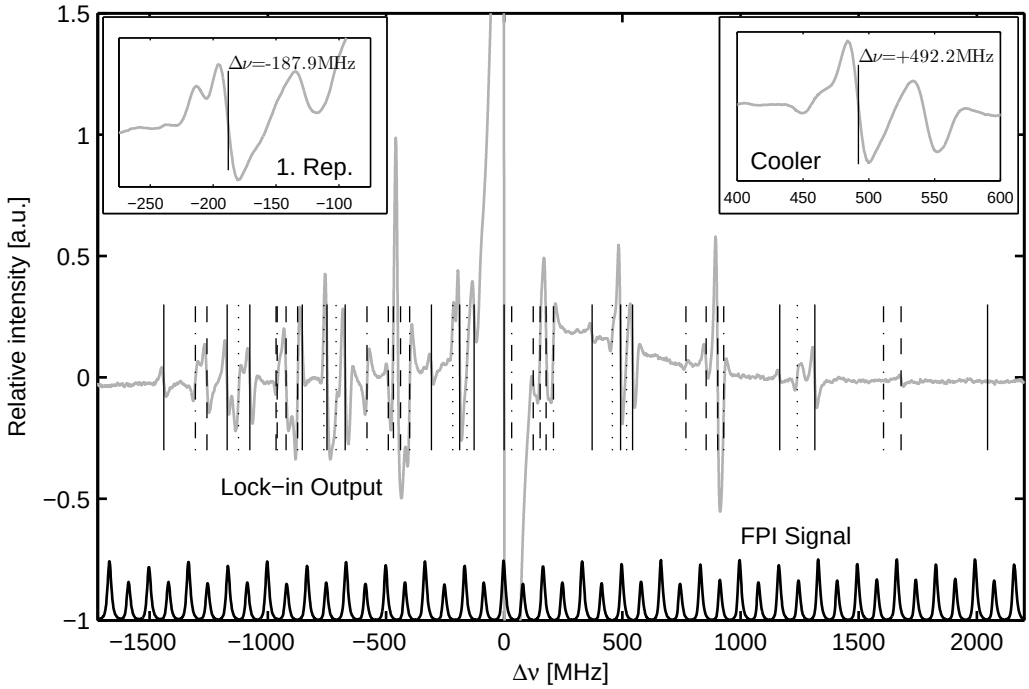

Figure 2.3.: The spectroscopy signal averaged over 3200 single scans. Vertical lines indicate the deduced resonances. Solid lines: transitions between 2 hfs states; dashed: crossovers with adjacent excited levels; dash-dotted, dotted: other crossovers as indicated in fig. 2.5.

These effects result in a measured linewidth of 30 MHz whereas the natural linewidth of the transition is 5.85 MHz [64].
The signal-to-noise ratio of the data is improved by averaging over many laser frequency scans. The spectroscopy signal in fig. 2.3 thus corresponds to about 3200 single scans with 250 ms for each scan. The transmission signal of a FPI is simultaneously recorded. As the scan of the laser frequency deviates slightly from being linear, the FPI peaks are needed to precisely determine a frequency scale. The ^{40}Ar peak is used as reference for averaging the single scans and thus allows for compensation of laser drifts.
The FPI has free spectral range of $c/(8 \cdot l_{eff}) = 82.96$ MHz due to the special design (lower part in fig. 2.2). As explained in the introduction of this chapter, this differs from the previously used $c/(8 \cdot l) = 83.33$ MHz. The lens in between the mirrors can be described as effectively increasing the optical path length. This applies as it has a index of refraction greater than 1.

2.4. Data analysis

The frequency calibrated spectroscopy signal is then analyzed for resonances. According to selection rules each HFS ground state with F_g can be excited to $F_g - 1..F_g + 1$ which results in a set of 15 possible atomic transitions. Nevertheless, a total of 40 resonances are identified, some of which must hence arise from spectroscopy. Due to the Doppler-free setup the atomic resonances lead to enhanced transmission. Thus the derivative of a

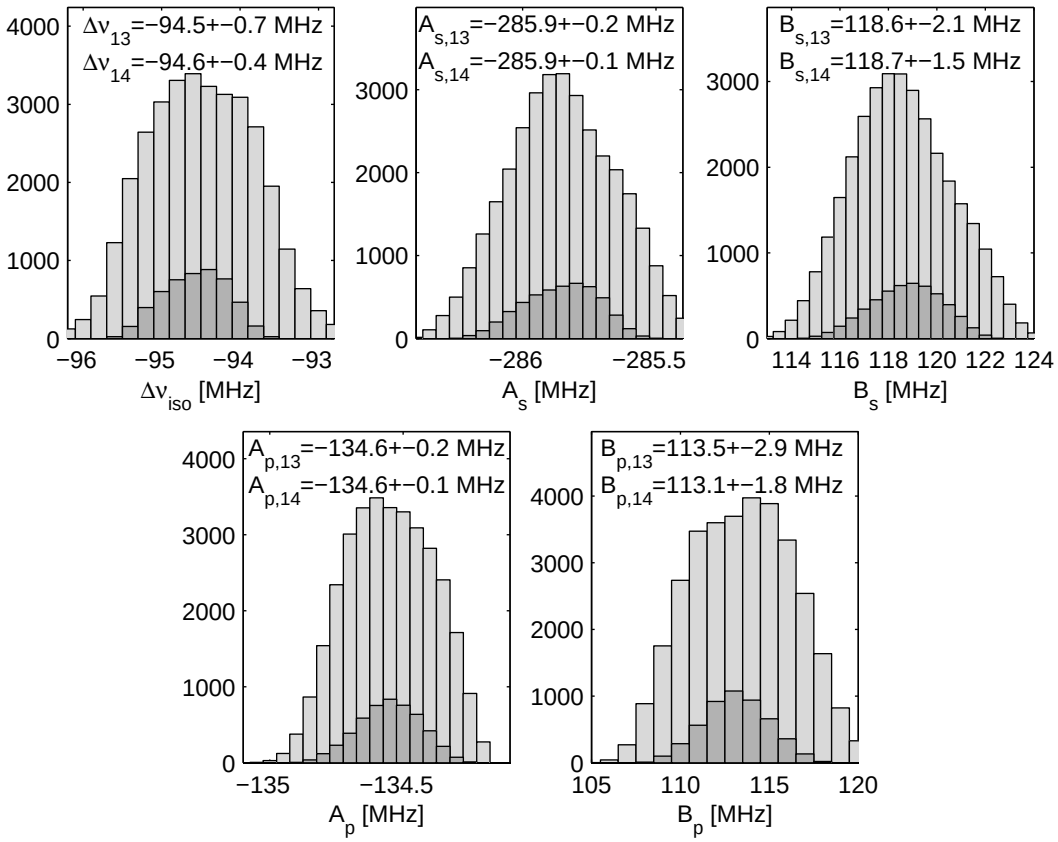

Figure 2.4.: Hyperfine constants and isotope shift as derived from the analysis of the observed spectrum. The histograms depict the number of parameter sets with either 13 (light gray) or 14 (dark gray) matching lines for each tested value of one parameter. Some histograms are lopsided which is probably due to discretization of parameters during fitting. But mean and median are always about the same so this is considered irrelevant.

scan over these peaks is first positive then negative. Therefore the number of transitions going into the calculation is reduced by omitting those resonances with the wrong sign of derivative. Of the 40 originally observed resonances still 23 remain.
In Doppler-free spectroscopy with nearby atomic resonances, crossovers resonances are likely to be observed[4]. There are 15 possible crossover resonances between lines with the same hfs-ground-state. These 15 are not easily distinguishable from the original 15 atomic resonances as they have the same sign of slope. So the set of lines obtained from the spectrum is checked according to whether lines are right in-between two other lines. This further reduces the set of resonances to 15 lines. As it turns out during evaluation, one atomic resonance is not observed, therefore one crossover resonance remains in the set of lines.
The hfs constants A_s, B_s, A_p, B_p and the isotopic shift $\Delta\nu$ are fitted to the data. This is done by variation of these five parameters over a large range and counting the number of resonances that can be reproduced by calculation within the errors. It is found that up to 14 resonances can be both observed and calculated.
Fig. 2.4 summarizes the results for all parameters. In this specific run of the fitting program 5059 (32991) sets of parameters with 14 (13) matching resonances were found. The results are plotted in histogram form and the value of each parameter is calculated by the mean and the standard deviation of the histogram. The agreement between the value derived from 14 and 13 matching resonances is well within the standard deviations. The error, however, is larger for 13 matches as one line less has to match.
Analysis of the remaining observed features indicate that these are spectroscopic crossovers of different types. Fig. 2.5 illustrates the derived crossover scheme. All lines that are calculated with the help of this scheme are plotted into fig. 2.3 and agree well with the experimental results.
Having found the hyperfine constants of both lower and upper state, the energy splitting is calculated and depicted in fig. 2.6. Losses during laser cooling are dominated by undesired excitation to adjacent excited states. Therefore $F = 11/2 \rightarrow F = 13/2$ is the favored cooling transition as it minimizes these losses due to the larger distance to other excited levels.
Tab. 2.2 compares the experimentally derived parameters with the existing literature values. Generally, they are found to agree quite well within the errors. Note that there is a systematic error of about 10^{-3} which is due to the error in length measurement of the FPI. The parameters estimated from the correlations between different noble gas isotopes are also close to the actual results which supports the method of estimation.

[4] At resonance frequency, atoms of one certain velocity class ($v \neq 0$) are excited via transition A by the first laser beam. This fulfills the resonance condition, $\omega_A - k_A v = \omega_{res}$. The counter propagating beam excites the same atoms via a different transition and $\omega_B + k_A v = \omega_{res}$ holds. Solving for the Doppler shift $\Delta_L = kv = (\omega_A - \omega_B)/2$ and plugging in one of the resonance conditions yields $w_{res} = (\omega_A + \omega_B)/2$.

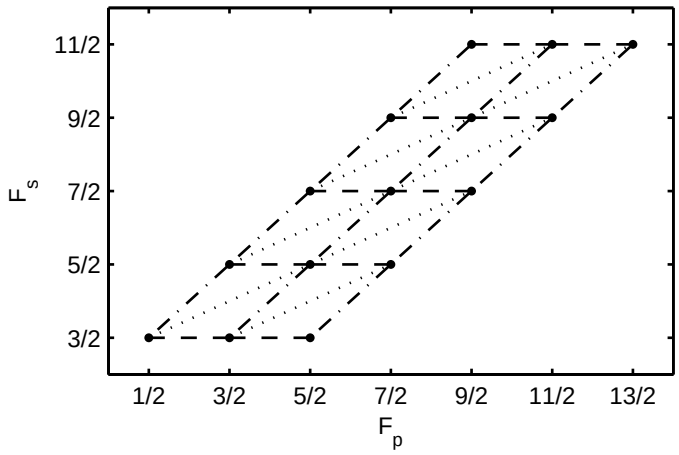

Figure 2.5.: This scheme describes the different types of calculated transitions. Dots indicate transitions between two hfs levels, the lines of different style indicate different types of crossover resonances between two transitions as used in fig. 2.3.

Table 2.2.: Data for the hyperfine constants of the $1s_5$ and $2p_9$ levels of ^{39}Ar as estimated and measured experimentally. The larger errors on the B's result from eq. (2.4) being much less sensitive to B than to A. Statistical errors are given, due to the frequency calibration with a FPI the additional relative systematic error of $1.1 \cdot 10^{-3}$ has to be minded.

	Estimation	This work	ANL [45]
A_s [MHz]	-286.1 ± 1.4[a]	$-285.9 \pm .14$	$-285.36 \pm .13$
B_s [MHz]	118 ± 20[a]	118.7 ± 1.5	117.8 ± 1.2
A_p [MHz]	-117 ± 20[b]	$-134.6 \pm .12$	-134.36 ± 0.08
B_p [MHz]	103 ± 10[c]	113.1 ± 1.8	113.1 ± 1.4

[a] see [49]: analysis using data from ^{37}Ar
[b] estimated from the hfs constants of ^{37}Ar
[c] estimated from the hfs constants of ^{21}Ne

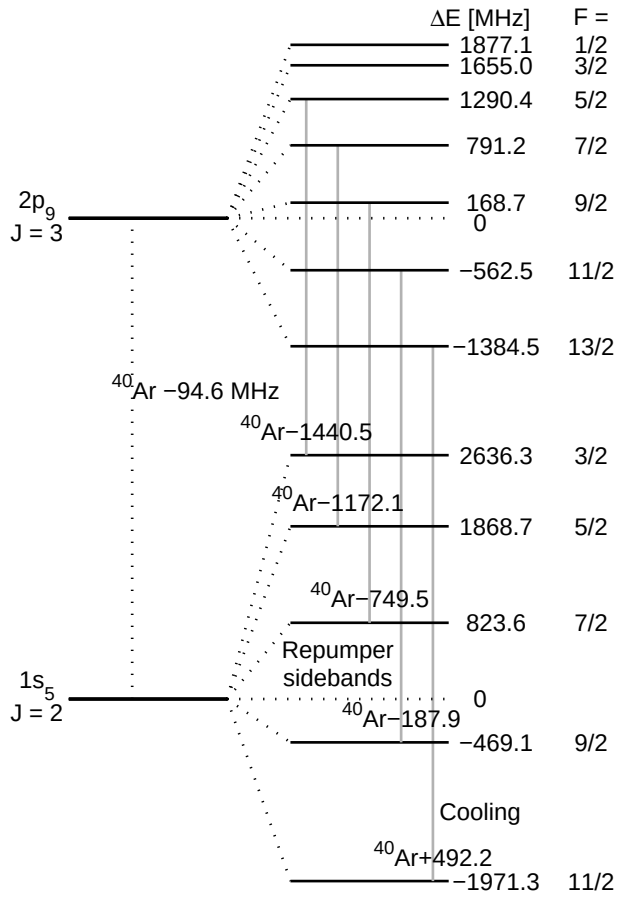

Figure 2.6.: Energy diagram of the levels relevant for cooling and trapping of ^{39}Ar. The vertical lines indicate the designated cooling transition as well as the necessary repumper sidebands.

3. Laser system

The laser system employs diode lasers and acousto-optic modulators and it is set up to meet three basic requirements. Firstly, frequency stability is essential as the light force on the atoms depends on the scattering rate which is governed by the small transition linewidth. Secondly, several laser frequencies are needed to compensate for the varying Doppler and Zeeman shifts in the different stages of the apparatus. Due to the hyperfine splitting in ^{39}Ar, additional "repumper" sidebands also have to be generated. Thirdly, for a successful ATTA setup efficiency considerations come into play, so that sufficient laser power has to be provided. This allows for large laser beams with high intensity i.e. large capture regions both in real and in momentum space.
The contents of this chapter can be seen as overview of and supplement to the diploma theses [65] and [66]. Therefore, it is kept compact and focuses on providing essential information.

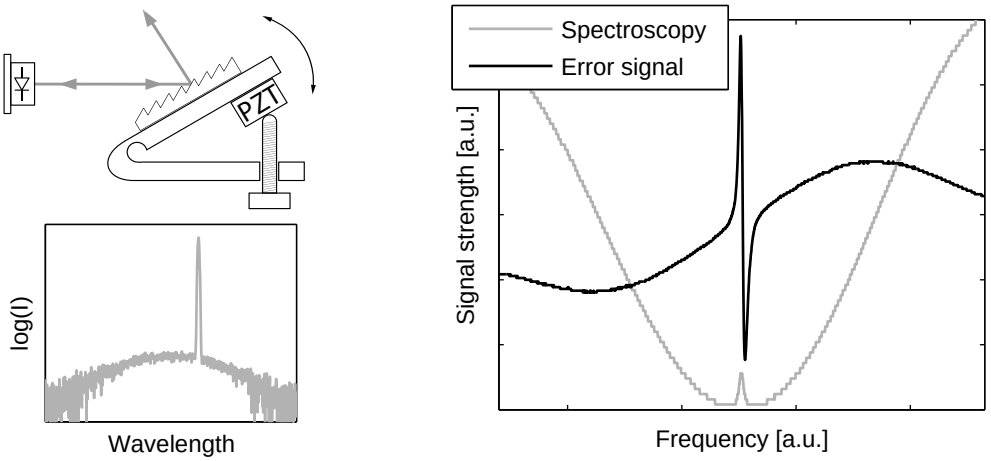

Figure 3.1.: Top left: ECDL in Littrow design. A narrow frequency range is reflected back to the laser diode via first-order diffraction from the grating. Induced emission on this frequency range leads to frequency narrowing. Bottom left: corresponding spectrum, schematic. Right: spectroscopy signal and error signal from Doppler free saturation spectroscopy

3.1. Frequency stabilization

In order to have an absolute locking point, a self-built external cavity diode laser (ECDL) is stabilized to the $1s_5$-$2p_9$ transition in ^{40}Ar. The ECDL works in Littrow configuration (fig. 3.1) such that part of the light emitted from the diode is retro-reflected by a grating. This serves for frequency selection as it leads to induced emission on a narrow frequency

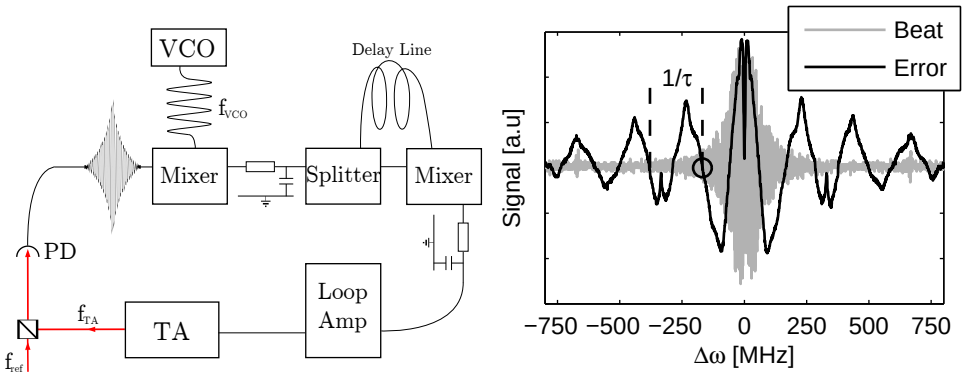

Figure 3.2.: Left: schematic of the beat lock loop for generation of an error signal from the beat note. Right: Typical beat note signal and error signal. The circle indicates the locking point for ^{39}Ar,−168 MHz. Dashed lines indicate the spacing given by the delay line. The beat signal shown is strongly damped towards higher frequencies as the oscilloscope recording the data has a rather small bandwidth.

range. In the latter this laser is referred to as “Master”.
Stabilization is realized via Doppler-free saturation spectroscopy in a RF discharge cell (argon pressure ≈ 0.05 mbar). The laser current is sinusoidally modulated with 20 kHz which leads to modulation of the spectroscopy signal. A lockin-amplifier produces the derivative of this signal which is fed into the PI-loop controlling the grating via a piezo.
The linewidth of the emitted laser light is obtained by observation of the beating signal between two ECDLs and is found to be ≈ 600 kHz. This is sufficiently smaller than the transition linewidth.
Two commercial diode laser systems are stabilized relative to the “Master” via beat signals on fast photo diodes. As one of them mainly serves for generation of the cooling light and the other for repumping light, they are denoted “Cooler” and “Repumper”, respectively[1]. The electronics for generation of an error signal are schematically illustrated in fig. 3.2 and are realized with standard RF electronics. Further details on this locking scheme can be found in e.g. [65].

3.2. Sideband generation

The ^{39}Ar hyperfine splitting derived from the measurement in sec. 2.4 indicates that there is a non-vanishing probability to excite an atom via e.g. $F_g = 11/2 \rightarrow F_e = 11/2$ while the irradiating light is resonant with $F_g = 11/2 \rightarrow F_e = 13/2$[2]. The atom can then decay via $F_e = 11/2 \rightarrow F_g = 9/2$ and is hardly cooled down any more. This effect becomes

[1] The PI-stabilized laser is first shifted by 240 MHz. This then allows for simple switching the Cooler between ^{39}Ar (−168.0 MHz) and ^{40}Ar (−660.2 MHz) for possible monitor purposes. Otherwise, it had to be switched from +72.0 MHz to −420.2 MHz which is not easily achieved by changing just the VCO frequency.

[2] Strictly speaking, under perfect conditions this would not apply to the Zeeman slower. The magnetic field is always directed along the atomic beam and circularly polarized light is used. Therefore, only transitions with $\Delta m_F = -1$ are allowed. However, the polarization is never perfect, especially not after a fiber and a dielectric mirror.

especially important in the case of high intensities, where the spectral lines are further intensity broadened. In the MOT, it is the dominant loss channel due to the large number of scattering events.
Figs. 3.3 and 3.4 illustrate these "hyperfine losses". Details on the calculations are not included here, but basically line broadening is calculated for the different intensities[3]. Then, for each of the possible transitions, the transition rate is calculated and normalized to an excitation probability matrix for one scattering event, E. The size of E is $n_e \times n_g$ corresponding to the number of ground and excited states. The decay probabilities from the excited levels can be derived from Clebsch-Gordan-coefficients and produce a $n_g \times n_e$ matrix, D. The product of both matrices is a $n_g \times n_g$ transfer matrix $T = D \circ E$. For a given initial distribution over the possible ground states p_i the final distribution p_f after N scattering events is

$$p_f = T^N \cdot p_i \tag{3.1}$$

Starting with all atoms in $F_g = 11/2$, $p_i = (1; 0; 0; 0; 0)$, the probability to find an atom in the final $F_g = 11/2$ state is then simply the first component of p_f, $p_f(1)$.
Additional optical pumping is usually employed to close these hyperfine loss channels. Most of the atoms can be pumped back to $F_g = 11/2$ after a couple of cycles on the $F_g = 9/2 \rightarrow F_e = 11/2$ transition. Nevertheless, some atoms might also be pumped to $F_g = 7/2$ via $F_g = 9/2 \rightarrow F_e = 9/2$. This motivates one further repumper sideband resonant with $F_g = 7/2 \rightarrow F_e = 9/2$.
The Cooler and Repumper are locked to frequencies from where all necessary sidebands can be produced with acousto optical modulators (AOMs). Most of the AOMs operate in double pass configuration, see fig. 3.5. The main advantage is that the AOM frequency can be changed without beam displacement. Another advantage is that the absolute frequency tuning range is doubled. In turn, the disadvantage is that the double pass setup is less efficient in terms of laser power: The diffraction efficiency is about $70 - 80$ % per pass, hence $50 - 60$ % in double pass configuration.
For each experimental stage, the laser beams of different frequency are overlapped with equal polarization in a single mode optical fiber. The polarization has to be aligned to one of the axes of the fiber to maintain polarization. The light is then guided to a tapered amplifier laser. Maximum amplification is achieved when the polarization of the incoming light matches that of the amplifier.

3.3. Amplification

In the course of a diploma thesis [65] a fiber-coupled tapered amplifier (TA) system was designed and built. Details such as mechanical, optical, and electrical setup, and specification of the components can be found there. Transversal mode beam analysis shows that the diodes used lase on the TEM_{01}. This leads to a reduced fiber coupling efficiency of only about 40 %[4].
However, as each of the TAs produces up to 1 W (850 mW after the optical isolator)

[3] For the formula for scattering rate, line broadening and saturation parameter please see sec. 4.3.
[4] This is not only governed by the transversal mode but also partly due to the optical fiber. Uncoated fiber ends reflect about 4 % each which -combined with the coated fiber coupler lenses- already limits transmission to ≈ 90 %.

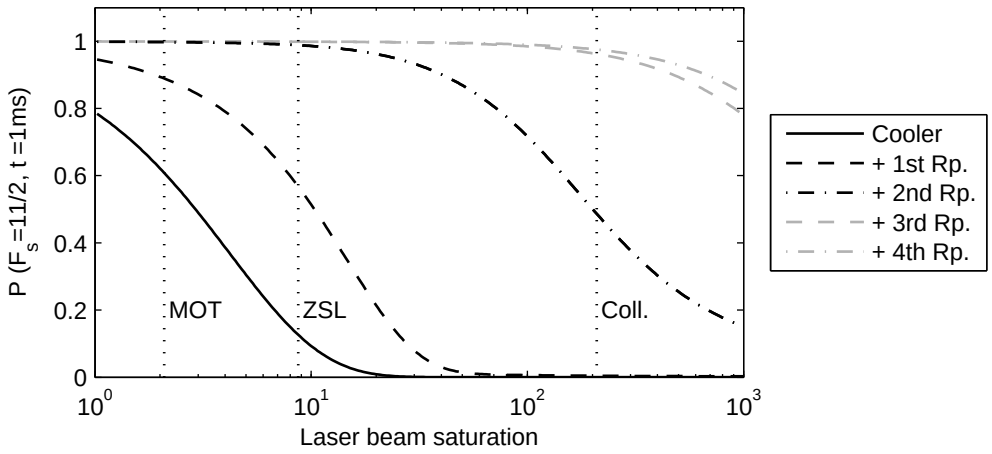

Figure 3.3.: Probability to find atoms in $F_g = 11/2$ after 1 ms. This timescale is chosen as it is on the one hand typical for both collimator ($\bar{\tau} \approx 0.3$ ms) and Zeeman slower ($\bar{\tau} \approx 5$ ms) and on the other hand well illustrates the effect on atoms in the MOT. Strongest losses occur in the collimator due to the very high saturation and therefore severe line broadening.

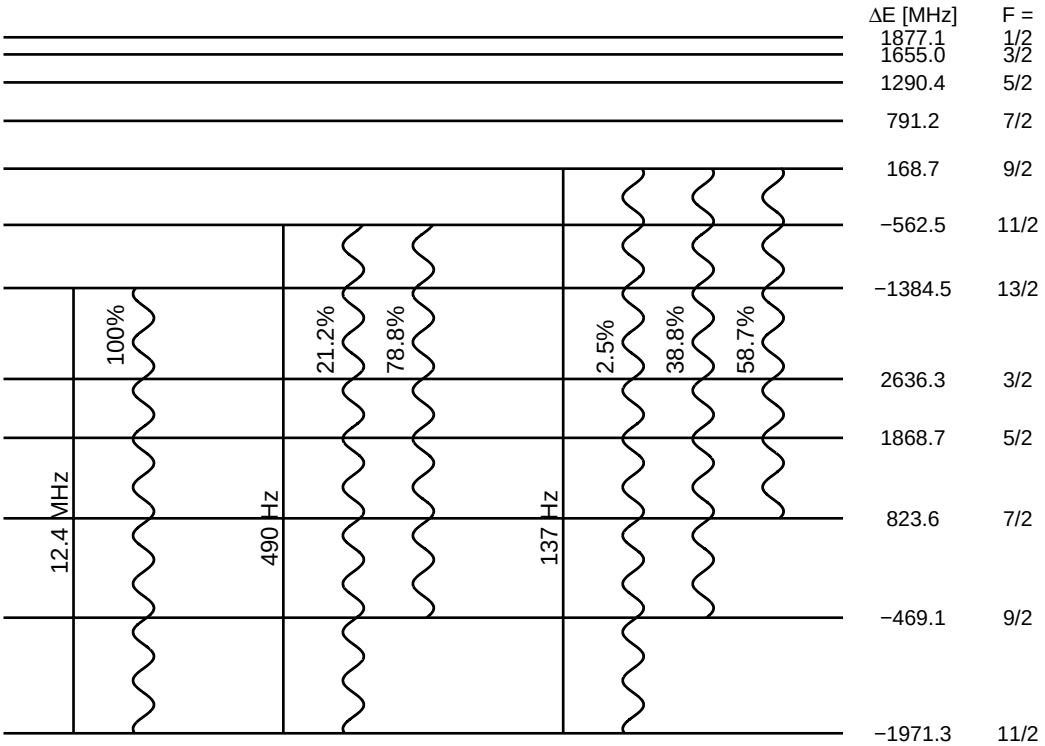

Figure 3.4.: Fractional transition probabilities while driving the $F_g = 11/2 \rightarrow F_e = 13/2$ transition. The calculation of the excitation rates (straight vertical lines) was done for a saturation parameter $s \approx 2$ which is typical for the MOT. The decay probabilities (curved lines) correspond to Clebsch-Gordan-coefficients.

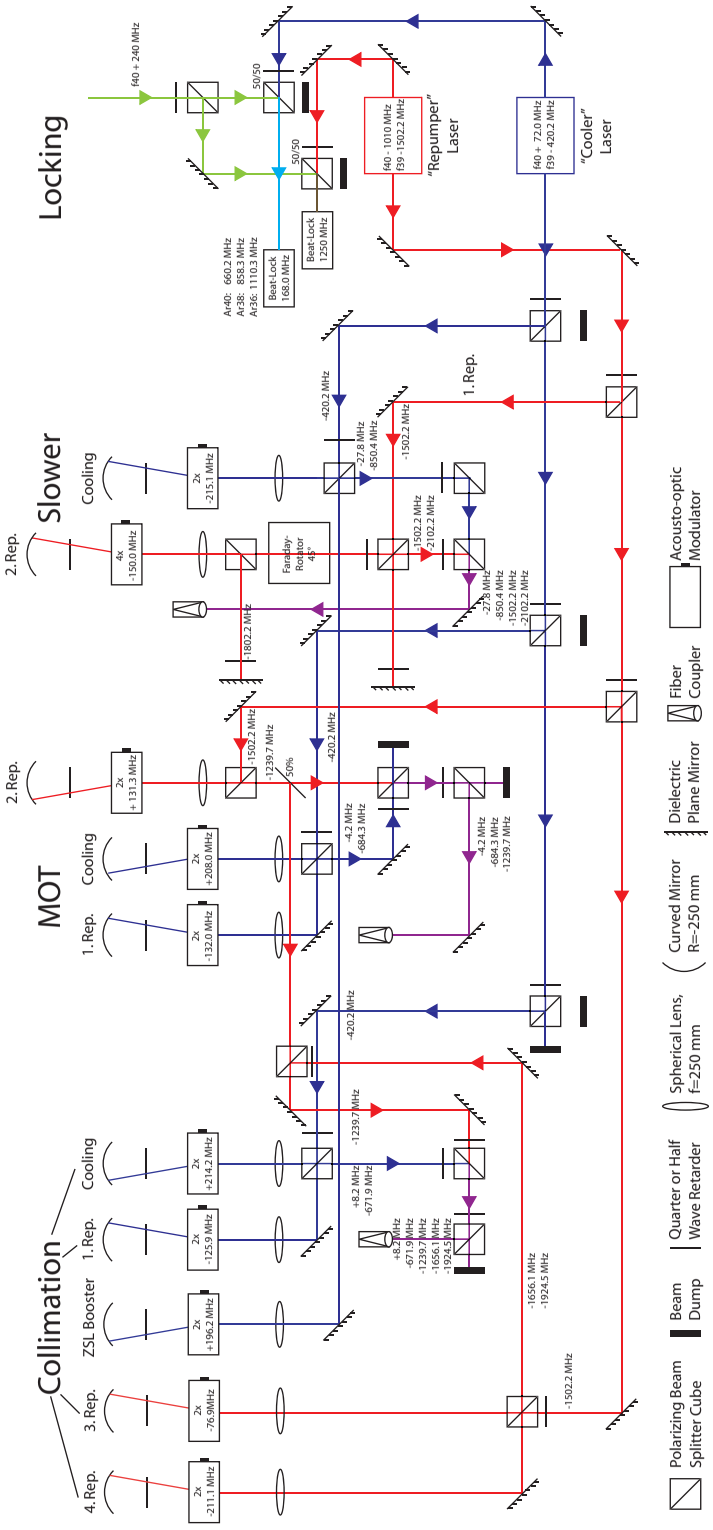

Figure 3.5.: Setup for beat-locking and sideband generation.

available laser power is not a limiting factor. Depending on the seed power, the output power may vary. This is especially critical for single atom detection in the MOT because it leads to drifts of the background photon rate. Therefore, the MOT-TA is stabilized to constant power in the MOT beams.
Fig. 3.6 illustrates the simultaneous amplification of different frequencies in the same TA chip. In this case, it is the Zeeman slower light as monitored by a scanned FPI but the outputs of the other TAs look similar. In principle, it works fine but under certain conditions an additional optical isolator right before or after the fiber is advantageous: A TA always also emits light via its input facet. This can be transmitted in reverse direction through the fiber and lead to disturbances in the AOM setup.

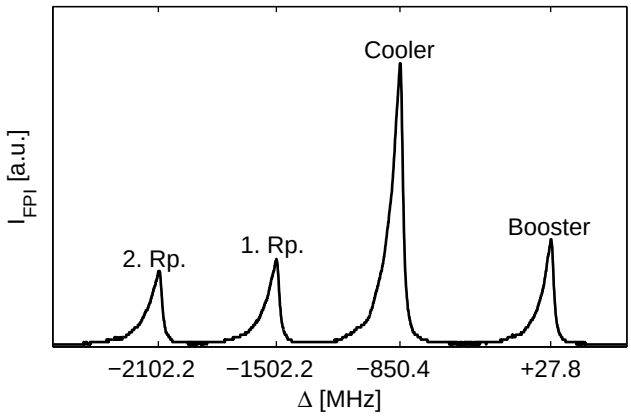

Figure 3.6.: Simultaneous amplification of different frequencies in one TA chip. The plot shows the transmission of Zeeman slower light through a Fabry-Pérot interferometer ($FSR =$ 1.5 GHz). The highest peak corresponds to the cooling light, the peak at higher frequency corresponds to the "booster" (which is introduced in sec. 4.6.2), and the other two are repumpers.

4. Atomic beam apparatus

4.1. Vacuum system

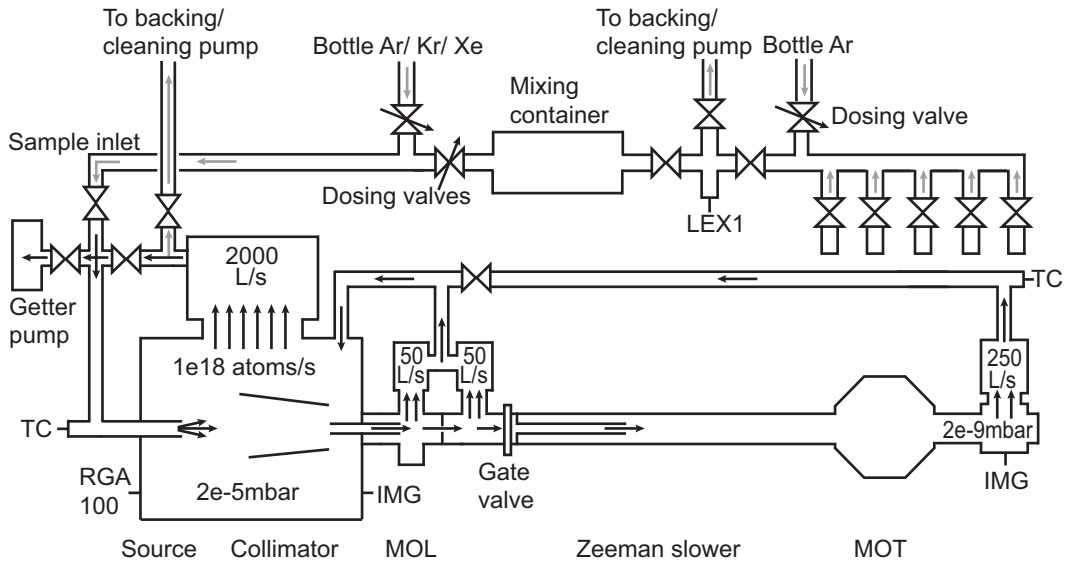

Figure 4.1.: Schematic drawing of the vacuum system. The solid black arrows represent the direction of gas flow in recycling mode. The gray-shaded arrows indicate optional bypasses for e.g. HV evacuation of the reservoir section to reduce cross sample contamination. Pumping speeds are given in numbers as well as the approximate pressures during operation. The apparatus runs with either atmospheric Ar/Kr/Xe from gas bottles or with enriched samples. These are mixtures of highly enriched gas samples with bottle-Ar. Abbreviations: TC - thermocouple gauge, IMG - Inverted Magnetron Gauge, RGA - Residual Gas Analyzer, LEX1 - Keller LEX1 gauge. Getter pump: SAES CapaciTorr D400. All other pumps: Varian turbomolecular pumps. Dimensions are not to scale.

The key to ^{39}Ar-ATTA is the setup of an atomic beam apparatus with maximum efficiency in terms of ^{39}Ar count rate. The first of several steps necessary is the design and implementation of a vacuum system that makes high sample throughput possible. At the same time, a sufficient vacuum level has to be maintained in the trap chamber to reduce collisional losses with the background gas.
In the source chamber, a 2000 l/s turbomolecular pump allows for 10^{18} atoms/s throughput at a pressure of $2 \cdot 10^{-5}$ mbar. Sample consumption can be minimized when the vacuum system operates in recycling mode. In this configuration the large pump serves merely as compressor and transports atoms back to the source reservoir. A steep pressure gradient between reservoir (10^{-1} mbar) and main chamber ($2 \cdot 10^{-5}$ mbar) is realized by a differential pumping stage right in front of the source tube. The getter pump connected to the

reservoir pumps most of the outgassing compounds except for CH_4 and noble gases. This enables for continuous operation in recycling mode because the resulting argon outgassing rate during source operation is less than 10^{-4} mbar $\cdot$ l $\cdot$ h^{-1}.
The metastable atoms necessary for atom optical manipulation are produced in a RF discharge source. Atoms emerge from the source and the metastable ones are optically collimated. The collimated atomic beam passes a series of differential pumping stages and is laser cooled, i.e. slowed down both transversally and longitudinally. A magneto-optical trap is realized in a compact chamber with several viewports under UHV conditions (pressure in the 10^{-9} mbar range).
Due to the low abundance of ^{39}Ar, most measurements for characterization or mechanical adjustment are done with ^{40}Ar or ^{38}Ar. ^{40}Ar is particularly useful for adjusting components related to the atomic beam, that is the source, the collimator, the magneto-optical lens and the Zeeman-slower. The measurements are then performed by fluorescence detection. Each atom in the beam scatters only few photons while passing the fluorescence volume, so as many atoms as possible have to be observed in order to have high signal quality.
The laser frequencies are set to ^{38}Ar for MOT optimization. For ^{40}Ar the MOT shows substantial saturation and a reduced lifetime compared to the single atom scenario. The reason are two body collisions between metastable atoms due to the large number density. Due to its smaller natural abundance the ^{38}Ar metastable flux is by a factor ≈ 1600 smaller than for ^{40}Ar, therefore saturation effects play less of a role.

4.2. Metastable beam source

Here an overview of the existing techniques to produce beams of metastable atoms is presented. Most of these metastable sources operate with discharges sustaining a plasma (see tab. 4.1, taken from [67]), which is why a detailed discussion of the relevant processes happening in such a plasma is essential. Keeping in mind what can be learned from an investigation on those processes, the different kinds of sources can be understood much better.

4.2.1. Excitation techniques

Optical excitation

Optical excitation schemes for the production of metastable noble gases usually require two intermediate states. The atoms in the source are irradiated with at least two different optical frequencies, one from the ground state to the first intermediate state and one from the first to the second intermediate state. From there the atom decays to the metastable state. A high flux atomic beam source has been realized for krypton at ANL [76].
Transferring the technique to produce metastable argon is problematic as the lowest states in krypton can be accessed with 124 nm light whereas 107 nm light is required for argon. At this wavelength most materials suitable for vacuum systems except for LiF are opaque. LiF itself is a further cause of problems due to its hygroscopic nature [77] which leads to severe degradation over time.

Table 4.1.: Comparison of different sources for the production of metastable atomic beams.

Element	Source type	Excitation technique	Throughput $\left[\frac{\text{atoms}}{\text{s}}\right]$	Metastable intensity $\left[\frac{\text{atoms}}{\text{s}\cdot\text{sr}}\right]$	Ref.
He	supersonic	DC	$1.2 \cdot 10^{19}$	$26.6 \pm 5.3 \cdot 10^{14}$	[68, 69]
He	supersonic	e^- beam	$2 \cdot 10^{21}$	$3 \cdot 10^{14}$	[70]
He	supersonic	DC	—	10^{14}	[71]
Ne	effusive	DC	—	$1 \cdot 10^{15}$	[72]
Ne	supersonic	DC	$8 \cdot 10^{18}$	$11 \pm 2.8 \cdot 10^{14}$	[68, 69]
Kr	effusive	microwave	$1 \cdot 10^{17}$	$7 \cdot 10^{14}$	[73]
Kr	effusive	optical	$3 \cdot 10^{17}$	$3 \cdot 10^{14}$	[74]
Kr	effusive	RF	$7 \cdot 10^{16}$	$4 \cdot 10^{14}$	[75]
Kr	supersonic	DC	$1.7 \cdot 10^{18}$	$4.3 \pm 2.2 \cdot 10^{14}$	[68, 69]
Ar	supersonic	DC	$2.4 \cdot 10^{18}$	$6.0 \pm 1.5 \cdot 10^{14}$	[68, 69]
Ar	effusive	RF	$1.5 \cdot 10^{18}$	$4 \cdot 10^{14}$	this work[a]
Ar	effusive	RF	$1.0 \cdot 10^{18}$	$5.7 \cdot 10^{14}$	this work[b]

[a] determined from fluorescence detection

[b] with Faraday cup (cup diameter 25 mm, distance 2.8 m, cup efficiency ≈ 0.15, measured metastable current 0.85 nA)

At this point a combination of several techniques might seem advantageous: population of the 1s states with a discharge and then transfer to $1s_5$ via optical pumping. However, in discharges the metastable $1s_5$ state is anyway much stronger populated than any other of the 1s states [43]. Thus, pumping atoms from one of those to $1s_5$ does not seem to be a promising way to boost the $1s_5$ population density.
Nevertheless, there might still be a way to overcome the major drawbacks of discharge sources (heating, implantation) if significant progress is achieved in the development of an argon UV excitation scheme. With the recent advances in the fields of table-top free electron lasers [78] or high-intensity rare gas discharge lamps [79] there might soon be new techniques available. Another possible excitation scheme might be via 2-photon or even 4-photon transitions with available diode lasers. Fig. 1.3 may serve to identify several possible transitions for optical pumping to $1s_5$.

DC discharge

Direct current glow discharges can be and have been used to produce metastable atomic beams. They consist of at least one pair of electrodes, one of which is on high voltage. The high voltage leads to acceleration of both ions and electrons and thus ion implantation in the material surrounding the discharge. It is therefore not an option for trace analysis as the risk of cross-sample contamination is obvious. Besides this, the DC discharge source in a former argon beam machine in Heidelberg produced only 10^{12} metastable atoms /s/sr, which is by more than two orders of magnitude less than what the RF discharge is capable of.

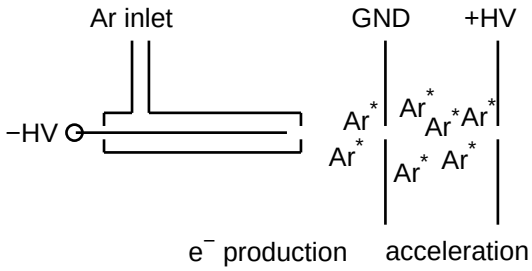

Figure 4.2.: A setup for the production of metastable noble gas atoms similar to [72]. The positive high voltage on the wire maintains the primary discharge for electron production. The flux of metastable atoms is greatly enhanced by the following acceleration stage.

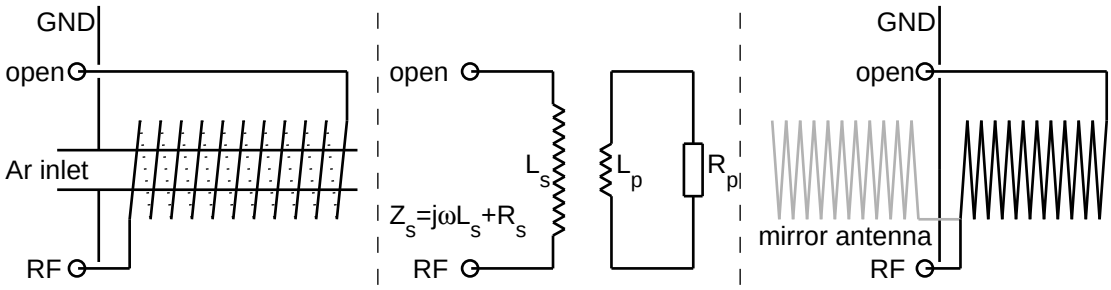

Figure 4.3.: Schematic of the RF discharge source with coil and source tube. The source tube length is $l \approx 125$ mm, and the diameter is $d \approx 11$ mm. The central image shows an equivalent circuit diagram which models the plasma as secondary coil (one winding) of a transformer with a lossy dielectric inside. An alternative description would be that of a helical quarter-wave monopole antenna as in the right-hand picture. The ground plane actually provides a mirror antenna such that a dipole antenna is formed.

AC discharge

Alternating current discharges partially overcome the drawbacks of DC discharges while leading to even higher metastable fluxes. In the broader context of ATTA experiments microwave radiation powered discharges have been realized [73] as well as radio frequency (RF) discharges [75]. RF discharges are widely used in industrial applications such as plasma surface coating and components in the HF and VHF range are readily available. Therefore the present setup focuses on the implementation of a RF driven atomic beam source.
Yet, it has to be mentioned that a electrostatic sheath layer is present not only in DC discharges but also in RF driven plasmas, see fig. 4.4. This is due to the different velocity and mobility of ions and electrons which leads to a charge imbalance close to the plasma boundaries. Consequently, RF plasmas can also have relatively high sheath voltages which lead to undesired implantation of ions into the discharge tube.
Several pictures serve for describing different aspects of the RF plasma as illustrated in fig. 4.3. The obvious is a mechanical one: a plasma is formed in a glass tube surrounded by a coil and powered by radio frequency. In order to calculate the relevant plasma parameters the equivalent circuit diagram is a useful tool. Experimental observations show that a resonant antenna is advantageous for producing large metastable fluxes. The length of

the used wire should approximately equal the wavelength times a velocity factor [80], [81]. A fudge factor comes into play when the special helical structure is to be considered[1]. Besides this, it has to be kept in mind that a well-conducting ground plane is obligatory as the antenna is actually a dipole antenna. The other half of the dipole is provided by the ground plane forming a mirror antenna. Given the fact that the vacuum parts here are made from stainless steel with poor conductivity the performance might be improved with an additional copper plate or silver coating of the flange.
Examples where the relevant plasma parameters are explicitly calculated are given in [83] (and more compact [84]). A similar calculation can be done for the present case where the plasma length $l \approx 125$ mm, the radius $R \approx 6$ mm, the absorbed power $P \approx 50$ W and the frequency $f = 168$ MHz. This results in $R_p \approx 0.01\ \Omega$ and $X_p \approx 0.3\ \Omega$. However, the significant quantity is the impedance seen by the RF generator. In the transformer picture this computes to $R_s = N^2 \cdot R_p$ where N is the number of coil windings (here $N \approx 10$). The reactance is simply $X_s = \omega L_s$.

4.2.2. Plasma model

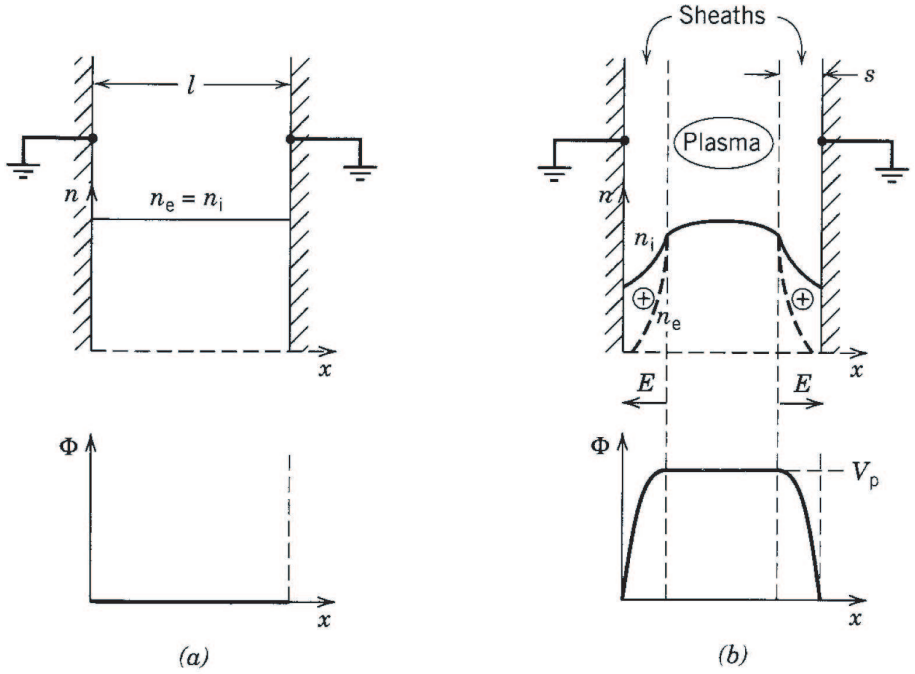

Figure 4.4.: The formation of plasma sheaths: (a) initial ion and electron densities and potential; (b) densities, electric field, and potential after formation of the sheath; copied from [83].

As already indicated in table 4.1, the most efficient metastable sources feature a plasma powered by a RF field. In order to develop a better understanding of the processes gov-

[1]There are two different types of helical antennae, distinguished by their radiation pattern. For diameters much less than the wavelength the antenna operates in "normal-mode" radiating mostly perpendicular to the antenna axis. When the wavelength is on the order of the diameter it operates in "axial mode" and radiation much more directed along the antenna axis [81], [82].

erning metastable production, a two step model is applied.
First, the relevant plasma parameters such as electron temperature T_e and electron density n_e are calculated. M. Lieberman presents an excellent example of a plasma model in [83], hence the following calculation uses a similar approach.
In the second step, the excitation and loss rates for metastable argon atoms are derived from the available data on collisional cross-sections and the previously calculated plasma parameters. This allows for calculation of both the metastable density at any point in the discharge tube and the probability of an atom to "survive" in the metastable state until it emerges from the source tube.
The previously mentioned Lieberman model calculates plasma densities for uniform pressure in a plasma chamber. Hence, regarding the context of an atomic beam source, the model has to be extended. It has to be adapted to the present experiment such that it takes the pressure gradient in the discharge tube into account which leads to all parameters being pressure, or respectively position, dependent.
Furthermore, experimental observations indicate that there is a threshold for plasma operation. Depending on pressure and available RF power the plasma extends more or less into the main chamber. This phenomenon has to be taken into consideration by establishing a "cutoff"-length in the model. Nevertheless, this adapted model still has its shortcomings. The most important one of those is the yet unresolved issue of the power dissipation pattern[2].
During the calculation of the plasma parameters, the electron density in the plasma is assumed to be equal to the ion density, $n_e = n_i$, which is the quasi-neutral plasma approximation for a vanishing density of negatively charged ions. But strictly speaking, this is only valid for the central region of the plasma as the build-up of an electro-static sheath close to the plasma boundaries leads to a stronger depletion of the electron density in the boundary region, see fig. 4.4.
In the following a brief outline of the plasma model is given. Starting from the pressure in the main chamber and the geometry of the source tube, the position dependent density of ground state atoms n_g is obtained. Due to the fact that the atoms and ions in the discharge have a relatively low temperature, the collisional energy for ion-atom collisions is low. The cross section $\sigma_i g$ for these collisions can be derived from fig. 4.5, which, together with n_g, leads to the corresponding mean free path λ_i for ions.
Combined with the geometrical restrictions of the plasma, namely length l and radius R, an effective plasma size d_{eff} and an effective area A_{eff} for energy transport to the wall can be calculated. These effective plasma size parameters deviate from the geometrical size parameters. They originate from a heuristic solution of the density profile at low pressures, where the collisionless plasma edge[3] begins to play a significant role.
From n_g and d_{eff} the mean electron temperature T_e can be derived, and results for the present source setup are illustrated in fig. 4.6. Furthermore, the Bohm velocity u_B (the velocity of ions at the plasma sheath edge) can be directly obtained from T_e.

[2] Basically, a solution in between two extreme scenarios seems reasonable. Either, the power is distributed uniformly over the whole discharge or its distribution pattern follows the pressure gradient. The first scenario is reasonable as the vacuum wavelength at 168 MHz is about 2 m which is much larger than the dimensions of the plasma. Nevertheless, the antenna is operated close to a resonance where a standing wave forms on the coil wire. This latter scenario seems as well plausible. Clearly, this requires further investigation.

[3] This is the region in direct vicinity to the wall, where the mean free path is larger than the distance to the wall

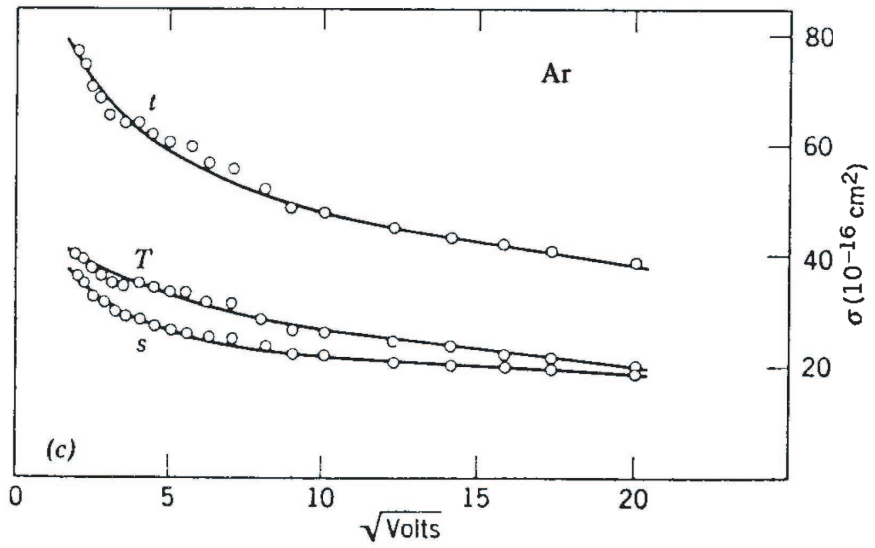

Figure 4.5.: Experimental values for elastic scattering (s), charge transfer (T), and the sum of the two mechanisms for argon ions in their parent gases, copied from [83]. x-axis: collisional energy, y-axis: collisional cross-section.

Each creation of an electron-ion pair leads to a loss of collisional energy, E_c, from the

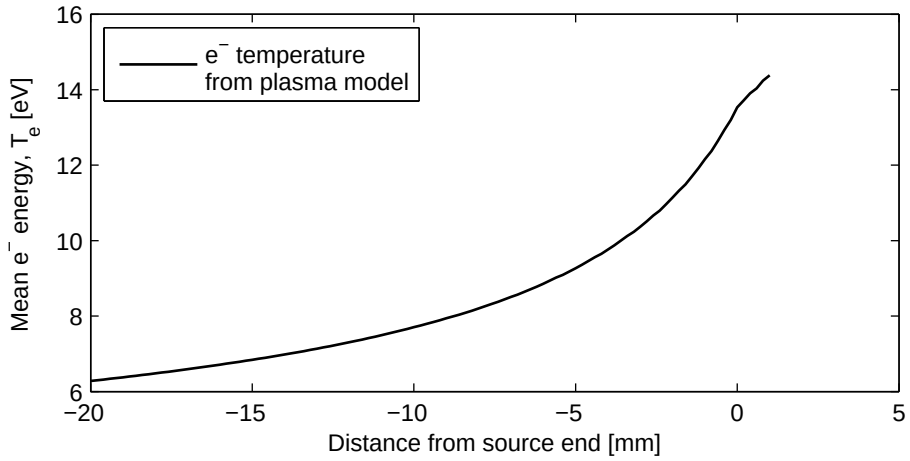

Figure 4.6.: The mean electron temperature as derived from [83] for $2 \cdot 10^{-5}$ mbar pressure in the main chamber and a glass tube of 125 mm length and 5.5mm radius.

system. Ions hitting the surface surrounding the plasma lead to a further loss of kinetic energy, E_i. Likewise, electrons hitting the wall also correspond to a loss of kinetic energy, the mean loss is $2 \cdot e \cdot T_e$ for electrons from a Maxwell-Boltzmann energy distribution.
Each of these contributions can be calculated from the mean electron temperature T_e. Accordingly, $E_T = E_c + 2T_e + E_i$ is the total energy equivalent temperature lost per ion that hits the wall of tube. As most of the plasma calculations use energy equivalent temperatures, the physical quantity "energy" is calculated as $\varepsilon_T = e \cdot E_T$.
Energy conservation demands that the power that is fed into the plasma has to be dissi-

pated, most likely into the wall. The particle flow of ions to the wall is $n_i \cdot u_B \cdot A_{eff}$ which leads to the following relation between plasma density and absorbed power P_{abs}:

$$n_i = \frac{P_{abs}}{u_B \cdot A_{eff} \cdot e \cdot E_T} \tag{4.1}$$

As mentioned earlier, the electron density n_e is assumed to be equal to the ion density n_i. Hence, having now calculated the ion density from plasma size parameters and energy conservation, the electron density necessary for the calculation of the metastable production and loss rates is likewise available.

4.2.3. Metastable density model

Table 4.2.: An overview of metastable density at different pressures and for different excitation schemes from available data in literature. The choice of a RF discharge is obvious as it achieves the highest efficiency.

Pressure [mbar]	Excitation method	Metastable density [m^{-3}]	Efficiency	Ref.
0.0013	ECR[a]	10^{15}	$3.3 \cdot 10^{-5}$	[85]
0.013	ICP[b]	$1.2 \cdot 10^{18}$	$3.7 \cdot 10^{-3}$	[43]
0.02	ICP	$1.9 \cdot 10^{17}$	$4 \cdot 10^{-4}$	[86]
0.05	DC[c]	$\approx 10^{18}$	$\approx 10^{-4}$	[87]
0.066	RF cap.[d]	$1.5 \cdot 10^{15}$	$9.3 \cdot 10^{-7}$	[88]
0.1	DC	$2 \cdot 10^{17}$	$8 \cdot 10^{-5}$	[89]
0.133	RF cap.	$1.7 \cdot 10^{18}$	$5.3 \cdot 10^{-4}$	[90]
0.4	RF	$1.1 \cdot 10^{17}$	$1.1 \cdot 10^{-5}$	[91]
50	DC	$2.0 \cdot 10^{20}$	$1.7 \cdot 10^{-4}$	[92]

[a] Electron Cyclotron Resonance
[b] Inductively Coupled Plasma
[c] Direct Current Discharge
[d] Radio frequency capacitively coupled

Several important conclusions can be drawn from the available literature prior to developing a metastable production model for this specific application. Tab. 4.2 summarizes both calculated and measured metastable densities for the $1s_5$-state in ^{40}Ar. Again, RF discharges seem favorable as they lead to the highest metastable excitation efficiency.
Under the assumption that the populations of the different atomic states are in a local steady-state, the metastable density can be calculated for each point along the source tube. This local steady-state can be understood such that the processes leading to population and depletion of an atomic state happen faster than the atoms move along the discharge tube. The residence time of an atom in the tube is on the order of a couple of ms whereas the metastable production rate is on the order of kHz and the loss rates range between kHz and MHz. Thus, to a certain degree the assumption of a local steady state is justified. Hence, the continuity equation has to hold for metastable atoms at each point of the

source,

$$\dot{n}_m - D_m \cdot \frac{\partial^2 n_m}{\partial z^2} = 0, \tag{4.2}$$

where n_m is the density of metastable atoms and D_m the metastable diffusion coefficient. Early diffusion measurements with metastable argon atoms in argon gas discharges as presented in [93] lead to

$$D_m = 4.3 \cdot 10^{-7} \frac{\mathrm{m}^2}{\mathrm{s}} \cdot \frac{(\frac{T}{\mathrm{K}})^{1.68}}{\frac{p}{\mathrm{mbar}}} \tag{4.3}$$

is the pressure and temperature dependent diffusion coefficient for metastable argon atoms in argon. Using the formula for the diffusion coefficient from Chapman-Enskog theory ([94]), the cross section for collisions between metastable atoms and ground state argon atoms is computed to

$$\sigma_{mg} \approx 300 \text{ Å}^2. \tag{4.4}$$

The $\dot{n}_m$ term in 4.2 includes all production and loss processes of metastable atoms apart from the diffusive loss. Production of metastable atoms (denoted as Ar^*) can take place via different mechanisms:

direct excitation from ground state:	$\mathrm{Ar} + \mathrm{e}^- \rightarrow \mathrm{Ar}^* + \mathrm{e}^-$
direct e^--impact exc. from 1s states:	$\mathrm{Ar}(\mathrm{s_j}) + \mathrm{e}^- \rightarrow \mathrm{Ar}^* + \mathrm{e}^-$
indirect e^--impact exc. from 1s states:	$\mathrm{Ar}(\mathrm{s_j}) + \mathrm{e}^- \rightarrow \mathrm{Ar}(\mathrm{p_k}) + \mathrm{e}^- \rightarrow \mathrm{Ar}^* + \mathrm{e}^- + h\nu$
ion-impact excitation:	$\mathrm{Ar} + \mathrm{Ar}^+ \rightarrow \mathrm{Ar}^* + \mathrm{Ar}^+$
radiative recombination:	$\mathrm{Ar}^+ + \mathrm{e}^- \rightarrow \mathrm{Ar}^* + h\nu$

The second mechanism represents excitation from one metastable or resonant level[4] to a metastable state. The third mechanism represents excitation from one metastable or resonant level to an excited state with cascading to a metastable level, respectively. Given the available electron and ion energies and densities, the excitation via the last two channels can well be neglected and excitation from other s_i-levels only becomes important for high electron temperatures (see [96, 89, 97, 98, 87, 95]).
The $1\mathrm{s}_5$ state has been found to be about 6 times stronger populated than the other metastable state $1\mathrm{s}_3$ or the two resonant states [43]. Therefore, transitions from these states do not or only weakly contribute to the $1\mathrm{s}_5$ population. Nevertheless, atoms can still be pumped from $1\mathrm{s}_5$ to one of the other states which is why those transitions are taken into account as loss mechanisms. Consequently, the following calculation applies only for the $1\mathrm{s}_5$ population density.
The local excitation rate constant $k_{gm}(T_e)$ is obtained by integrating the total electron impact cross section (first three mechanisms, see [99, 100]) over the electron energy distribution corresponding to T_e at this position. In general, rate constants can be calculated from the corresponding cross section and the energy distribution $f(\varepsilon, T_e)$:

$$k(T_e) = \int_0^\infty f(\varepsilon, T_e) \cdot \sigma(\varepsilon) \cdot v(\varepsilon) \mathrm{d}\varepsilon = \langle \sigma(\varepsilon) \cdot v(\varepsilon) \rangle_{T_e} . \tag{4.5}$$

[4]The resonant levels are those that can be directly excited optically from the ground state, which are $1\mathrm{s}_4$ and $1\mathrm{s}_2$. In plasmas they are often found to be radiation trapped (depending on the pressure) as the excitation and decay rates can become similar [95]. That means that the light emitted by one atom is simply resonantly absorbed by another atom.

The electron energy distribution is assumed to follow a Maxwell-Boltzmann distribution (MBD), which writes in terms of energy as

$$f(\varepsilon, T_e) = \frac{2}{\sqrt{\pi}} \cdot \frac{\sqrt{T(\varepsilon)}}{T_e^{3/2}} \cdot e^{-T(\varepsilon)/T_e}. \tag{4.6}$$

In order to get a feeling for the efficiency of electronic excitation, it is useful to compare

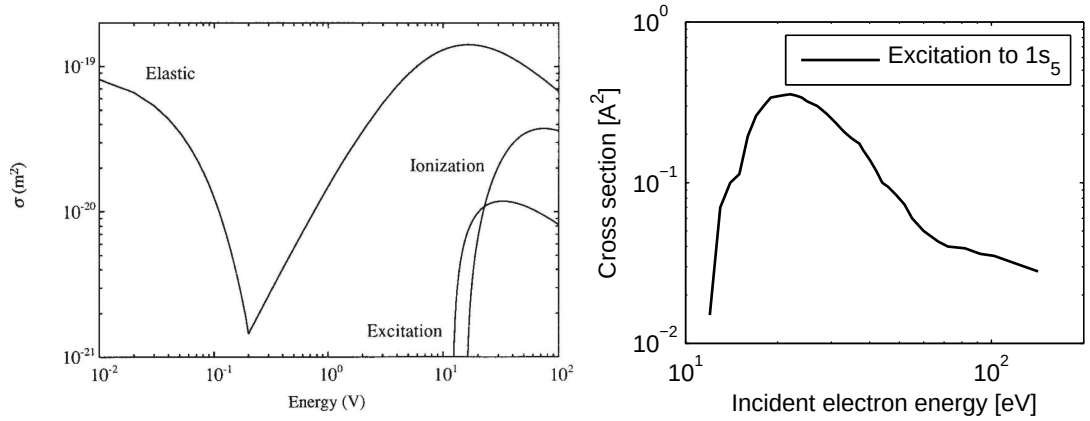

Figure 4.7.: Left-hand: Ionization, excitation and elastic cross-sections for electrons in argon gas, copied from [83]; Right-hand: Measured cross-section for excitation to the $1s_5$ level in argon, copied from [100].

the collisional cross section with the cross section for excitation. In [83] the first one is found to be about 10 $Å^2$ (left-hand plot in fig. 4.7) whereas the latter is found to be approximately 0.1 $Å^2$ in the energy range of interest (right-hand plot in fig. 4.7, see [99, 100]). Hence only every hundredth collision between a ground state atom and an electron leads to excitation to a metastable state. The majority of all collisions are simply elastic scattering of electrons, while about one in ten collisions with a fast electron leads to ionization of the atom[5].

Regarding the loss channels, again a multitude of possible processes come into play (for a detailed overview see [98, 101]), most of which are negligible. Yet, some of them are briefly discussed as they help to complete the picture of what happens to metastable atoms in this experiment.

Diffusive loss of metastable atoms to the wall is the predominant loss channel inside the source tube. Whenever a metastable atom hits the wall of the discharge tube it is de-excited to the ground state. The rate for diffusive loss is derived with the help of eqs. 4.2 and 4.3. While introducing a characteristic diffusion length Λ, the diffusive loss rate is found to be

$$r_D = -n_m \cdot \frac{D_m}{\Lambda^2}. \tag{4.7}$$

For the cylindrical source geometry the following relation applies to Λ [102]:

$$\frac{1}{\Lambda^2} = \left(\frac{2.405}{R}\right)^2 + \left(\frac{\pi}{l}\right)^2. \tag{4.8}$$

[5]The minimum energy of the electron has to be 15.76 eV which is the ionization energy of argon atoms. The ground state atom itself has only a low kinetic energy of about 0.03 eV.

Outside of the source tube, diffusion is not anymore considered as a loss channel, because there it corresponds to the actual emission of metastable atoms from the source. The second most important loss mechanism is electron-impact excitation of metastable atoms. This becomes dominant just after emission from the source. Basically three processes with similar contributions to the loss rate are related to this:

$$\begin{aligned} \text{e}^-\text{-impact excitation and cascading:} \quad & \text{Ar}^* + \text{e}^- \rightarrow \text{Ar}(\text{p}_\text{k}) + \text{e}^- \rightarrow \text{Ar}(\text{s}_\text{j}) + \text{e}^- + h\nu \\ \text{direct e}^-\text{-impact excitation:} \quad & \text{Ar}^* + \text{e}^- \rightarrow \text{Ar}(\text{s}_\text{j}) + \text{e}^- \\ \text{e}^-\text{-impact ionization:} \quad & \text{Ar}^* + \text{e}^- \rightarrow \text{Ar}^+ + 2\text{e}^- \end{aligned}$$

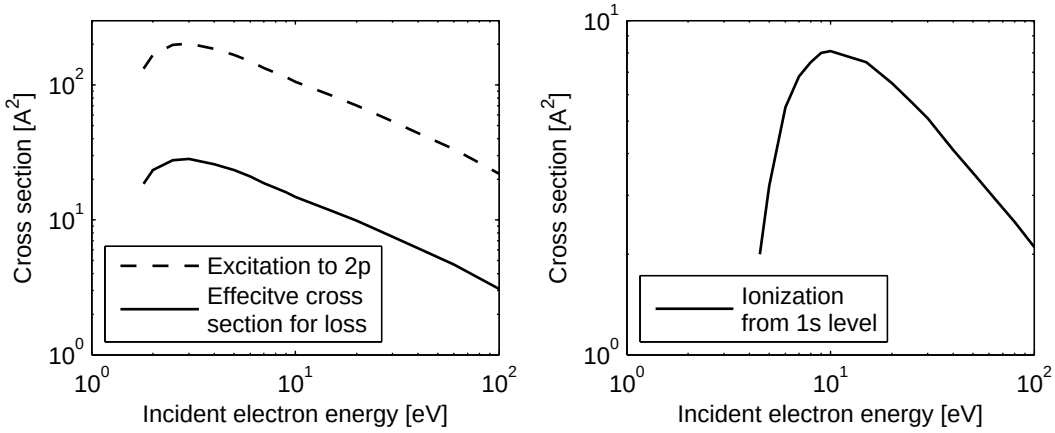

Figure 4.8.: Left-hand: Dashed line: Average electron impact cross-section for transfer from 1s to 2p, copied from [103], solid line: effective cross-section for loss of $1s_5$ atoms; Right-hand: Electron impact cross-section for ionization of 1s atoms, copied from [104].

Average cross sections σ_{sp} for electron-impact excitation from any of the 1s levels to the 2p multiplet can be found in [103], see fig. 4.8. The cross section for transfer from one $1s_i$ level to one specific $2p_k$ level is calculated by

$$\sigma_i^k = \sigma_{sp} \cdot \frac{f_{ik}}{\sum_k f_{ik}}, \tag{4.9}$$

where f_{ik} is the experimentally observed line strength for the transition $1s_i$-$2p_k$. For each of the $2p_k$ levels the probability to decay back to the initial $2s_i$ state is found by the branching ratio

$$\delta_k^i = \frac{A_{ki}}{\sum_i A_{ki}}, \tag{4.10}$$

with the Einstein coefficients A_{ki}. Consequently, the collision energy dependent effective cross section for pumping atoms from $1s_i$ to any other 1s level via all possible $2p_k$ levels is

$$\sigma_{ij}^k(\varepsilon) = \sigma_{sp}(\varepsilon) \cdot \sum_k \left[(1 - \delta_k^i) \cdot \frac{f_{ik}}{\sum_k f_{ik}} \right], \tag{4.11}$$

and especially from $1s_5$ to any other 1s level

$$\sigma_{5j}^k(\varepsilon) \approx 0.14 \cdot \sigma_{sp}(\varepsilon). \tag{4.12}$$

This has been explicitly calculated but as the necessary line strengths and coefficients can be found online ([105]) they are not listed here. The important result is that the effective cross section for losses from the $1s_5$ level via electron-impact excitation and subsequent cascading is just 14% of the cross section for excitation, reflecting that decay back to the initial state is highly probable. The rate constant is

$$k_{exc} = \left\langle \sigma_{5j}^{k}(\varepsilon) \cdot v(\varepsilon) \right\rangle_{T_e} . \tag{4.13}$$

The rate constant k_r for direct transfer from $1s_i$ to $1s_j$ via electron-impact is often assumed to be constant ($k_r = 2 \cdot 10^{-13}\mathrm{m}^3/\mathrm{s}$, [97]), independent of the electron energy. However, the results from [106] clearly show the opposite. This is accounted for in the following by using a modified $k_r(T_e)$ instead, weighted by the Maxwellian electron energy distribution. For losses by ionization the corresponding cross section can as well be taken from literature, see [104] and fig. 4.8. The rate constant is again obtained by

$$k_{iz} = \langle \sigma_{iz}(\varepsilon) \cdot v(\varepsilon) \rangle_{T_e} . \tag{4.14}$$

Interestingly, losses via collisions between metastable atoms or between ground state atoms and metastable atoms do not play a significant role inside the source tube. k_{mm}, the rate constant for metastable-metastable collision, is found to be

$$k_{mm} = 6 \cdot 10^{-16}\mathrm{m}^3/\mathrm{s} \text{ , [97].} \tag{4.15}$$

Division by the mean relative speed[6] leads to $\sigma_{mm}^{loss} \approx 100$ Å^2. The collisional cross section between metastable atoms is calculated with the help of eq. 4.4 to be $\sigma_{mm} \approx 800$ Å^2.[7]
Hence only one in eight collisions results in $\mathrm{Ar}^* + \mathrm{Ar}^* \rightarrow \mathrm{Ar} + \mathrm{Ar}^+ + \mathrm{e}^-$. Given the low density and the low relative speed this process can be neglected here. Nevertheless, in a dense magneto-optical trap it leads to saturation.
Two-body quenching, $\mathrm{Ar}^* + \mathrm{Ar} \rightarrow 2\mathrm{Ar}$, has a small rate constant of only

$$k_{2B} = 2.1 \cdot 10^{-21}\mathrm{m}^3/\mathrm{s} \text{ , [97].} \tag{4.16}$$

Similar to the above the cross section for loss found to be $\sigma_{2B}^{loss} = 3.7 \cdot 10^{-4}$ Å^2. Compared to eq. 4.4 the difference is nearly 6 orders of magnitude. As already mentioned, the ground state atom has about 0.03 eV kinetic energy. The mean collisional energy for this process is 11.548 eV + 2 · 0.033 eV = 11.614 eV which is still less than the energy of the adjacent $1s_4$ level (11.624 eV). Furthermore, in a very classical picture, only a small fraction of the kinetic energy of the ground state atom can actually be transferred to electrons of the metastable atom. Momentum and energy conservation lead to $\Delta E \approx 4m_e/m_{atom} \cdot E_{kin} \approx 1/18362 \cdot E_{kin}$. Therefore, it is not likely that metastable atoms are de-excited via this mechanism.
Again, for atoms in the MOT it plays an important role: the collision is elastic which means that momentum is transferred to trapped atoms. Having an atom with 400 m/s hit

[6] The mean relative speed of two atoms v_{rel}^- is $\sqrt{2}\bar{v}$. For derivation: $v_{rel} = \sqrt{(\mathbf{v_2} - \mathbf{v_1})^2} = \sqrt{\mathbf{v_2^2} - \mathbf{2 \cdot v_2 \cdot v_1} + \mathbf{v_1^2}}$. The mixed terms can simply be canceled out due to the random distribution of velocities.

[7] The calculation uses the geometrical scattering cross-section: $\sigma_{mg} = \pi \cdot (r_g + r_m)^2 \approx 300$ Å^2, $r_g = 188$ pm $\Rightarrow r_m \approx 789$ pm $\Rightarrow \sigma_{mm} = \pi \cdot (2 \cdot r_m)^2 = 783$ Å^2.

an atom at rest, the atom in the trap will simply be kicked out of the trap. Its resulting kinetic energy is most probably far larger than the capture limit of the trap. Thus, the atom stays in the metastable state but will ultimately be de-excited when colliding with the trap chamber.
In principle, de-excitation by collisions with ions is also possible. Unfortunately, this topic is rarely treated in literature. However, an estimate for the rate constants can be given by the following argument. Collisions between ions and metastable atoms should not be fundamentally different from collisions between ions and ground state atoms. Thus the collision cross section should be comparable to fig. 3.15 in [83] (100 Å^2). Given the low relative speed, the rate constant is estimated to $k_{im} \leq 5 \cdot 10^{-16}\text{m}^3/\text{s}$. This is about 2.6 orders of magnitude lower than the rate constant for losses due to electrons. As the electron and ion densities are similar this process can well be neglected.
Based on the previously derived plasma parameters the production and loss rates at each point along the source tube can now be calculated by rewriting eq. 4.2 and keeping only the significant terms:

$$n_g \cdot n_e \cdot k_{gm} - n_m \cdot \left(n_e \cdot (k_{exc} + k_r + k_{iz}) + \frac{D_m}{\Lambda^2} \right) = 0. \tag{4.17}$$

Solving this for n_m leads to the local metastable density:

$$n_m = \frac{n_g \cdot n_e \cdot k_{gm}}{n_e \cdot (k_{exc} + k_r + k_{iz}) + \frac{D_m}{\Lambda^2}}, \tag{4.18}$$

where all parameters implicitly or explicitly depend on the position along the source tube. With a similar calculation it is possible to derive the excitation probability density ρ_{exc} for atoms as they move along the source. Then, this can be convolved with the probability to be still in the metastable state when the atoms leave the discharge. By this $\rho_{exc+surv}$ is obtained. An exemplary result for the experimentally optimized source parameters is shown in fig. 4.9. η, the production density is obtained by integration of $\rho_{exc+surv}$ over the whole discharge region. The results indicate that mostly atoms that are produced in the last 10 mm of the discharge actually contribute to the production efficiency.
The dependence of the source efficiency on parameters like RF power, gas temperature, source tube radius or throughput (measured by the pressure in the main chamber) is illustrated in figs. 4.10 and 4.11. For each of the plots two parameters are kept constant at the values experimentally found to be optimal.
The metastable flow, which is proportional to the product of efficiency and pressure, is depicted in fig. 4.12. Basically the same results as in fig. 4.11 are presented but additional losses due to metastable-ground-state collisions along 40 cm of further propagation in the source chamber are taken into account. These are computed with the help of above the σ_{mg} (eq. 4.4).
Even though the metastable density calculation as well as the plasma model use many approximations the combined model reproduces the experimentally optimized parameters to some extent. Especially, the calculated source efficiency of $1.3 \cdot 10^{-3}$ agrees quite well with the experimental value of $1.8 \cdot 10^{-3}$ (last row in table 4.1).
The results in fig. 4.9 might be used for further improvement of the metastable source. It might be beneficial to use a positively charged electrode in a certain distance from the source exit. On the one hand this could help to repel ions, which would otherwise be implanted into e.g. the collimator mirrors. On the other hand, electrons would be drawn

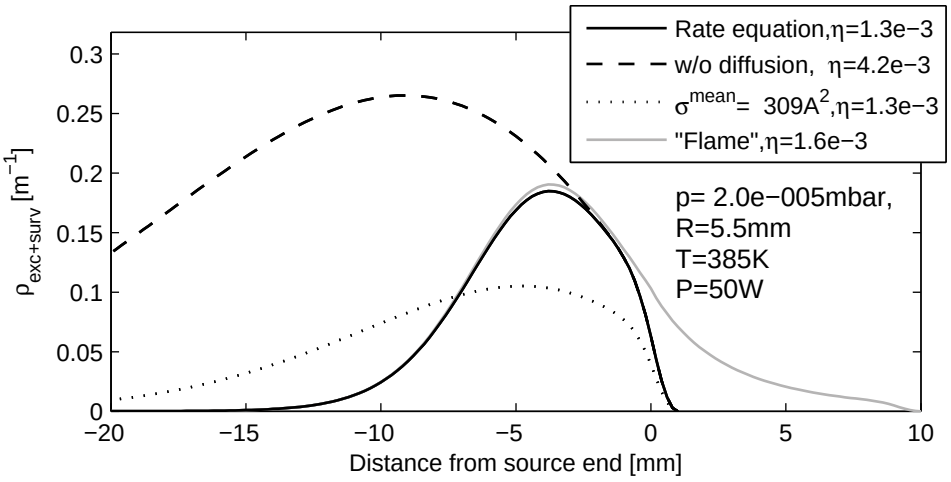

Figure 4.9.: The local metastable production density multiplied by the probability to survive until the end of the source can be integrated to obtain the source efficiency. Solid line: results obtained by solving the rate equation with a plasma cutoff at 1 mm behind the tube end. Dashed line: same without diffusive loss. Gray curve: plasma extends further into the main chamber thus increasing the efficiency. Dotted curve: fitted from a simple model to reproduce the same efficiency. The simplified model assumes a uniform cross section for loss.

towards this electrode, hence effectively increasing the electron density close to the source exit. This could further enhance the metastable flow, but is subject to future investigations.

4.2.4. Characterization of the source

This section compiles several key properties of the atomic beam source. Detailed insight into the methods used for measuring the metastable flux and additional information is provided in [107]. Fig. 4.13 for example illustrates how the velocity distribution is obtained from both absorption and fluorescence measurements. The longitudinal fluorescence is measured 40 cm downstream of the source whereas absorption is measured directly behind the source. The peak at $v = 0$ is produced by transversal fluorescence and serves as marker. Frequency calibration is done with the help of a Fabry-Pérot interferometer with ≈ 83 MHz free spectral range.
The speed of atoms emitted from the source in axial direction does not follow a MBD as would be naively expected. Certainly, such a behavior is found for atoms inside the source. But fast atoms travel a larger distance in a given time interval than slow atoms. Consequently they hit the walls of the tube more often. This "wall-hitting-frequency" is proportional to the velocity v. Thus, fast atoms are by a factor $\propto v$ more likely to be emitted from the source[8]. The on-axis atomic velocity distribution is therefore rather

$$f(\theta = 0, v) \propto v^3 \cdot e^{\frac{-v^2}{\hat{v}^2}} \tag{4.19}$$

[8]Strictly speaking, this is only true for a large source vessel with a small opening. Depending on the source geometry, an emission distribution somewhere in-between eq. 4.19 and a MBD may occur.

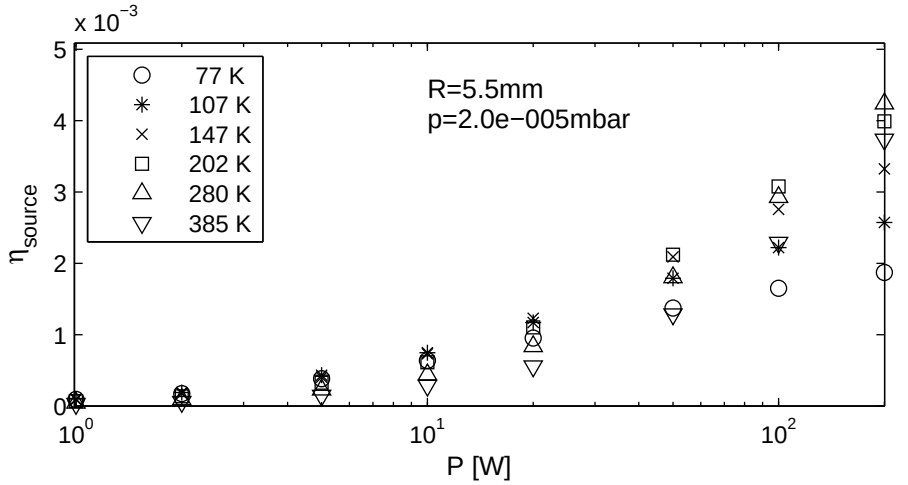

Figure 4.10.: Calculated dependence of the source efficiency on variable RF power and gas temperature at constant tube radius and throughput. The efficiency shows saturation with increasing RF power (note the logarithmic x-axis) and is not found to be strongly dependent on the source temperature.

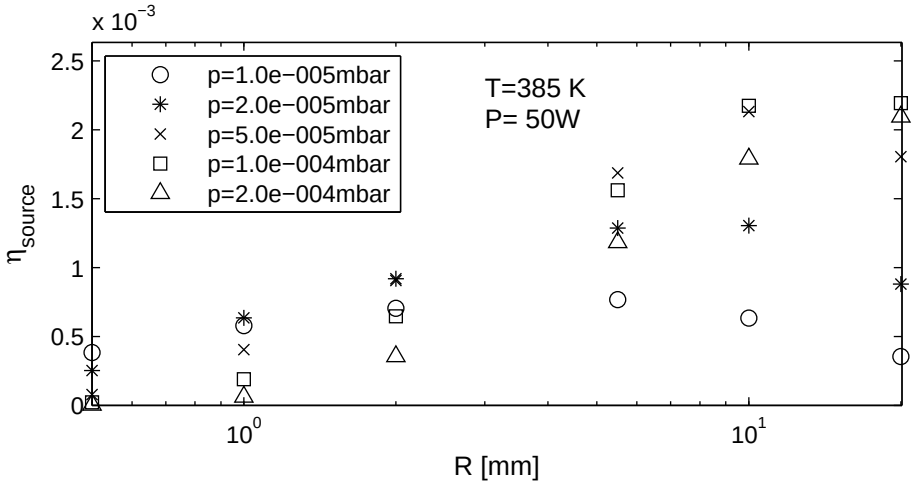

Figure 4.11.: Calculated dependence of the source efficiency on variable tube radius and throughput at constant RF power and gas temperature. The results indicate that with increasing pressure the efficiency peaks at higher radii. In a simple picture more atoms can be pumped through a larger tube in order to obtain a comparable optimum density close to the source exit.

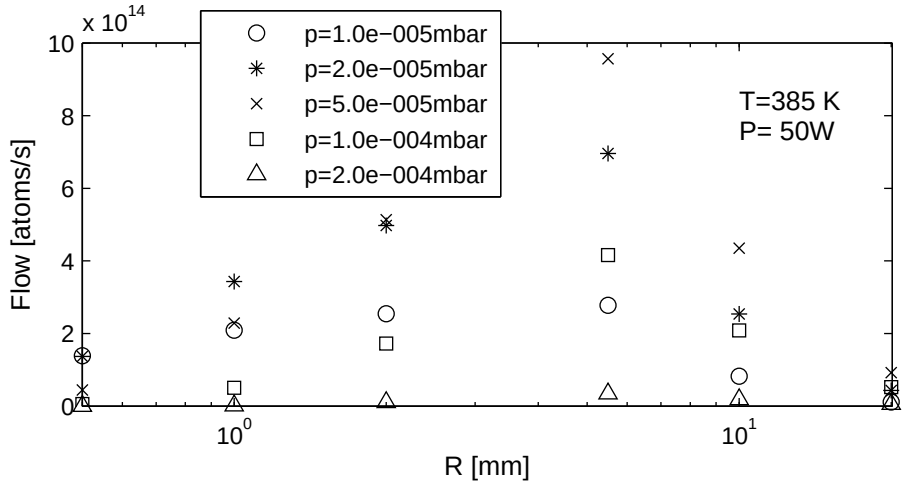

Figure 4.12.: Dependence on the metastable flow after the main chamber on variable tube radius and throughput at constant RF power and gas temperature. The experimentally optimized parameters ($R = 5.5$ mm, $p_{main} = 2 \cdot 10^{-5}$ mbar) are found to be close to the optimum. The results take the limit for the atomic beam diameter given by the collimator laser beams and the differential pumping stage into account. Thus tube radii of more than ≈ 6 mm are disadvantageous. The detection efficiency decreases with increasing p as the MOT lifetime decreases. Hence, pressures higher than $2 \cdot 10^{-5}$ mbar prove to be disadvantageous.

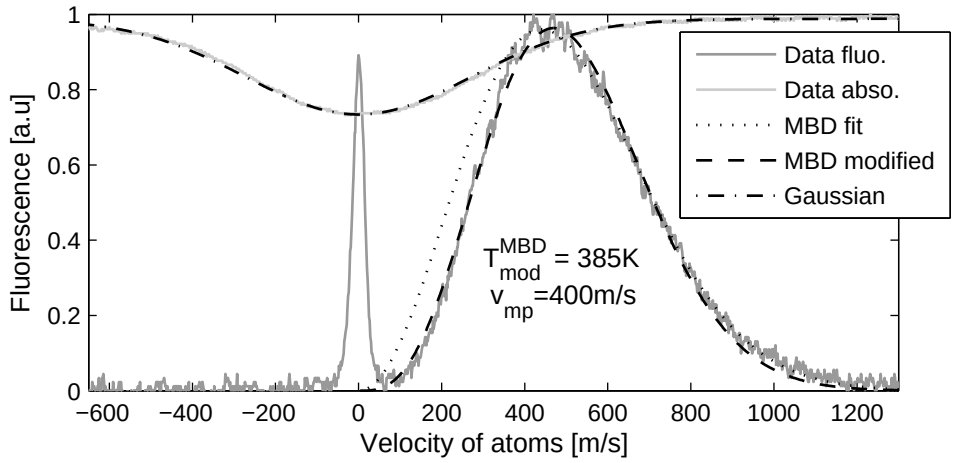

Figure 4.13.: Atomic beam fluorescence profile in 40 cm distance from the source. A simple MBD fit leads to dotted curve ($T = 467$K, $\hat{v} = 441$m/s). The fit quality is poor for low velocities. Therefore a modified velocity distribution is fitted to the data taking divergence due to the measured transversal velocity spread (Gaussian fit to absorption profile, $v_{trans} = 270$m/s) into account. This leads to $T_{mod} = 385$K and $\hat{v} = 400$m/s.

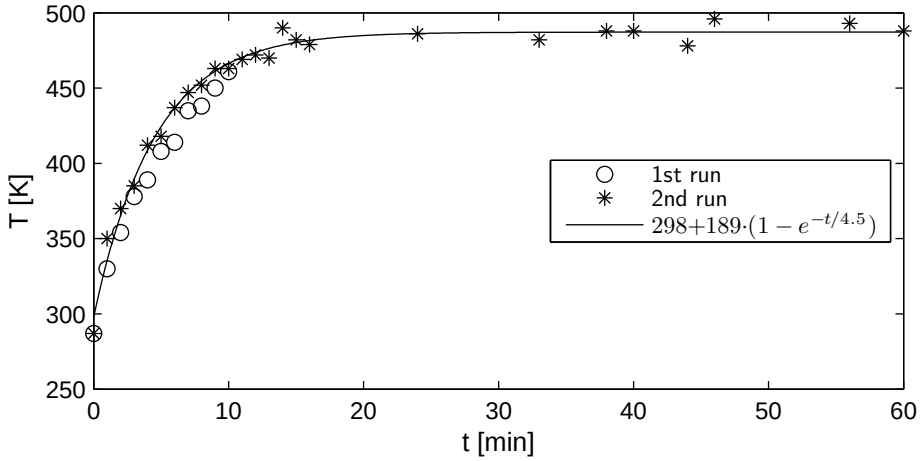

Figure 4.14.: Heating of the atomic beam source for high RF power from a multivibrator circuit. The time constant and the equilibrium temperature depend on the supplied power and the antenna setup, see text.

where θ is the angle between velocity vector and the main axis of the source tube. $\hat{v}$ is the most probable velocity of the corresponding MBD in the source. Nevertheless -regarding the fluorescence measurement- the initial MBD is reproduced: Fast atoms travel faster through the fluorescence volume, which leads to a suppression factor of v^{-1}.
The mean and most probable velocity as well as the corresponding temperature in the source can be obtained by fitting a modified MBD (modMBD) to the fluorescence signal. The need for modification arises when the transversal velocity comes into play. The transversal spreading of fast atoms along the atomic beam is less than for slow atoms. Hence, the fluorescence measurement actually detects less of the initially emitted slow atoms. Fig. 4.13 compares the fitted curves for a pure MBD and the modMBD. The modMBD clearly fits the data much better especially for low velocities where transversal spreading becomes important.
From the fluorescence measurement a most probable velocity of 400 m/s is derived which corresponds to 450 m/s mean velocity and a temperature $T = 385$ K. This, however, depends strongly on the operating conditions. Fig. 4.14 gives an example where an initially "cold" source warms up during operation with about 150 W RF power provided by a multivibrator circuit. The fitted line indicates that the characteristic time-scale for the heating process is $\tau \approx 4.5$ minutes. Equilibrium is reached after about 20 minutes.
Temperature is also an issue when difference source designs are considered. During operation of a 13.56 MHz discharge with a non-resonant antenna the source flange substantially heated up. This heating may be attributed to the poor conductivity of the source flange which leads to power dissipation as it has to serve as mirror monopole.
In addition, test runs with very small source diameters (as low as 0.2mm) resulted in deformation and degradation (and even melting) of the glass tube due to too high intensity or poor heat conductivity. Besides this, small tube diameters have the drawback of very steep pressure gradients which inhibit operation of turbomolecular pumps in recycling mode.
Fig. 4.15 presents the results for pressure dependence of the atom flow. Note that the set of experimental parameters is not the optimum, which explains the difference to the calculations in terms of maximum efficiency. The breakdown of the fitted curve can be

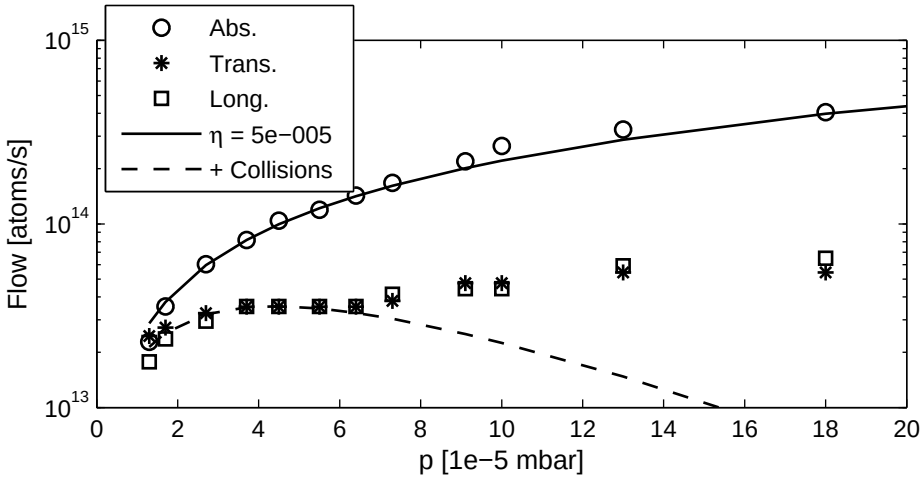

Figure 4.15.: An exemplary flow-pressure dataset. The source geometry is different from that in the previous calculation, hence the efficiency is rather low. The efficiencies from fluorescence measurements have been scaled to match the absorption data for low pressure. Dashed curve: fitted flow with constant $\eta = 5 \cdot 10^{-5}$ and losses due to metastable-ground-state collisions ($\sigma_{mg} = 300$ Å^2). For higher pressure the fit quality breaks down, see text.

explained by the following. The absorption measurement provides the excitation efficiency that is used for calculating the flow after the main chamber. But at about $6 \cdot 10^{-5}$ mbar the plasma begins to extend beyond the point of absorption measurement. Therefore, the efficiency increases strongly which leads to much higher metastable flow. From the difference between the solid line and the data the excitation efficiency is expected to have increased by one order of magnitude at a pressure of $1.8 \cdot 10^{-4}$ mbar.
In fig. 4.16 the saturation behavior predicted by the calculation is experimentally observed. However, for 144 MHz saturation is stronger than calculated: Here, application of more than 30 W RF power does not at all lead to substantial increase in metastable flow. The dataset for 13.56 MHz also shows saturation but it is much weaker in this case. The reason might be that, on the one hand, the tube is much narrower, thus excitation can mostly occur outside of it where the power threshold is higher. On the other hand, it could be related to the previously mentioned fact that the 13.56 MHz setup seems to dissipate more power in the vacuum parts. Therefore the actually available power might be less than what the RF generator claims.

4.3. Laser cooling basics

This section gives a brief overview of different parameters and formulae for laser cooling, which are relevant for the following calculations. Full derivations of these formulae can be found in a number of atom optics textbooks, e.g. [64] or [108].

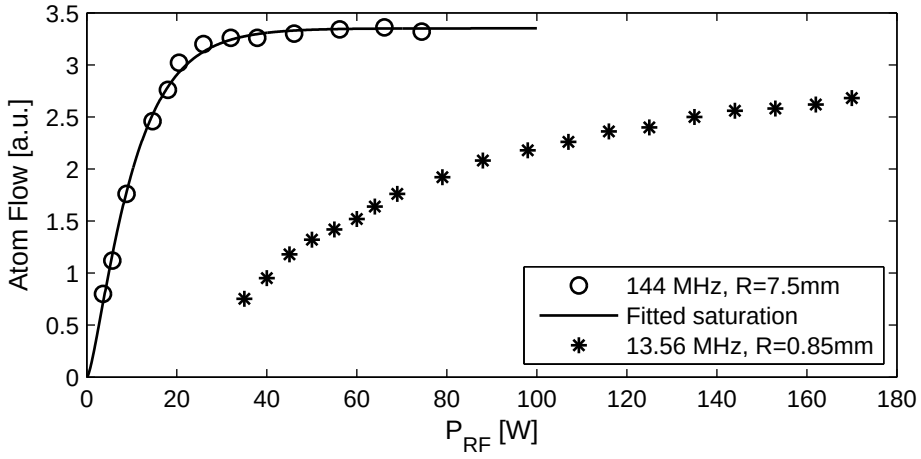

Figure 4.16.: The metastable production efficiency shows saturation for increasing RF power as qualitatively predicted by the calculation. The fit serves just as guide to the eye and is based on a best-guess curve.

4.3.1. Photon scattering rate

The concept of an isolated atom in free space has to be modified in order to understand the process of spontaneous emission from an excited atomic state. Basically, an excited atom can be seen as a pure state for the system "atom". Nevertheless, the system "atom + electromagnetic field" has different eigenstates: the electromagnetic field is also quantized and has a non-zero ground state. In this system, the excited atom is in a mixture of states and thus follows time evolution.
The mean lifetime τ of the excited state can be related to the linewidth Γ via $\tau = 1/\Gamma$. For spectroscopic purposes the spectroscopically observed linewidth γ is more convenient, $\gamma = \Gamma/(2\pi)$. From the derivation in [64] Γ is calculated as

$$\Gamma = \frac{\omega^3 |\mu_{eg}|^2}{3\pi\varepsilon_0 \hbar c^3} = \frac{16\pi^3 |\mu_{eg}|^2}{3\varepsilon_0 h \lambda^3}, \tag{4.20}$$

where μ_{eg} is the transition dipole moment defined accordingly

$$\mu_{eg} = \int \Psi_e^* \hat{\boldsymbol{\mu}} \Psi_g \mathrm{d}^3 r = \langle \Psi_e | \, \hat{\boldsymbol{\mu}} \, | \Psi_g \rangle \,. \tag{4.21}$$

The Ψ's denote ground and excited state and $\hat{\boldsymbol{\mu}}$ is the transition dipole moment operator. [109] gives a nice example of how the transition dipole moment is calculated and also illustrates polarization effects on the saturation intensity I_s. Laser cooling techniques, as presented in the following, mostly make use of $\sigma\pm$ polarized light. In this case of an ideal two-level system, the saturation intensity for ^{40}Ar computes to

$$I_s = \pi hc/(3\lambda^3 \tau) = \left(1.44 \mathrm{mW/cm^2}\right). \tag{4.22}$$

The on-resonance saturation parameter is defined as the ratio of incident intensity and saturation intensity, $s = I/I_s$. s_0 denotes the maximum saturation in e.g. the center of a Gaussian laser beam. In the following, the detuning Δ denotes the difference between the

frequency of the light the atoms "see" and the transition frequency ν_0. In particular, for off-resonant laser light with frequency ν_L the laser detuning is defined as

$$\delta_L = \nu_L - \nu_0, \quad \Delta_L = \omega_L - \omega_0. \tag{4.23}$$

A full treatment for a two-level atom (as can be found in the above-mentioned textbooks) results in an expression for the photon-scattering rate per atom, γ_p, dependent on laser intensity and detuning:

$$\gamma_p = \frac{\Gamma}{2} \cdot \frac{s}{1 + s + (2\Delta/\Gamma)^2}. \tag{4.24}$$

Power broadening as an effect of high intensity gives rise to the power broadened linewidth $\Gamma' = \Gamma \cdot \sqrt{1+s}$, see fig. 4.17. On the one hand, this can be beneficial under certain circumstances where e.g. all atoms should scatter as many photons as possible. But, on the other hand, controlled manipulation and efficient cooling of atoms becomes more complicated as the force on the atoms becomes less velocity sensitive, which will be illustrated in the paragraphs below.

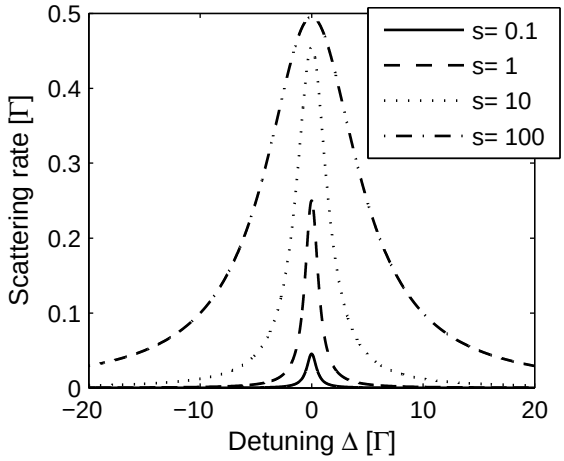

Figure 4.17.: The photon scattering rate as function of detuning for different intensities. The effect of increasing laser intensity manifests in an amplitude rise and substantial broadening of the curve.

4.3.2. Radiation pressure

Each of the photons absorbed by an atom transfers momentum to this atom. This momentum is given away again when the atom re-emits the photon. Thus, exposure to isotropic irradiation does not lead to a net momentum transfer. However, anisotropic irradiation from e.g. a laser beam has a very distinct effect. The atom absorbs only momentum from one direction whereas it emits isotropically. Combining eq. 4.24 with Newton's second law of motion and the momentum per photon $p_\gamma = \hbar k$ results in an expression[9] for this dissipative light force F_{dis}

$$F_{dis} = \gamma_p \hbar k = \frac{\Gamma}{2} \frac{s}{1 + s + (\frac{2\Delta}{\Gamma})^2} \hbar k. \tag{4.25}$$

[9] Congratulations, you just found the bonus footnote. Contact me for a free drink.

Atoms in motion experience an additional frequency shift by Doppler shifting the resonance frequency. This is calculated from the scalar product of the wave vector $\vec{k}$ and the velocity of the atom $\vec{v}$, $\Delta_D = -\vec{k}\vec{v}$. Therefore, for each atomic velocity there is a different detuning, $\Delta = \Delta_L + \Delta_D$. When $\vec{v}$ is anti-parallel to $\vec{k}$ then $\Delta_D > 0$. The atoms see light of a higher frequency, hence there is a certain velocity class in resonance with a red-detuned laser beam. The maximum deceleration is simply calculated by

$$a_{max} = \frac{F_{dis}(\Delta = 0)}{m} \approx \text{ several } 10^5 \text{m/s}^2 \text{ for typical parameters.} \tag{4.26}$$

4.3.3. Optical molasses

As a consequence, the resulting force on an atom in a system with two counter propagating beams, $\vec{k}_1$ and $\vec{k}_2 = -\vec{k}_1$, is

$$F = \frac{\Gamma\hbar\vec{k}_1}{2}\frac{s}{1+s+(\frac{2(\Delta_L-\vec{k}_1\vec{v})}{\Gamma})^2} + \frac{\Gamma\hbar\vec{k}_2}{2}\frac{s}{1+s+(\frac{2(\Delta_L-\vec{k}_2\vec{v})}{\Gamma})^2} \tag{4.27}$$

This expression can be expanded for small velocities, where $v_k = \vec{k}/k \cdot \vec{v}$:

$$F = 8\frac{\hbar k^2 \Delta_L}{\Gamma} \cdot \frac{s}{\left(1+s+(2\Delta_L/\Gamma)^2\right)^2} \cdot v_k \equiv -\beta v_k. \tag{4.28}$$

Provided that the detuning of the laser beams is negative, i.e. the light is red-detuned, β can be identified as a coefficient of damping. Hence, two counter propagating, red-detuned laser beams cause the atomic velocity along the axis of the beams to be viscously damped. In analogy to the well-known viscose liquid "molasses" this setup is named "Optical Molasses" (OM). Fig. 4.18 illustrates the effects of different detunings and/or varying intensity on the damping force.

4.4. Atomic beam collimation

4.4.1. Collimation techniques

In a long atomic beam apparatus atomic beam collimation becomes necessary, which is motivated in the following[10]. The MOT has a certain capture region, which is about $A_{MOT} = \pi r_{laser}^2$. Given the distance R between source and MOT, the solid angle observed by the MOT is $\Delta\Omega = A_{MOT}/R^2$. Under assumption of an effusive beam source, the fraction of detectable atoms is $\Delta\Omega/\pi$.[11]
In reality, things are even more complicated, because both longitudinal velocity $v_\parallel$ and transversal velocity $v_\perp$ are thermally distributed. Nevertheless, the detectable fraction is

[10] Note that this section serves as a overview, a more detailed discussion with helpful references can be found in e.g. [107].

[11] The full angle of the source is not 4π but π as only atoms that are actually emitted from the source into the hemisphere of the MOT have to be considered (factor 1/2) and $I(\theta) = I_0\cos\theta$ for an effusive source (another factor 1/2).

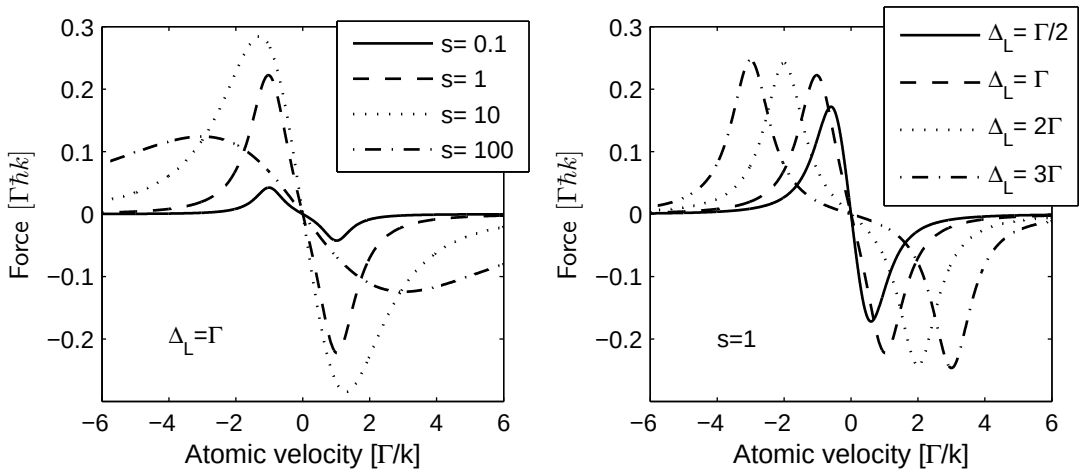

Figure 4.18.: Damping force in an optical molasses for different saturation s and different laser detuning Δ_L. Too low s leads to a rather small force on the atoms which limits the range of slowable atoms. Very large s also leads to smaller force as the spectral line is substantially broadened. For the detuning, things are similar: small Δ leads to a steep gradient of the force but of smaller amplitude. Large Δ however results in a less steep gradient. The velocity capture range of the OM is given by the region between the extrema of the curves. For the right-hand plots with $s = 1$ this corresponds to a range $[-\Delta_L/k.. + \Delta_L/k]$.

approximately $c^* \cdot r_{laser}^2/R^2$, thus inverse-quadratically decreases with distance from the source given a certain maximum r_{laser}. The proportionality factor c^* is calculated from the velocity distributions and increases for smaller transversal velocity width.
There are different techniques to reduce the transversal velocity spread of an atomic beam. The simplest one would be with a slit of diameter d in a certain distance l of the ideally point-like beam source. Only atoms with $v_\perp/v_\parallel \leq \frac{d}{2l}$ can pass the slit, thus the transversal velocity distribution is narrowed. This would, however, not yield a higher loading rate of the MOT as compared to a situation without slit, so it has gain 1.
Optical collimation can also be implemented and leads to large gains [110]. It has to be mentioned that the concept of a "gain" is not applied as easily as usually: a perfectly collimated beam would lead to gain 1 directly behind the source but to gain ∞ for infinitely large distance. "Gain" in the paragraphs below refers to the spatially dependent gain evaluated at the position of the MOT. In order to efficiently collimate atoms emerging from the source, the laser beams should be in resonance with large velocities close to the source. Close to the end of the collimation stage, they should be in resonance with atoms of zero transversal velocity. This can be achieved by e.g. one perpendicular laser beam of spatially varying detuning which is hard to produce. Alternatively, the angle between the atomic beam and a laser beam of fixed detuning has to be varied spatially.
Several realizations of this include curved mirrors, focused beams and tilted flat mirrors. Here, the latter is realized, as it has several advantages over the first two possibilities. Due to the large longitudinal velocity the collimation stage has to be long, which requires huge c.w. laser power when implemented with a focused beam. The mirror setups simply recycle the same beam again and again, as the absorption by the atoms is low. Nevertheless, the mirrors have to have a high reflection coating due to the large number of reflections. Flat mirrors are commonly used and thus are more or less readily available which is not

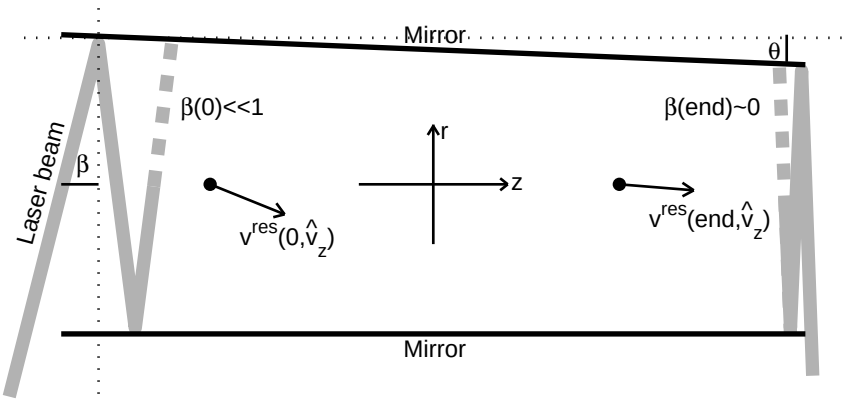

Figure 4.19.: Collimation of an atomic beam with tilted mirrors and laser light. Important parameters in the calculation are the incident laser angle β_0, the mirror angle θ, and the transversal and longitudinal velocity distributions. Note that each reflection of the laser beam at the tilted mirror changes the laser angle by 2θ.

necessarily the case for curved mirrors.
Collimation with tilted mirrors can be understood easily. The physical quantities used hereafter are defined in fig. 4.19. At each point along the longitudinal axis z there is one resonant transversal velocity $v_r^{res}(z, v_z)$ for each longitudinal velocity v_z. This can be calculated by setting the detuning zero:

$$0 \stackrel{!}{=} \Delta(z, v_z, v_r) = \Delta_L - \mathbf{k}\cdot\mathbf{v} = \Delta_L - kv_z\sin\beta(z) - kv_r\cos\beta(z)$$

$$\Rightarrow v_r^{res}(z, v_z) = \frac{\Delta_L - kv_z\sin\beta(z)}{k\cos\beta(z)} \stackrel{\beta\ll 1}{\Rightarrow} \frac{\Delta_L}{k} - v_z\beta(z) \tag{4.29}$$

The expression can be evaluated for typical parameters, $\beta(0) \approx 100$ mrad, $\beta(\text{end}) \approx 20$ mrad, $\Delta_L = 2\pi\cdot(+8\text{ MHz})$:

$$v_r^{res}(0, v_z) = 6.5\frac{\text{m}}{\text{s}} - \frac{v_z}{10} \quad \text{and} \quad v_r^{res}(\text{end}, v_z) = 6.5\frac{\text{m}}{\text{s}} - \frac{v_z}{50};$$

and for the most probable velocity $\widehat{v}_{MBD} \approx 430\frac{\text{m}}{\text{s}}$:

$$v_r^{res}(0, \widehat{v}_{MBD}) = -36.5\frac{\text{m}}{\text{s}} \quad \text{and} \quad v_r^{res}(\text{end}, \widehat{v}_{MBD}) = -2.1\frac{\text{m}}{\text{s}}.$$

4.4.2. Collimator design

Prior to the experimental realization, the optimum collimator parameters were determined by simulation. The details of this simulation and its results are described in [107]. It was found that -depending on the source geometry- collimation factors of up to 80 in the MOT are possible. As the atomic beam apparatus is actually longer than the simulated one, the maximum possible collimation factor should be around 120.
Parameters such as laser angle, mirror angle, laser detuning and beam saturation were optimized. The outcomes are as follows. In principle, the angles should be as small as possible, as this allows for a maximum number of reflections between the mirrors. This

is however restricted by the fact that the laser beams still have to be coupled into the collimator. Therefore the minimum laser angle is given by the spacing between the mirrors and the waist of the laser beam. The mirror spacing itself has to be as large as possible to reduce degradation of the coating from ion-impact.
Under these conditions, the optimum laser detuning should be around zero, tending to negative values. Still, the emission velocity distribution of the source can be different leading to modified results. In order to achieve the best results, the available laser power per beam has to exceed ≈ 100 mW.

4.4.3. Realization of the collimator

Motivated by the results from the simulation, the collimator consists of two pairs of 15 cm long, 4 cm wide mirrors with a spacing of 6 cm. These are mounted on adjustable custom mirror mounts. Ideally, a larger spacing would be beneficial, but this is the maximum possible given the geometrical constraints of the vacuum chamber.
A trade-off between setup stability and adjustability is reached by in-vacuum collimation of the laser beams. The light for each beam pair is guided into the chamber via a optical fiber feed-through. Then, elliptical beams with an aspect ratio of 1:3 are formed by cylindrical lenses of one inch diameter (f=50 mm, f=150 mm). A setup based on Thorlabs's opto-mechanical cage system serves for pre-adjustment of the collimator[12].
Each collimator axis can be optimized for optimum atom collimation by one motorized linear actuator (Newport NSA12V6) controlling θ. There is no need for further "knobs" as one mirror per pair is fixed to be parallel to the apparatus axis. The laser angles at the entrance of the collimator are likewise fixed and the beams enter nearly perpendicular to the atomic beam.
First measurements as presented in diploma thesis [107] and following publications [65, 67] show a collimation gain of only about 35, see also figs. 4.20 and 4.21. The transversal velocity spread is derived from the frequency calibrated fluorescence profiles by fitting Voigt curves to the data[13].
Despite principally good agreement with the simulation this is a striking difference. There are a number of possible reasons. Firstly, the simulation is done for only one radial axis (i.e 2D) and then extrapolated to 3D. Secondly, it assumes a point-like source which is not the case for a 11 mm source tube[14]. Thirdly, again related to the larger tube radius, the assumption for an effusive source does not hold here. This could also explain why the optimum detuning is found to be slightly blue (+8 MHz)[15].
Position sensitive fluorescence measurements carried out by translating the MOT chamber by about ± 40 mm yield the intensity profile of the atomic beam. The data shown in fig. 4.22 fits well to the calculated beam profile for the previously derived transversal velocity width and the source/pumping stage geometry ([65]).
The beam is clearly not perfectly collimated but already 36 % of the atoms can theoretically

[12] "pre-" as this cannot be adjusted under vacuum conditions.
[13] A Voigt curve is the convolution of a Gaussian with a Lorentz curve. The Lorentz curve describes the broadening to the spectral linewidth and the Gaussian the velocity distribution.
[14] The tube radius is similar to that of the following differential pumping stage. Hence it might well be that atoms from the off-center positions are also collimated but have a final radial position larger than the pumping stage. This will be investigated in the near future as it might yield higher ^{39}Ar count rate.
[15] This, however, can also be due to a not yet minimized mirror angle.

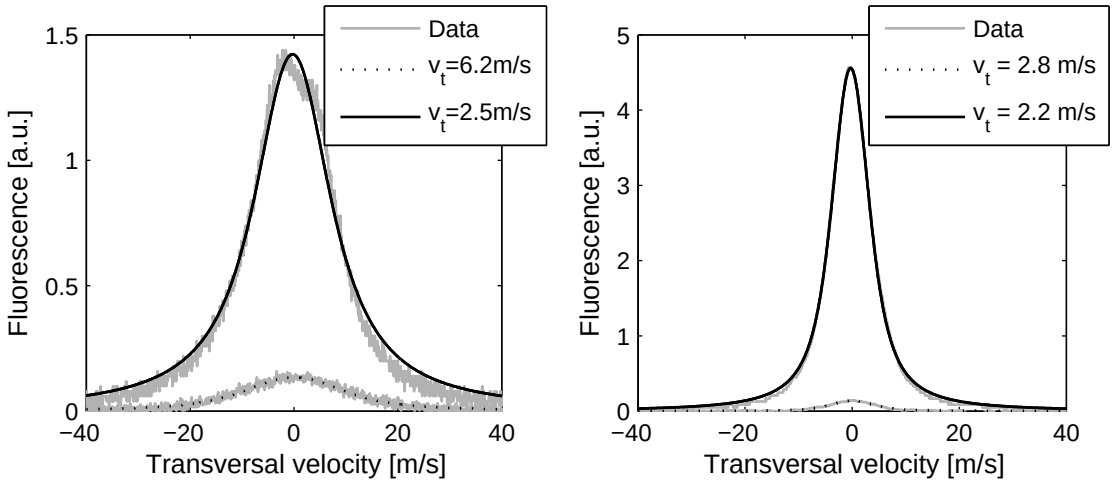

Figure 4.20.: Transversal fluorescence profiles for both the uncollimated and the collimated atomic beam at two different positions. The solid lines are fitted Voigt profiles for the collimated beam, the dotted for the uncollimated beam. Data is plotted in gray shade. Left-hand: fluorescence measured behind the differential pumping stage (after collimator). Right-hand: fluorescence at the position of the MOT. The larger enhancement with larger distance from the source is obvious. The small uncollimated width in the MOT chamber is due to geometrical collimation.

be captured. Further collimation is achieved by the magneto-optical lens, see next section.

4.5. Magneto-optical lens

4.5.1. Beam compression

Collimated atoms have a significantly reduced transversal velocity spread, thus the atomic beam diameter[16] increases slowly as it propagates through the apparatus. Still, it can be advantageous to have an even smaller beam, e.g. to implement steeper differential pumping stages. This can be achieved by setting up a compression stage downstream of the collimator.

There are different types of such compression stages all of which incorporate magnetic fields. The several types are distinguished by the geometry of the magnetic field, the number and geometry of the laser beams and their polarizations. Consequently, a variety of synonyms exist, among which “magneto-optical lens”, “atomic funnel” and “2D MOT” are most well-known.

Another benefit of such a compression stage is that it further reduces the transversal velocity by laser cooling. In that case, a convenient picture is to think of the collimator as being used for collecting as many atoms from the source as possible by transversal cooling.

[16]It might be defined in various ways, here it refers to the full width at half maximum (FWHM).

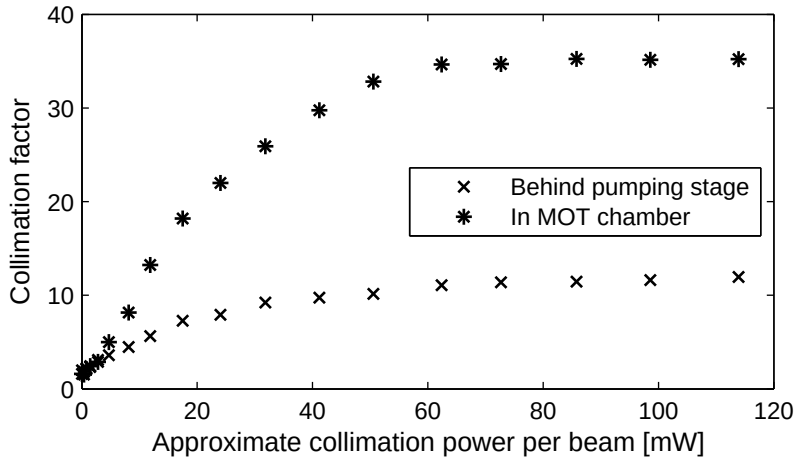

Figure 4.21.: Measured power dependence of the collimation for two different positions along the atomic beam. Both datasets show saturation for about 60 mW per beam which corresponds to $\approx$ 300 mW output power of the tapered amplifier. Much higher power would lead to less collimation due to even more power broadening.

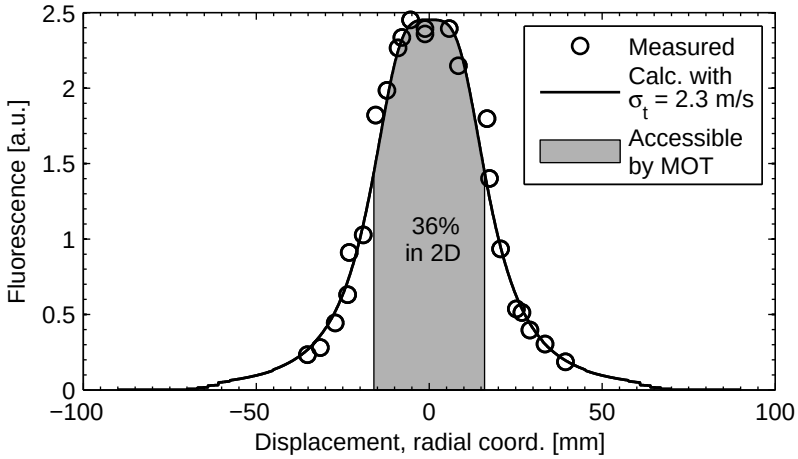

Figure 4.22.: Measured and calculated collimated beam profile at the position of the MOT. The MOT chamber is horizontally displaced by $\pm$40 mm while a fluorescence measurement setup is fixed to it. A calculated profile for $\sigma_v^{trans} = 2.3$ m/s well reproduces the measured radial profile. In order to obtain the fraction of atoms within the capture region of the MOT, the calculated profile is integrated in 2D ($\int\int ..r\mathrm{d}r\mathrm{d}\varphi$).

The subsequent 2D MOT then traps the atoms on the axis where transversal magnetic field is zero[17].

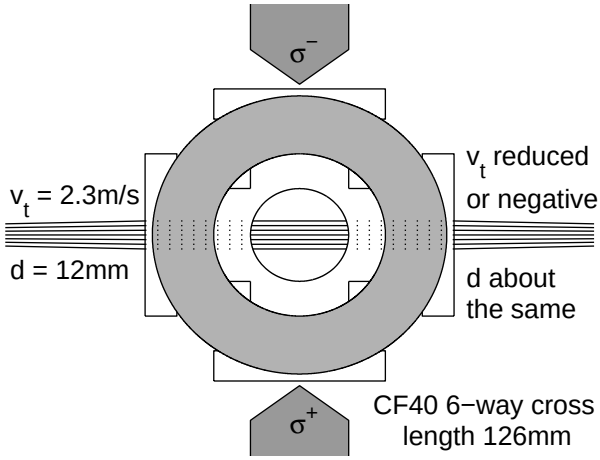

Figure 4.23.: Setup of the magneto-optical lens. A 6-way CF40-cross provides optical access for two pairs of trapping beams perpendicular to the atomic beam. Two flat coils produce the quadrupole field necessary for focusing atoms into the MOT.

4.5.2. Realization of the MOL

Implementation of the magneto-optical lens is done in a simple manner. Two flat coils with opposite direction of current produce a quadrupole field. Ideally, the axis connecting the coil centers should be aligned with the apparatus axis but mounting the pair under a 90° angle is much more compatible with the existing vacuum setup, see fig. 4.23. Due to this setup, there is one radial axis with twice the magnetic field gradient than the other one.
Fig. 4.24 shows the results for a simulation of the MOL. As the magnetic field gradients are ≈ 1.7 Gauss/cm and ≈ 0.85 Gauss/cm, results for 1.3 G/cm are given. Depending on their longitudinal velocity, atoms are focused into the MOT. Nevertheless, the divergence of the atomic beam is significantly reduced. The MOL is more efficient for ^{38}Ar than for ^{39}Ar due to the smaller number of magnetic sublevels and hence more efficient cooling.
The angles between the cooling beams and the atomic beam are adjusted such that the same light as for the MOT can be used. Separately tunable frequencies for the MOL would further complicate the optical setup as more AOMs would have to be set up. Given the specific magnetic field geometry, the difference in field gradients can be partially compensated by adjusting the laser power independently for each radial axis.
The effect of the MOL on the loading rate of the MOT can be seen in fig. 4.25. A one-dimensional MOL leads to a loading rate by a factor 1.8 higher than without MOL. For the two-dimensional MOL a gain of $1.8^2 = 3.24$ is predicted as both axes are independent.

[17] Depending on the type of coil setup there might be several such axes. A quadrupole field produced by a pair of coils in anti-Helmholtz configuration offers the axis between the centers of both coils and the plane between the two coils. For very fast beams the axis is given by the longitudinal velocity but longitudinally slow beams may change direction, depending on the alignment of the laser beams, see [111] for an example.

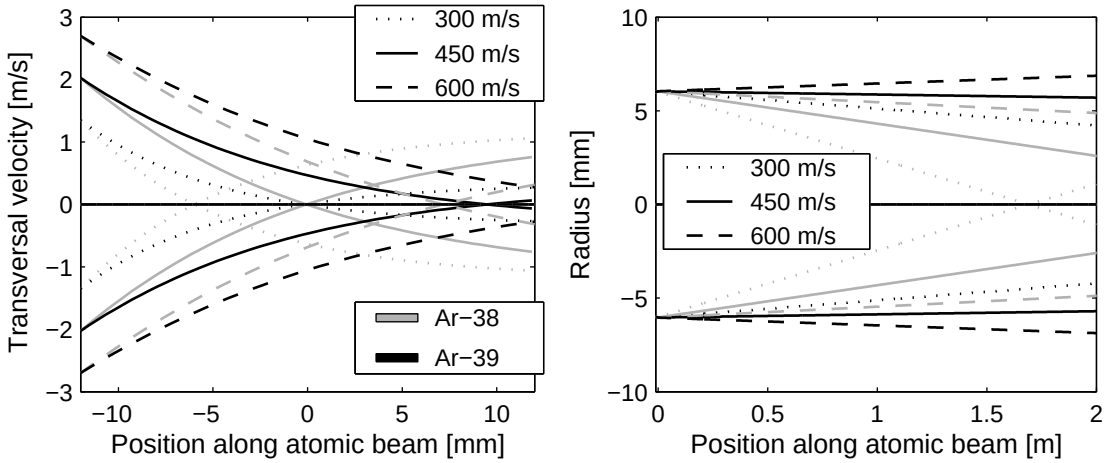

Figure 4.24.: Calculated trajectories for ^{38}Ar and ^{39}Ar in a two-dimensional magneto-optical trap. The parameters are about the same as in the experiment: magnetic field gradient 1.3 G/cm, $\delta = -6$ MHz, $s = 5$. The term "magneto-optical lens" is well justified for ^{38}Ar whereas it is less obvious for ^{39}Ar due to smaller effective detuning between the opposing trap beams.

This agrees well with the observed results showing a gain of 3.1 which deviates only by 5% from the expected value.
Thus, for the final design with such a two-stage collimation, it is safe to assume that more than 90% of the metastable atoms passing the pumping stage at least reach the MOT chamber[18]. But -as illustrated in the following section- the Zeeman slower again reduces this efficiency.

4.6. Longitudinal slowing

The collimated and compressed atomic beam still has a high mean longitudinal velocity. Integral detectors such as Faraday cups or multichannel plates that measure the absolute flux are not influenced by the longitudinal velocity distribution but the MOT is sensitive to it due to the limited capture velocity, see sec. 4.7. It only detects atoms from a range of velocity close to zero, typically up to a few tens of meters per second. Thus, the velocity distribution along the direction of flight also has to be both narrowed and shifted to smaller values. The methods explained below make use of electric fields, laser beams, or combinations of the latter with magnetic fields. This experimental realization of ^{39}Ar-ATTA features a so-called Zeeman slower but for a first MOT a chirped slower was used. To provide a more complete picture, various other slowing techniques are explained as well.
Whenever a laser beam is used to longitudinally slow atoms down, it has to be kept in mind that the momentum transfer by the photons lead to a three-dimensional random walk in momentum space. Although scattering N photons with a counter propagating

[18]Simply by multipliying the MOL gain with the fraction of the atomic beam that can be trapped.

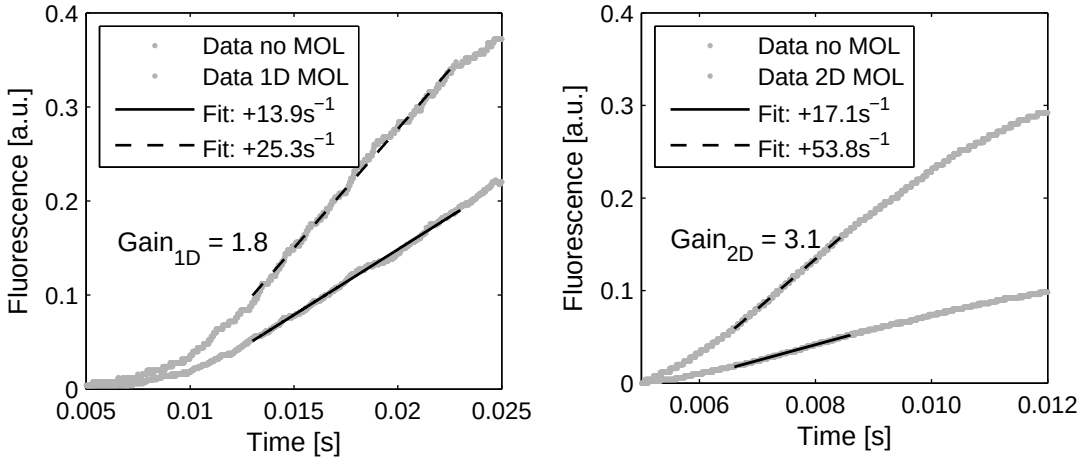

Figure 4.25.: Loading rate of the MOT with and without magneto-optical lens. Left-hand: one-dimensional MOL, right-hand: two-dimensional MOL. As to be expected the 2D-gain is approximately the square of the 1D-gain (5% deviation).

laser beam reduces the mean longitudinal velocity by

$$\Delta v_{\parallel} = N \cdot \frac{\hbar k}{m}, \tag{4.30}$$

it leads to transversal heating. The atoms perform a 3D random walk with N steps, consequently the transversal velocity spread broadens by

$$\Delta v_{\perp} = \sqrt{\frac{N}{3}} \cdot \frac{\hbar k}{m} = \sqrt{\frac{1}{3} \cdot \frac{\hbar k}{m} \cdot \Delta v_{\parallel}}. \tag{4.31}$$

4.6.1. Methods

Stark Slower

The Stark slower as explained in [112] uses the DC Stark effect. This effect describes the frequency shift of atomic levels in an electric field. The detuning depends quadratically on the electric field strength E, $\Delta_S = \frac{\alpha}{2}E^2$. The proportionality factor α depends on the scalar and tensor polarizabilities of the levels involved and their angular momentum quantum numbers, J and m_J. The limiting parameter for a Stark slower are the high electric fields needed (typically tens of kV/mm). In combination with the atomic beam diameter and its divergence this rapidly leads to voltages of about 1 MV which cannot be easily handled.

Slowing with a broadband laser

An atomic beam can also be slowed down by a broadband laser beam [113]. This is resonant with a large velocity range but has a much lower spectral power density. For a given broad frequency range $\Delta\omega$ the same deceleration (as with a narrow band laser) can be

achieved by $P_{laser}^{broad} \approx P_{laser}^{narrow} \cdot \Delta\omega/\Gamma'_{narrow}$. Each velocity class is resonantly slowed down to the same final velocity. The main disadvantage besides the large laser power necessary is that the different velocity classes reach the final velocity at different positions. Thus, they might not be detected due to transversal movement. Another disadvantage when dealing with multi-level atoms is undesired optical pumping because of the multitude of frequencies offered by the laser.

Chirped slower

Keeping in mind what is illustrated in section 4.3, a simple scheme for reduced longitudinal velocity exploits the Doppler shift. A red-detuned laser beam (detuning $\Delta_L < 0$) propagates towards the atomic beam and decelerates atoms close to $v_{res} = |\Delta_L|/k$. The addressed range of velocities depends on the power-broadened linewidth, $\Delta v = \Gamma'/k$.
A chirp of the laser frequency causes v_{res} to vary accordingly. Given that the chirp is linear and that the atoms can follow it, i.e.

$$\frac{1}{k} \cdot \frac{\mathrm{d}\omega}{\mathrm{d}t} \overset{4.26}{\leq} a_{max}, \tag{4.32}$$

part of the atoms can be slowed down to have a velocity in the capture range at the position of the MOT, [114],[115],[116],[117]. However, most of the atoms still remain not slowed down at all or are slowed down to low speed before reaching the MOT, thus they are lost due to the residual transversal velocity or gravitational acceleration.
A simple approach serves for further clarification of this effect. The equations of motions are solved for different release times of atoms from the source. Basically, the following equations are numerically integrated, and the result is shown in fig. 4.26

$$\dot{v} = \frac{\Gamma\hbar k}{2m} \cdot \frac{s}{1 + s + \left(\frac{2(\Delta_L(t) + k \cdot v)}{\Gamma}\right)^2} \quad \text{and} \quad \dot{z} = v. \tag{4.33}$$

Zeeman Slower

Just like the above-mentioned techniques, Zeeman slowing uses a laser beam counter propagating the atomic beam. It is a magneto-optical technique that uses a (off-)resonant light in combination with a spatially varying magnetic field. Again, the idea is that atoms of an initially higher velocity are slowed down by resonant scattering. But in contrast to the chirped-slower it is not the laser frequency that compensates for the temporal change in Doppler shift but a magnetic field shifts the atomic resonance. It is shifted such that at each position another velocity is resonant. Assuming a constant deceleration a, an initial velocity v_{up} and a final velocity v_{lo} leads to the solution of the trajectory in phase space

$$v(z) = \sqrt{v_{up}^2 - 2az}\ , \quad z \leq z_{max} = \frac{v_{up}^2 - v_{lo}^2}{2a} \tag{4.34}$$

The geometry of the magnetic field can be calculated similar to sec. 4.4.1. Atoms of a certain velocity v along the beam axis see the Doppler-shifted frequency, $\omega_{obs} = \omega_L +$

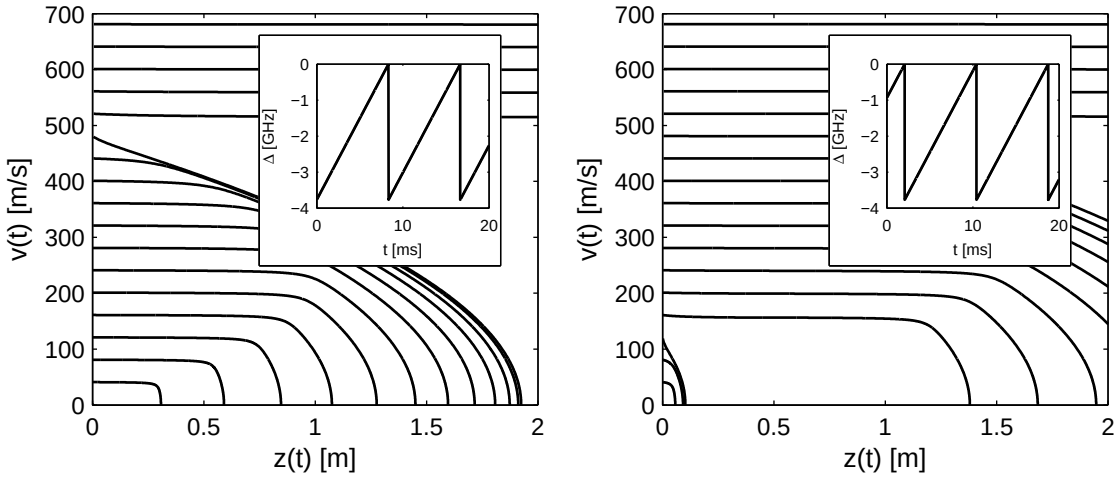

Figure 4.26.: Chirped slower velocity trajectories for two different release times of the atoms from the source. Note that the release time Δt is defined via the phase of the frequency sweep whereas -for convenience- each calculation starts at t=0. Left-hand: $\Delta t = 0$; right-hand: $\Delta t = 3/4 \cdot T$. For this calculation the parameters are $\Delta = -2\pi \cdot 600$ MHz..$2\pi \cdot 0$ MHz, $f_{chirp} = 120$ Hz and $s = 10$. In reality the chirp would only go to about -30 MHz, where the atoms are slow enough to be captured and the displacement of the MOT by radiation pressure is much less. But the general pattern remains similar, for each release time atoms of different initial velocity or even no atoms at all are slowed down to have velocities in the capture range at the position of the MOT.

$k \cdot v(z)$. In order to resonantly scatter light this has to equal the magnetically shifted atomic transition frequency, $\omega_{shift} = \omega_0 + \frac{\mu'}{\hbar} \cdot B(z)$, where μ' denotes the effective magnetic moment of the transition,

$$\mu' = (m_e g_e - m_g g_g)\mu_B, \tag{4.35}$$

where $m_{g,e}$ is the magnetic quantum number and $g_{g,e}$ the Landé g-factor of the ground or excited state, respectively. The Landé factors are calculated according to eq. C.11-C.15. With the laser detuning defined in eq. 4.23 it follows that

$$\Delta_L + k \cdot v(z) \stackrel{!}{=} \frac{\mu'}{\hbar} \cdot B(z) \quad \text{for resonant scattering.} \tag{4.36}$$

Plugging in the velocity trajectory as in eq. 4.34, the above is equivalent to

$$B(z) = \frac{\hbar}{\mu'} \cdot \left(\Delta_L + k \cdot \sqrt{v_{up}^2 - 2az}\right) \quad , \quad z \leq z_{max} = \frac{v_{up}^2 - v_{lo}^2}{2a} \tag{4.37}$$

So far, Zeeman slowing under ideal conditions has been discussed, but any realization deviates from those due to imperfections e.g. in the coils. Therefore, an additional criterion has to be introduced, which relates the slope of the magnetic field to the maximum possible deceleration. The spatial derivative can be written as

$$\frac{\mathrm{d}B}{\mathrm{d}z} \stackrel{4.37}{=} \frac{\hbar k}{\mu'} \cdot \frac{\mathrm{d}v}{\mathrm{d}z} = \frac{\hbar k}{\mu'} \cdot \frac{\mathrm{d}v}{\mathrm{d}t} \cdot \frac{\mathrm{d}t}{\mathrm{d}z} = \frac{\hbar k}{\mu'} \cdot a \cdot \frac{1}{v}.$$

It is found, that for each point along the axis of propagation the following has to be fulfilled:

$$\left|\frac{\mathrm{d}B}{\mathrm{d}z}\right| \leq \frac{\hbar k}{\mu'} \cdot a_{max} \cdot \frac{1}{v(z)}. \tag{4.38}$$

In order to account for this, a sound assumption for a in eqs. 4.34, 4.37, and in the numerical optimization is

$$a \leq \xi \cdot a_{max}, \tag{4.39}$$

with a typical fudge factor $0.4 \leq \xi \leq 0.6$ that accounts for imperfections in the magnetic field and the non-uniform laser beam.
Without loss of generality B is positive in the following discussion and the quantization axis is parallel to the magnetic field. The effective magnetic moment μ' is accordingly positive (negative) for σ^+ (σ^-) polarized light, which leads to different solutions for $B(z)$. These various types of magnetic field geometry are displayed in fig. 4.27 for further illustration.
a.) Decreasing field slower, first realization [118], see also or [119]:

$$\begin{aligned} B(z_{max}) \approx 0 \Rightarrow \Delta_L &= -k \cdot v_{lo} \\ \overset{B(0)\geq 0}{\Rightarrow} \mu' > 0 &\Rightarrow \text{use of } \sigma^+ \text{ light} \\ B(z) = \frac{\hbar k}{\mu'} &\left(\sqrt{v_{up}^2 - 2az} - v_{lo}\right) \ , \quad \mu' > 0 \end{aligned} \tag{4.40}$$

b.) Increasing field slower, see also [120] or [119]:

$$\begin{aligned} B(0) = 0 \Rightarrow \Delta_L &= -k \cdot v_{up} \\ \overset{B(z)\geq 0}{\Rightarrow} \mu' < 0 &\Rightarrow \text{use of } \sigma^- \text{ light} \\ B(z) = \frac{\hbar k}{\mu'} &\left(\sqrt{v_{up}^2 - 2az} - v_{up}\right) \ , \quad \mu' < 0 \end{aligned} \tag{4.41}$$

c.) Spin-flip slower: In the case of the spin flip slower the condition of $B > 0$ becomes problematic and requires further illustration. The magnetic field reverses its sign and thus the quantization axis turns around. Accordingly, the polarization of the light shifts from σ^+ to σ^-. The detuning is set such that the light is resonant with the atoms in the intermediate region. Depending on the type of the transition used this region of zero magnetic field has to be large as ideally all atoms have to be pumped from one stretched state to the opposite one. The magnetic field profile of the spin-flip slower can be described by a combination of one of the above curves with a constant offset:

$$B(z) = \frac{\hbar k}{\mu'} \left(\sqrt{v_{up}^2 - 2az} - v_{lo}\right) - B_{offset} \ , \quad \mu' > 0 \tag{4.42}$$

Choice of the appropriate slowing technique

The previous section illustrates some of the various mechanisms to slow an atomic beam down. Given the need for a high flux apparatus and the limited capture range of the magneto-optical trap, the Zeeman slower is the right technique to be implemented. However, the choice among the different Zeeman slower types is not that obvious. Therefore, the main features of each of the three kinds are discussed in the below.

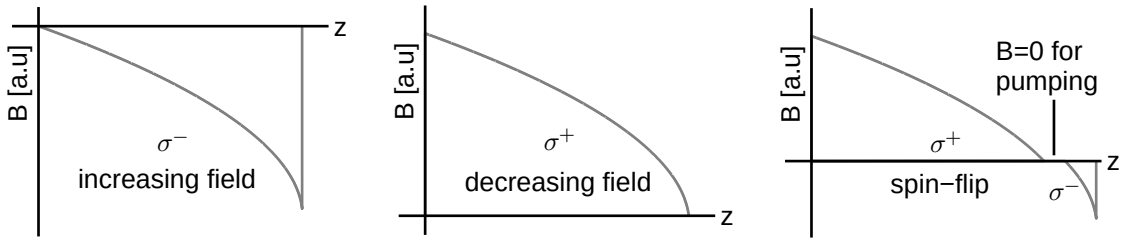

Figure 4.27.: The different types of Zeeman slower magnetic field configuration. Theoretically, there are two more configurations, namely increasing field slower and the decreasing field slower with an offset such that the profiles are shifted to higher absolute values. Each of the three configuration shown has certain benefits and drawbacks, yet the realization of an increasing field slower is the most advantageous in the context of this experiment.

a.) The main advantage of the **decreasing field slower** (sometimes also called "σ^+-slower") is that is has a low field at its exit. That means that experiments close to it are not disturbed by the slowly decaying field of the coil. However, this can also cause problems, as the laser beam remains resonant with the atoms when $B = 0$, they are further slowed down. Thus, extraction of atoms with one (more or less) clearly defined final velocity is complicated for the case of a σ^+-slower.
Further problems may arise as the laser is close to the atomic resonance and thus exerts influence on atoms at rest. In a magneto-optical trap the additional light pressure can be compensated by the trapping beams but for e.g. a purely magnetic trap the atoms might just be pushed out of the trap.
Another more practical drawback is the large power consumption of the decreasing field slower. For a realization with coils it is approximately proportional to the integral of the square of the current running through the coil. The current itself is -again approximately- proportional to the B-field. Thus the power

$$P \propto \int |B(z)|^2 \mathrm{d}z \tag{4.43}$$

is dissipated as heat and has to be transported away from the experiment. From fig. 4.27 it is obvious that the power is the highest for the σ^+-slower.
b.) The **increasing field slower** (also referred to as "σ^--slower"), in turn, has its maximum at the end and the residual field strongly influences the experiment if no additional measures are taken. A simple way to deal with this is the implementation of compensation coils.
Besides this obvious disadvantage, the σ^--slower offers better extraction of atoms as the field decreases steeply at the end and the light is no longer resonant with the atomic beam or atoms at rest (especially not with the MOT). The power consumption is moderate and it can be realized with a single solenoid coil as easily as the decreasing field slower.
c.) A **spin-flip slower** combines most of the benefits of the latter two. The light is not resonant in the experiment region and extraction of atoms works well. The residual field is typically much lower than with the σ^--slower and it can be minimized for power consumption. Depending on the parameters used, the power consumption can be as low as just one tenth of the consumption of the corresponding σ^+-slower.
Nevertheless, the major drawback is the fact that the atoms have to be pumped from one stretched state to the opposite one. Thus, the intermediate region has to have $B \approx 0$. In

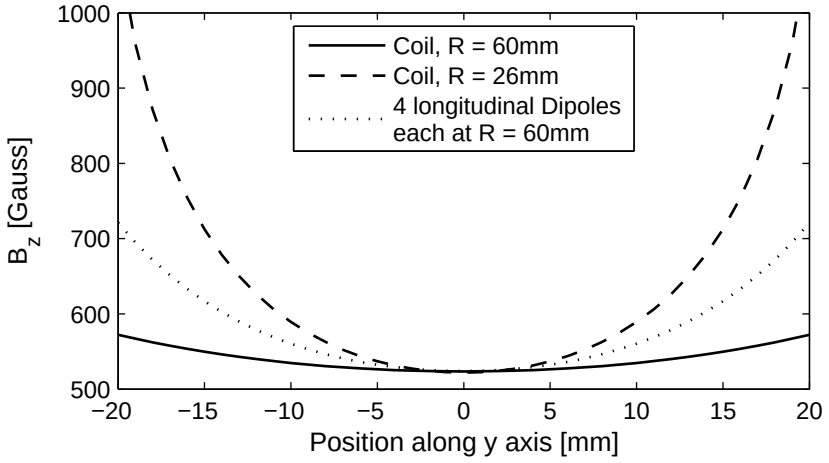

Figure 4.28.: Comparison of the transversal magnetic field variation for different Zeeman slower realizations. Large coil diameter results in a more homogeneous field than a small coil or a setup with dipole magnets placed on the same radius. Field homogeneity is particularly important for the final velocity of atoms emerging the slower. Higher magnetic fields lead to lower final velocity and more loss due to the transversal velocity.

this experiment, optical pumping gets further complicated by the large number of magnetic substates in ^{39}Ar. A recent publication by the competing group at ANL identifies undesired optical pumping in their spin-flip slower as one of the possible processes which suppress ^{39}Ar detection by a factor of 30 [14].
These arguments motivate that implementing a σ^--slower seems to be the most appropriate in the present case. The implementation itself can be done by either using solenoid coils or permanent magnets [121] (this is a realization of a transverse slower, i.e. a "π-slower"). Permanent magnets only have to be magnetized once and do not further consume power. The adjustment, however, is not as easy as with a solenoid coil, where the winding setup can be calculated before-hand and the current can be increased or decreased. [122] also states that the laser power needed to provide saturation with such a π-slower is significantly higher. This is most probably simply due the higher saturation intensity, as more levels are involved.
The large atomic beam diameter in the present case would also require a large radial distance of the magnets to provide a sufficiently homogeneous field, as the radial variation is stronger than for solenoid coils. This would again lead to a slow decline of the field and is thus not favorable. Fig. 4.28 shows a comparison between a dipole magnet setup and two coils of different radii, where the advantages of a coil setup with large diameter become apparent. After all, the strongest argument for a realization with coils is clearly the fact that the optimization routine is much easier as only the laser detuning has to be varied versus the current supplied.

4.6.2. Characteristics of the implemented Zeeman slower

Design

As explained in the preceding sections calculations of a Zeeman slower field typically use a "safety" parameter for the average deceleration, here $\xi = 0.5$. There are certain boundary conditions that the Zeeman slower has to meet, thus its maximum length is limited to 2 m in the present case.
Still, this is only an upper limit and the length has to be optimized for maximum flux[19]. At the time of the design the magneto-optical lens was not yet implemented, therefore the residual transversal velocity for this optimization was significantly larger than in the final setup (see caption fig. 4.29).
The results suggest that the 1.8 m long slower only allows for trapping of about 9% of the atoms when no additional measures are taken. With a higher final longitudinal velocity (which necessitates either a second frequency in the slowing beam or toggling between different MOT frequencies, see below) this can be increased to $\approx 33\%$.
Reduction of the transverse velocity with a magneto-optical lens gives another factor 2 increase, so that trapping of $\approx 68\%$ of the atoms seems possible. The difference to the previously derived MOL gain might be due to a different final velocity. For a modified initial velocity distribution via liquid nitrogen cooling of the source ($T_{mod} \approx 200$ K) 91% efficiency is predicted.

Given the optimum slower length, fig. 4.30 compares the realization of the magnetic field with the ideal shape for optimum slowing. The real field has pronounced wiggles which come from the discrete number of coil layers. As discussed above, it declines much slower than it ideally should. Therefore, a compensation coil with opposite field direction is implemented. This does not only lead to a faster decline but mainly serves for reducing the magnetic field at the designated position of the MOT.
Fig. 4.31 illustrates the setup and position of the coils relevant for the MOT. However, the coil pair for magneto-optical compression is not depicted as it is rather uncritical.
The wiggles mentioned above may lead to a partially too steep magnetic field gradient. This could cause atoms to leave resonance, which would result in a reduced efficiency, [66]. Nevertheless, the atoms can be brought back into resonance by increasing the laser power, thereby power broadening the resonance, see fig. 4.32.
The field shape of the designed coil is further tested for function by calculating the trajectories of different initial velocities, fig. 4.33. This has also be done by means of Monte-Carlo simulation and can be found in [66]. However, as the results do not deviate significantly, a simple step-wise calculation is sufficient here.

[19] The optimization procedure works as follows. Each slower length corresponds to an accessible velocity range and thus a maximum possible fraction of atoms slowed. For each velocity v from this range the transverse velocity spread $\sigma_r(v, z)$ is calculated. The initial spread is given by the collimator and broadening starts as soon as the velocity class comes into resonance. The additional velocity arises from eq. 4.31. With the help of $\sigma_r(v, z)$ the radius of the beam at the position of the MOT can be obtained for each v. This, in turn, allows for an approximate measure for the detectable fraction of atoms $\eta(v)$ via the error function. Convolution of $\eta(v)$ and probability distribution $p(v, T)$ leads to the quantity of interest, $\eta(l, T)$.

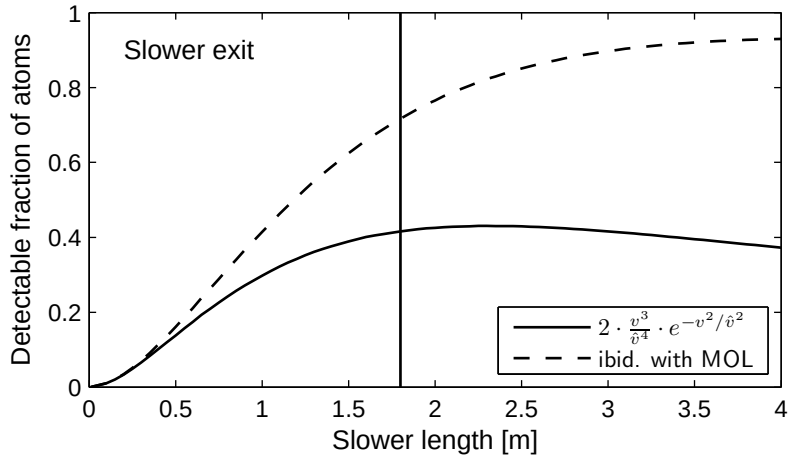

(a)

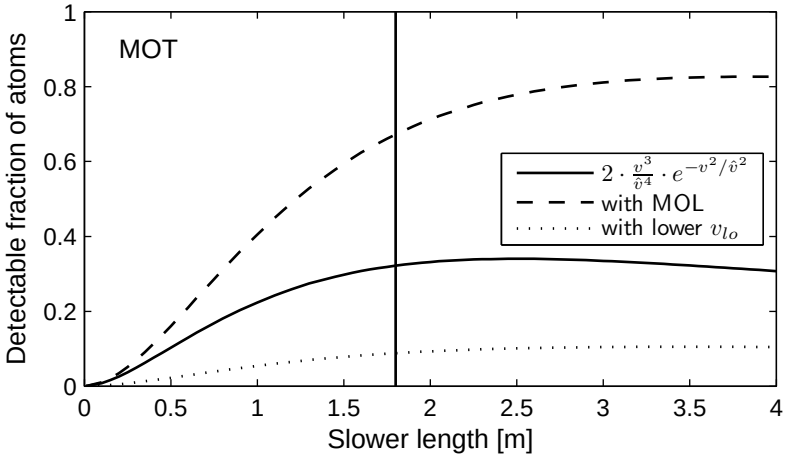

(b)

Figure 4.29.: Fraction of atoms detectable as function of slower length. The calculation uses the following parameters: $m = 39 \cdot m_u$, $\hat{v} = 405$ m/s ($T = 385$K), $\sigma_{trans} = 2.6$ m/s, $\xi = 0.5$, $r_{MOT} = 15$ mm. Transversal heating by scattering is taken into account. A vertical solid line indicates the actual length which is a compromise for several velocity profiles.
(a) directly behind the slower. The solid line assumes the previously derived velocity distribution (one order higher in v than a MBD, the flux out of the source more likely follows this behavior, see sec. 4.2). The dashed curve assumes the modified velocity distribution and a much narrower initial velocity spread as realized with the MOL.
(b) in the MOT. The solid line and the dashed line use the same parameters as above. The dotted line is a calculation for a much lower final velocity, $v_{lo} = 5$ m/s. The loss due to the Zeeman slower is strongly governed by the final divergence and the distance to the MOT. Using a two-frequency slower solves this problem.

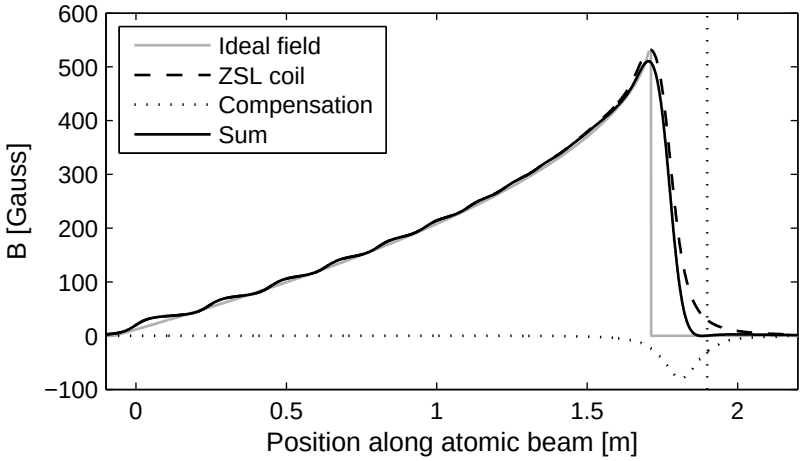

Figure 4.30.: Magnetic field of the Zeeman slower. The gray line indicates the ideal field as calculated from eq. 4.41. The real field (dashed) declines slowly wherefore a compensation coil is implemented (dotted line). It is optimized given the experiment's geometrical and mechanical restrictions. The resulting field is represented by the solid line and the position of the MOT is indicated by a vertical dotted line.

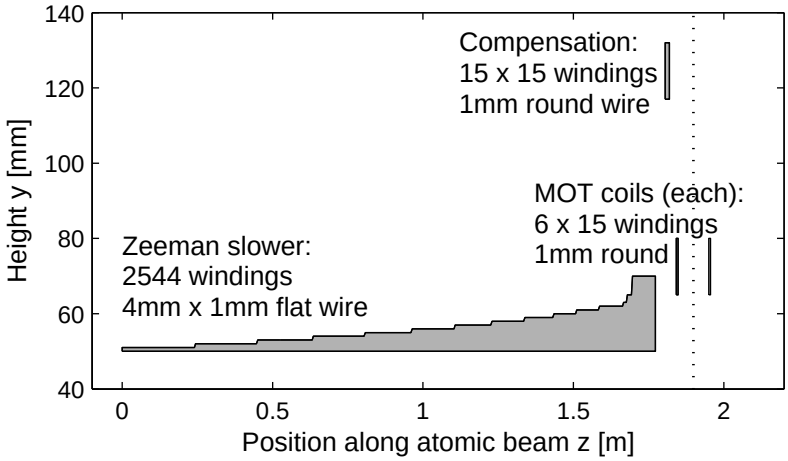

Figure 4.31.: Setup and position of coils relevant for slowing down and trapping of atoms. The figure shows a cut in the y-z-plane for positive values of y. Zeeman slower coil and compensation coil are symmetric around z whereas the MOT coils are symmetric to the x-z-plane (i.e. the optical table). The second MOT coil can be found at $y = -[65..80]$ mm accordingly.

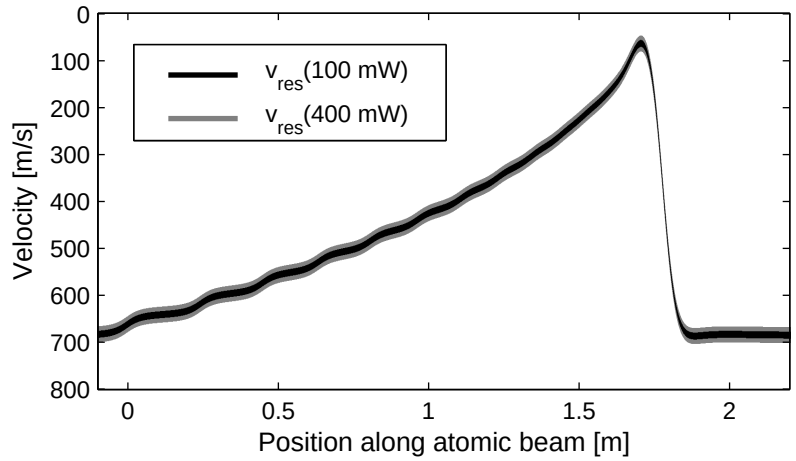

Figure 4.32.: Position dependent resonant velocities for two different values of laser power. The black-(gray-) shaded areas indicate the atoms which experience more than half of the maximum possible deceleration for $P_{laser} = 100$ mW ($P_{laser} = 400$ mW). Consequently, for these atoms the scattering rate γ_p is larger than $\Gamma/4$. This reflects the fudge factor ξ being set to $\xi = 0.5$.

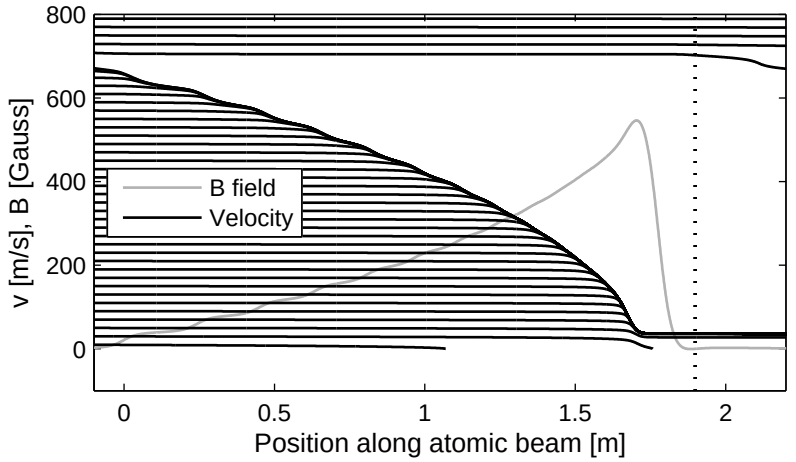

Figure 4.33.: Velocity trajectories for the realized Zeeman slower. The parameters for calculation are: $I_{ZSL} = 13.2$ A, $I_{comp} \approx 5$ A, $P_{laser} = 70$ mW, $\Delta = -844$ MHz. The final velocity of the slow atoms of $v_{lo} \approx 36$ m/s is beyond the capture range of the MOT which is why a second Zeeman slower frequency is implemented, $\Delta_{booster} \approx -28$ MHz.

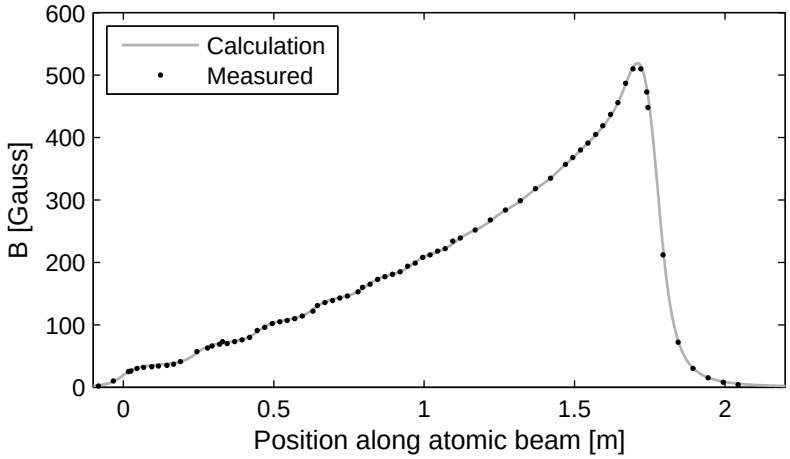

Figure 4.34.: Magnetic field of the Zeeman slower for $I_{ZSL} = 12$ A as measured by a Hall probe. The agreement with the calculated field is very good. Note that the calculated field is rescaled as compared to previous illustrations to account for the different current.

Realization

The Zeeman slower coil is wound onto a brass tube of 100 mm diameter. The tube itself has longitudinal grooves which house copper pipes (dia. 6 mm) for water cooling. Fig. 4.31 shows the winding plan of the slower according to which $\approx$ 2500 windings of flat wire (4 mm $\times$ 1 mm) are coiled layer-wise. Each layer is connected both mechanically and thermally to the preceding with Stycast® thermally conductive resin. In steady state, e.g. while $\approx$ 700 W are dissipated, the slower equilibrates a temperature of about 35°C. A comparison between the calculated and the measured field of the finished coil can be seen in fig. 4.34. The compensation coil is implemented by 225 windings on an aluminum ring with one copper pipe glued to it. Round wire is used and the windings are placed in a 15 mm $\times$ 15 mm groove. Again, the copper pipe is necessary for cooling, as the power dissipation is $\approx$ 60W.
As already mentioned above, the Zeeman slower beam features two frequencies for cooling. This can be motivated by a closer look at the characteristics of the atomic beam. It is already collimated by the differential pumping stages and the transversal velocity spread is further reduced by the collimator and the magneto-optical lens. Hence, the velocity capture range in directions perpendicular to the beam does not need to be larger than a couple of m/s. In direction along the beam the capture range has to be larger, as the transfer efficiency from Zeeman slower to MOT is governed by the final velocity of the slower.
Therefore, the additional near-resonant ($\delta \approx -28$ MHz) frequency, the so-called "booster", slows the atoms further down on the slope of the MOT field. Usually, the MOT light would be further red-detuned to allow for this longitudinal slowing with the MOT beams. However, the scattering rate has to be high for successful detection of single-atoms, thus the MOT beam detuning is set to $\Delta_{MOT} \approx -4$ MHz.
Nevertheless, the function of the slower can be tested with light of only one frequency and fluorescence measurement in the MOT chamber. Extraction of the overall efficiency is complicated, as the MOT beams can trap more atoms than the smaller fluorescence beam

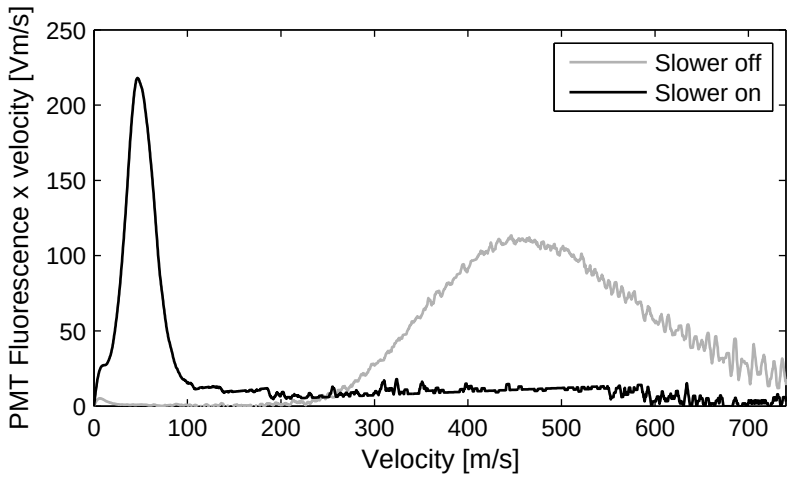

Figure 4.35.: Fluorescence measurement of the initial and slowed down velocity distribution at the position of the MOT. Note that the fluorescence measurement only detects density which is why the data is multiplied by v to get the flux. This linear scaling results in a much noisier signal for high velocity. The final velocity can be adjusted by either the field strength or the slower detuning. The integral over the slow atom peak corresponds to 29 % of the unslowed profile.

can access. Anyhow, the fraction of atoms that are actually manipulated by the slower can be derived from fig. 4.35 to 86 % of the initial flux. The better the initial collimation and the larger the MOT beams, the closer the slower efficiency will be to this upper bound. In this example without magneto-optical lens it is only 29 % which coincides with the prediction in fig. 4.29.

4.7. Magneto-optical trap

4.7.1. From optical molasses to magneto-optical trap

As soon as magnetic fields come into play the magnetic substructure of the atoms has to be taken into consideration. Each of the magnetic sublevels of the atomic states corresponds to an angular momentum state. These angular momentum states have magnetic dipole momenta which couple to external magnetic fields and lead to a shift in energy (generally referred to as "Zeeman effect"). This Zeeman shift is $\Delta E = g\mu B$ which is illustrated in fig. 4.37 for both ^{38}Ar and ^{39}Ar.
In a setup of two counter propagating, red detuned laser beams the Zeeman effect provides a tool for spatial confinement of atoms. There are several realizations of such a magneto-optical trap that may vary in number and polarization of laser beams and in geometry of the magnetic field. The following applies to a case of three orthogonal pairs of circularly polarized beams combined with a magnetic quadrupole field.
"Polarization" is a tricky term in this context. In the lab frame, polarization refers to the handedness relative to the direction of propagation. Circular polarization can be either left-handed or right-handed. However, in the atom frame only the polarization rotation

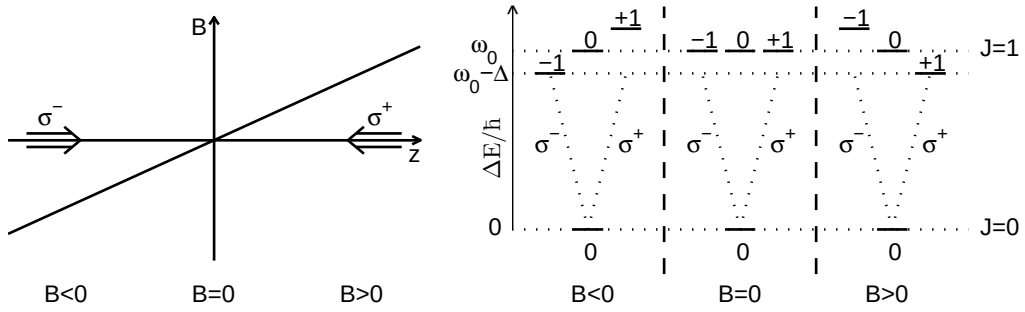

Figure 4.36.: Working principle of a magneto-optical trap. Red detuned laser light of circular polarization is combined with a magnetic field gradient. The further the atom moves away to one side from the MOT center the more resonant the beam from this side becomes, thus driving the atom back to the center. When the center of the MOT is crossed the roles of the laser beams switch, again driving the atom to the center.

relative to the quantization axis is important, which is denoted by the helicity σ^+ or σ^-. From angular momentum selection rules and the general convention follows that σ^+ light increases m by 1, $\Delta m = +1$, whereas $\Delta m = -1$ for σ^- light. Beams from either side of the MOT with the same handedness can be identified with σ^- and σ^+, respectively[20].
Fig. 4.36 illustrates the basic mechanism of the magneto-optical trap for the simplest system possible, $J = 0 \rightarrow J = 1$. The idea is that, depending on which side of the MOT an atom is, it is mainly influenced by the beam coming from that side. This drives the atom back to the center of the MOT where the forces from each of the beams are equal. The magnetic quadrupole field results in a spatially varying detuning

$$\Delta(v, r) = \Delta_L \pm kv \mp \mu' B(r)/\hbar \tag{4.44}$$

In analogy to the derivation of the velocity dependent force in an optical molasses (eq. 4.28), this modified detuning affects the dissipative light force (eq. 4.25). An approximation of the deduced expression in the low intensity limit for small Doppler- and Zeeman-shifts results in

$$\vec{F} = -\beta\vec{v} - \kappa\vec{r} \quad , \quad \beta : \text{damping coefficient as defined in eq. 4.28} \tag{4.45}$$

$$\kappa = \frac{\mu' A}{\hbar k}\beta \quad , \quad A : \text{magnetic field gradient.} \tag{4.46}$$

κ represents the proportionality factor of a force dependent on the distance from the center and is therefore identified as a spring constant. Rewriting the equation in a different way for the one dimensional case and an atom mass m clarifies this immediately:

$$\ddot{x} + \frac{\beta}{m}\dot{x} + \frac{\kappa}{m}x = 0 \tag{4.47}$$

[20] From [123]: "Note that these beam polarizations and the quantization axis of the atom have been defined relative to a fixed direction in space, i.e. the z-direction in this one-dimensional example. For $z > 0$ this is the same as the direction of the magnetic field, but for $z < 0$ the magnetic field points the opposite way; hence the $M_J = -1$ state lies above $+1$ in this region, [...]. Strictly speaking, σ^+ and σ^- refer to transitions of the atom and labeling the radiation as σ^+ is shorthand for circularly-polarized radiation of the handedness that excites the σ^+ transition (and similarly for σ^-)."

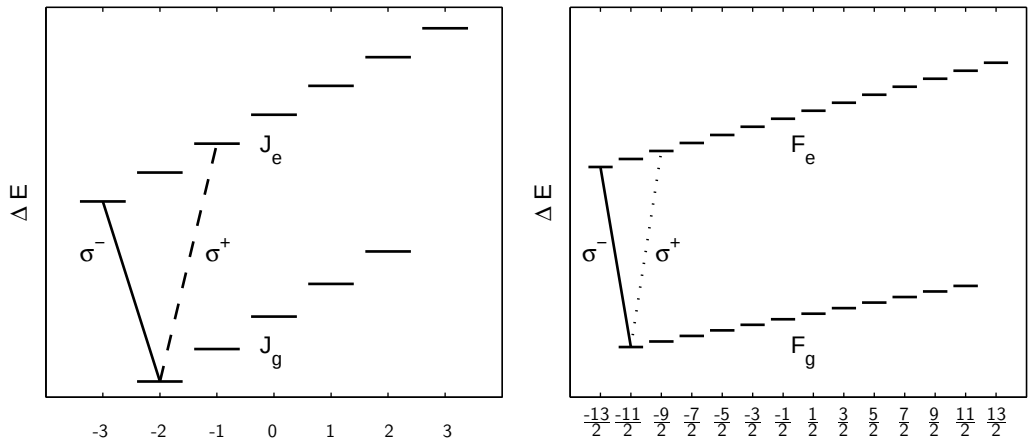

Figure 4.37.: Comparison between the Zeeman splitting in ^{38}Ar (left-hand) and in ^{39}Ar (right-hand). $B = 2.3$ G and $\delta_{MOT} = -6$ MHz in this calculation. The vertical scaling is the same for both plots. Even though ^{39}Ar has substantially smaller g_g and g_e, the maximum effective magnetic moment is still the same for all argon isotopes. However, the influence of the "expanding" beam is much higher in ^{39}Ar as it is closer to resonance.

This differential equation is solved by a damped harmonic oscillation with damping rate $\Gamma_D = \beta/m$ and oscillation frequency $\omega_r = \sqrt{\kappa/m}$ (use $x = e^{rt}$ as ansatz). Typical values (e.g. $1s_5 - 2p_9$ transition of Ar) lead to $\Gamma_D \approx$100kHz and $\omega_r \approx 1$ kHz. The conclusion is that the atoms follow an overdamped oscillation around the zero point of the B-field as it can be seen in the top-left plot of fig. 4.40.
Expanding the setup to three dimensions leads to the "magneto-optical trap". The velocity of the atoms is reduced by a 3D optical molasses and the spatial confinement is provided by the magnetic field.
The major difference between ^{39}Ar and the stable isotopes regarding laser cooling is the hyperfine splitting in ^{39}Ar. This directly affects the magneto-optical trap such that the net cooling force decreases, which will be illustrated in the following.
A comparison of the Zeeman splitting of the respective cooling transitions in ^{39}Ar and any stable argon isotope is provided in fig. 4.37. It is obvious that the detuning of the σ^+ transition is less for ^{39}Ar than for e.g. ^{38}Ar when the σ^- transition is resonant. The result is a larger force from the beam that drives the atoms away from the center of the MOT and thus a smaller net force in direction of the center.
The spatially varying detuning for σ^- and σ^+ light for a linearly varying magnetic field is shown in fig. 4.38. Given the natural linewidth, it becomes clear that the net force is much smaller for ^{39}Ar, especially close to the center of the MOT. Due to the nature of Gaussian beams, the intensity is the highest in the center of the trap, thus leading to larger linewidth and even smaller restoring force. In the end, this causes the ^{39}Ar MOT to be larger in size and the ^{39}Ar atoms being more complicated to detect.

4.7.2. Doppler limit and sub-Doppler cooling mechanisms

Laser cooling with near-resonant light always involves scattering processes. Therefore, the lower temperature limit for these types of cooling schemes is given by the recoil from

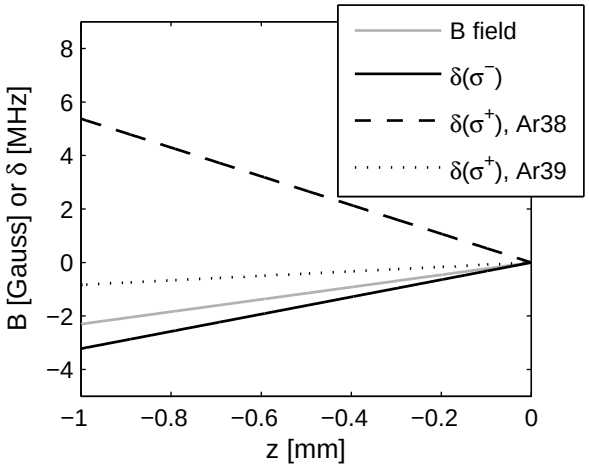

Figure 4.38.: Spatially varying detuning δ with 23 Gauss/cm gradient. The difference between σ^- and σ^+ light decreases about a factor 4 stronger for ^{39}Ar than for ^{38}Ar. The measured size of the MOT is on the order of 100 µm radius where the difference in detuning between the two beams is just about 0.2 MHz for ^{39}Ar.

one photon: $T_r = \frac{(\hbar k)^2}{2k_B m}$. The recoil temperature T_r is typically on the order of hundreds of nK, which corresponds to a speed of several cm/s. Lower temperatures can be achieved by evaporative cooling where the hottest atoms leave the cloud and the ensemble re-thermalizes.
However, atoms in a MOT typically have much higher temperature. So far, only cooling mechanisms are considered but there is also heating. Absorption and emission have different Doppler shifts which causes the light field to lose $2\hbar\omega_r$ per scattering process. Energy conservation requires that this energy is transferred to the atoms in form of kinetic energy. The equilibrium temperature is reached when cooling and heating cancel, $T_D = \frac{\hbar\Gamma}{2k_B}$. It is in the range of hundreds of µK for typical elements.
Again, this is not the temperature that is usually found, the experimentally observed temperatures lie somewhere between T_r and T_D. In order to explain this behavior one or more additional cooling mechanisms have to take place. They can only be understood when the "light shift" is considered. In the simple picture mentioned above (sec. 4.3.1) this shift of the energy levels stems from the interaction between atom and electro-magnetic field.
The situation of two counter propagating beams with orthogonal circular polarization results in a spatially rotating linear polarization, a corkscrew standing wave. Atoms that travel along this polarization gradient travel up and down the light shift potential landscape. Traveling uphill leads to reduced kinetic energy and increased potential energy. At the top of the hill the atoms are optically pumped to a different (now lower) ground state, thus release their potential energy and travel uphill again.

4.7.3. Calculation of MOT loading

The findings in the previous section already suggest that laser cooling and trapping works less efficient for ^{39}Ar than for ^{38}Ar. Hence, a basic 1D calculation of the longitudinal motion of atoms passing the MOT beam has been carried out.

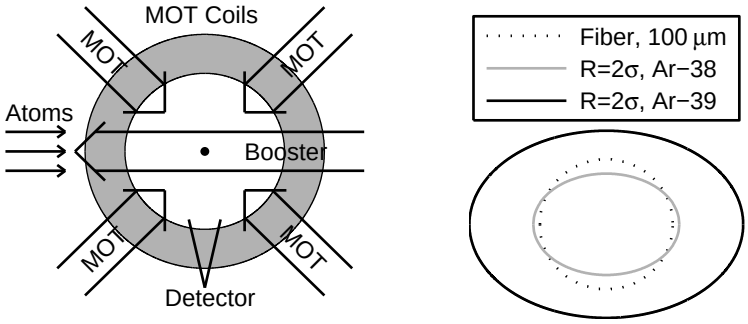

Figure 4.39.: Left-hand: setup of the MOT beams with the additional booster beam. The open triangle illustrates the direction of detection. Right-hand: Calculated MOT image on the fiber for ^{38}Ar and ^{39}Ar, 13.5 % radius.

It takes into account that the longitudinal trapping is accomplished by two orthogonal pairs of horizontal beams under an angle of 45° relative to the atomic beam (see fig. 4.39, left-hand), thus leading to a reduced Doppler shift and a higher intensity. Optionally, a laser beam counter propagating the atomic beam is added, this is the afore-mentioned "booster" beam.
Illustrative information for experimentally optimized parameters is compiled in fig. 4.40. Without the booster the optimal MOT beam detuning for capturing ^{39}Ar is around -20 MHz. This however is way too large for efficient detection. But as it can be seen in the corresponding plot, a detuning of -4 MHz with intensity $I = 1 \cdot I_0$ does not allow for trapping ^{39}Ar.
Other ATTA experiments [2, 14] use a toggling scheme between two sets of parameters, one for loading the MOT, the other for detection of atoms. A detailed discussion regarding this issue can also be found in [66]. As illustrated below, the lifetime of the MOT is limited to about 200 ms. Therefore toggling is not the optimum solution as it would reduce the detection efficiency.
Adding a near-resonant longitudinal beam entirely solves this issue. Effectively, a second Zeeman slower is realized with the magnetic field of the MOT. This even increases the capture efficiency: The capture range is enlarged towards higher velocities. Hence, the final Zeeman slower velocity v_f can be increased which leads to less beam divergence. The experimentally found gain with the booster is about 2-3 but, of course, strongly depends on v_f.
From the calculation it can be concluded that atoms with up to ≈ 70 m/s can continuously be captured while the MOT is adjusted for optimum detection. This does not critically depend on the experimental parameters but the MOT center tends to shift significantly towards the source for too high booster intensities (e.g. $s_{booster} = 10$: $\Delta z_{39} \approx -1.5$ mm, $\Delta z_{38} \approx -0.5$ mm).

4.7.4. Calculation of MOT size

Fig. 4.38 predicts that the effective detuning between cooling and heating beam is smaller for ^{39}Ar than for the even isotopes. This leads to a weaker net force on the atoms and results in a larger MOT size for ^{39}Ar.

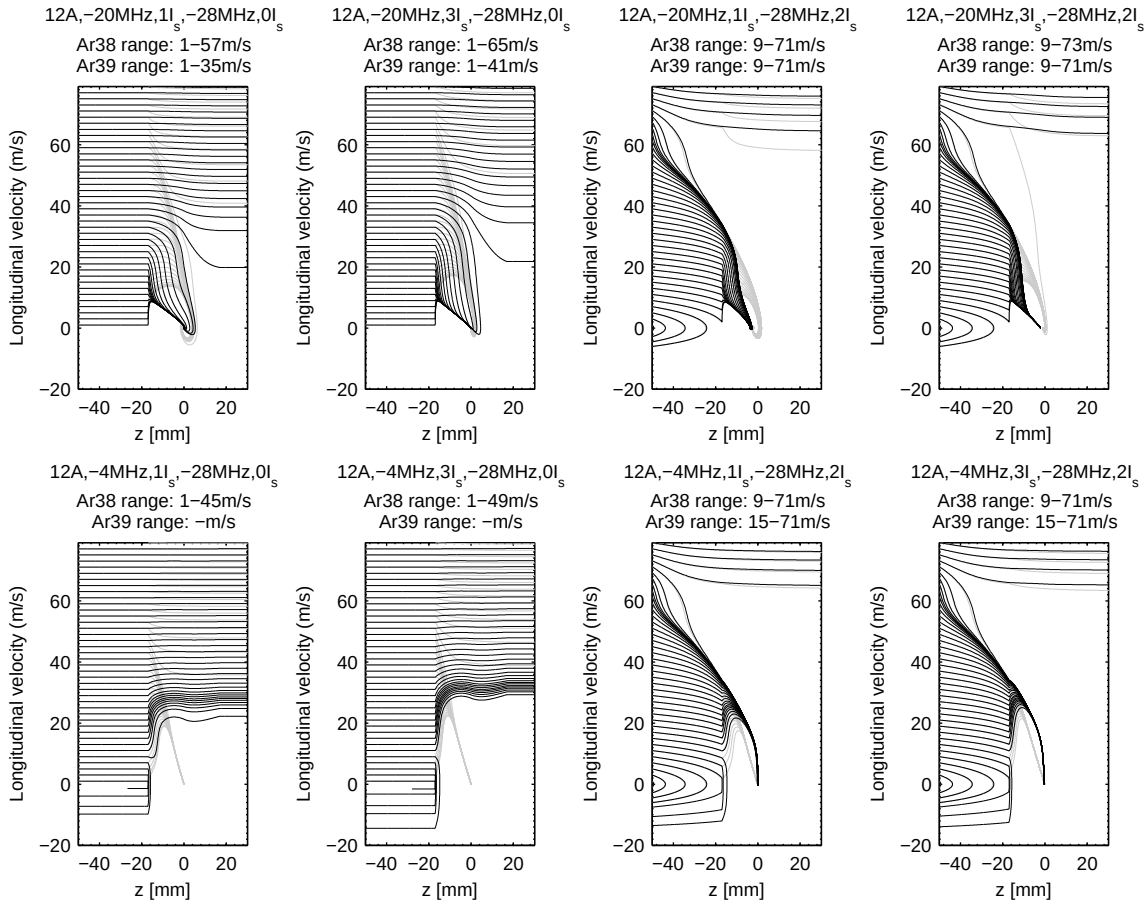

Figure 4.40.: Results from calculation of the MOT for different parameters. Gray shaded curves are trajectories for ^{38}Ar, black lines for ^{39}Ar. For each subplot, the parameters are indicated in the top line: coil current, MOT detuning, MOT intensity, booster detuning, booster intensity. Comparison between top left and bottom left figures illustrates that without booster beam the detuning for efficient ^{39}Ar loading is very different from that for detection. The figures on the right-hand side show the improvement by the booster.

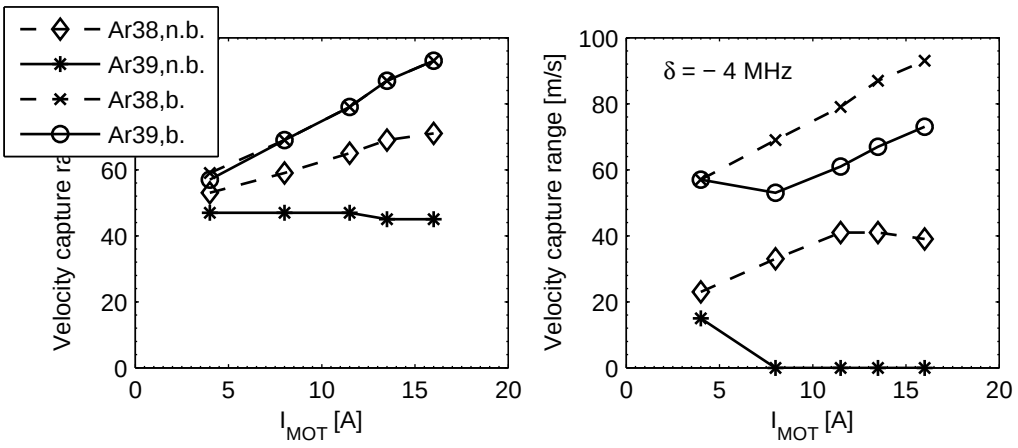

Figure 4.41.: Velocity capture ranges for ^{39}Ar and ^{38}Ar as a function of magnetic field current. Diamond and circles correspond to calculations without a booster ("n.b."), crosses and asterisks are with booster ("b."). Left-hand: Absolute maxima found for the full range of calculated experimental parameters. Right-hand: Capture range with optimum parameters for detection, with and without booster. The improvement is especially significant for ^{39}Ar and for booster saturation $s \geq 2$ practically constant.

In the following the expected MOT size is calculated for odd and even isotopes of argon. For simplicity a mass $m = 39\ m_u$ is assumed for all isotopes. Bearing in mind that the root-mean-squared velocity of atoms in a MOT is typically (see e.g. [40])

$$v_{rms} \approx 20\frac{\hbar k}{m} \tag{4.48}$$

it is possible to estimate the size of the MOT. Fig. 4.42 depicts the position dependent force $F(z)$ in a MOT with $s_{beam} = 0.5$. Close to the MOT center F is approximately linear with the position x,

$$F \approx -k \cdot x, \tag{4.49}$$

where k denotes the spring constant. As usually, Newton's second law of motion applies and yields the following differential equation

$$m \cdot \ddot{x} \approx -k \cdot x. \tag{4.50}$$

Plugging in the boundary conditions ($\dot{x}(0) = v_{rms}$, $x(0) = 0$) results in the well-known harmonic oscillator,

$$x(t) = x_{rms} \cdot \sin\left(\sqrt{\frac{k}{m}}t\right) \tag{4.51}$$

with

$$x_{rms} = 20 \cdot \frac{\hbar k}{\sqrt{k \cdot m}}. \tag{4.52}$$

Given $k_{odd} \approx 0.79 \cdot 10^{-18}$ N/m and $k_{even} \approx 2.75 \cdot 10^{-18}$ N/m from fig. 4.42 leads to

$$x_{rms,odd} = 72\ \mu\text{m} \quad \text{and} \quad x_{rms,even} = 39\ \mu\text{m} \quad \text{for dB/dx} = 23\ \text{G/cm}. \tag{4.53}$$

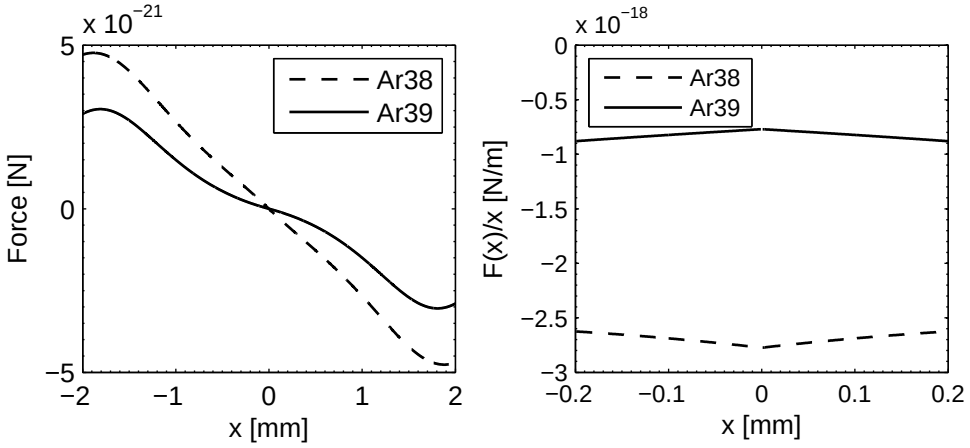

Figure 4.42.: Left-hand: Position dependent cooling force for ^{38}Ar and ^{39}Ar in the MOT. Right-hand: corresponding force gradient.

For the radial MOT axis corresponding parameters are obtained,

$$x_{rms,odd} = 103\ \mu\text{m} \quad \text{and} \quad x_{rms,even} = 55\ \mu\text{m} \quad \text{for dB/dx} = 11.5\ \text{G/cm}. \tag{4.54}$$

Then, assuming that the detector has a finite circular size with 100µm radius (which applies to the optical fiber used, see right-hand plot in fig. 4.39 for an illustration) and performing a 2D-integration leads to a MOT-image to fiber efficiency of

$$\eta_{odd} = 49\% \quad \text{and} \quad \eta_{even} = 90\%. \tag{4.55}$$

Similar results are found in the experiment, as the ^{39}Ar signal is 16.8 kcps and the ^{38}Ar signal is 28.5 kcps, see chapter 5.
A possible future improvement might be the implementation of modified MOT coils with better cooling. This would then allow for higher current and, consequently, a larger B-field gradient. Hence, the MOT size would be further reduced, leading to substantially improved detection of ^{39}Ar atoms.

4.7.5. Realization

The magneto-optical trap is realized with a pair of cylindrical coils with opposite direction of current. With the help of Biot-Savart's law the magnetic field can be calculated easily. Due to the opposing sense of current all even derivatives are zero in the center between the coils. Ideally, the distance between the coils would be $D = \sqrt{3}R_{coil}$ ("anti-Helmholtz configuration", "Maxwell-coil") as this also results in a vanishing 3rd derivative of the field. Thus, the gradient becomes as constant as possible.
Nevertheless, in the current coil setup small deviations from a linear magnetic field could not be avoided. Power dissipation in the coils becomes more and more problematic with increasing coil radius (higher resistance for same field strength) thus distance and radius should be as small as possible. However, the geometry of the vacuum chamber leads to further restrictions of these parameters. Hence the mean coil radius is $R = 54$ mm and the distance between the coils is $D = 130$ mm. The corresponding field and gradient are

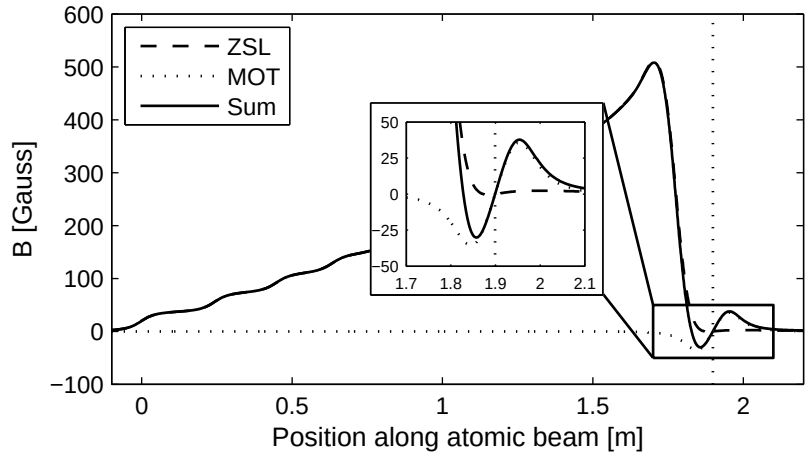

Figure 4.43.: Combined magnetic field of Zeeman slower, compensation and MOT coils (I_{MOT} = 12 A). The residual field and gradient of the Zeeman slower at the position of the MOT center (zero-crossing) is sufficiently small to allow for the MOT to be relatively unperturbed. The close-up further illustrates this.

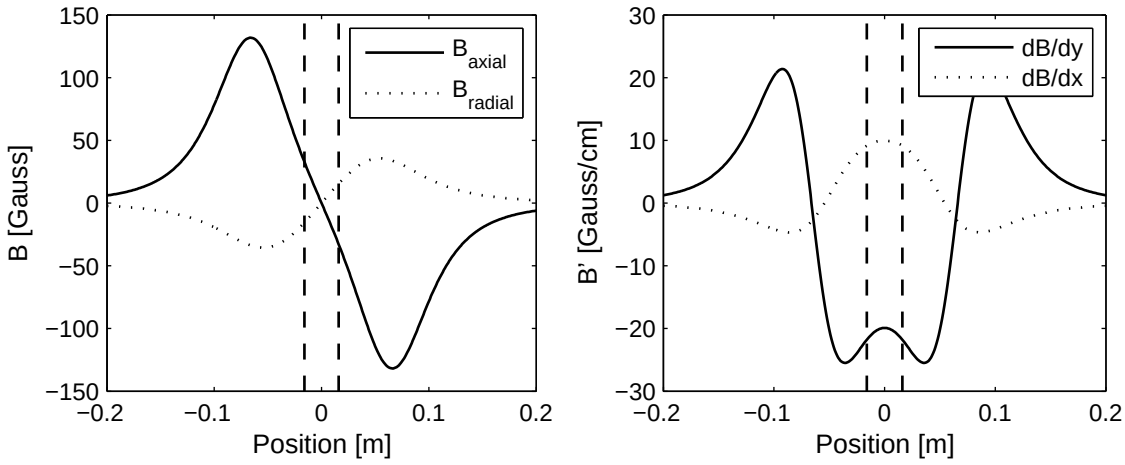

Figure 4.44.: Magnetic field of the present MOT coil configuration with I_{MOT} = 12 A. Left-hand: B field along the axial direction (connecting the two coil centers) and in the radial plane. Right-hand: respective magnetic field gradients. Due to Gauss's law for magnetism $\nabla \cdot \mathbf{B} = 0$ the axial gradient is twice the negative radial gradient at the position of the MOT. Dashed vertical lines indicate the size of the trapping beams.

shown in fig. 4.44 and were explicitly calculated for the exact wire configuration.
Still, coil cooling is limiting the maximum gradient to about 22 Gauss/cm which already leads to significant heating of the MOT chamber. Therefore a set of new coils is currently being build. It features more efficient water cooling and has $R = 32.5$ mm, $D = 90$ mm.
The light for the MOT is guided from the MOT-TA to the experimental chamber via a 1×4 polarization maintaining fiber splitter[21]. Three of the splitter's outputs are connected to self-made fiber collimators (focal length 150 mm, 13.5 % beam diameter of 32 mm). These collimators feature a rotable $\lambda/4$-plate for circular polarization.

4.7.6. Loading rate vs. lifetime

In the course of this ATTA experiment three key figures serve to characterize the MOT. The loading rate R has to be maximized to reduce the measurement time. At the same time, the MOT's lifetime τ and its size have to be such that atoms can be detected efficiently.
Loading and decay of the magneto-optical trap can be approximated by a simple differential equation. Assuming a constant loading rate R, a loss rate $\gamma = 1/\tau$ given by collisions with the background gas, and two-body collisions between trapped atoms[22] at a rate β leads to the following equation system for the number of atoms N in the MOT:

$$\dot{N} = R - \gamma N - \beta N^2 \tag{4.56}$$

$$N(0) = N_0 \tag{4.57}$$

For a small mean number of atoms in the MOT two-body collisions are negligible and eq. 4.56 is easily solved to

$$N(t) = \frac{R}{\gamma}\left(1 - e^{-\gamma t}\right) + N_0 e^{-\gamma t} \tag{4.58}$$

For the more complicated situation, MATLAB's "dsolve" function gives solutions of eq. 4.56 for the two situations MOT loading ($N_0 = 0, R = R_{load}$) and MOT decay ($N_0 = N_{equ}, R = 0$):

$$N_{load}(t) = \frac{1}{2\beta}\left[-\gamma + \tanh\left(\frac{1}{2}t\sqrt{4R\beta+\gamma^2} + \operatorname{atanh}\left(\frac{\gamma}{\sqrt{4R\beta+\gamma^2}}\right)\right)\cdot\sqrt{4R\beta+\gamma^2}\right] \tag{4.59}$$

$$N_{decay}(t) = \frac{\gamma}{\gamma + \beta N_0\left(1 - e^{-\gamma t}\right)}\cdot N_0 e^{-\gamma t} \tag{4.60}$$

The loading rate R is proportional to the flux of slow metastable atoms through the capture region of the MOT. It can be optimized without affecting the detection by tuning either the collimator, the MOL or the Zeeman slower. The source pressure however cannot be adjusted independently. For an optimum metastable flux, source pressures around $5\cdot10^{-5}$ mbar are optimal. In turn, this results in higher pressures in all parts of the vacuum apparatus. As illustrated in sec. 5.5, the lifetime of the MOT should ideally be

[21] The coupling and transmission efficiency amounts to about 40 % which is mainly due to the TA beam profile. The power per splitter channel is constant down to a few percents and three of the four ports have similar power.

[22] Strictly speaking, also collisions with the background gas are two-body collisions. But, as these are only proportional to N, they are simply treated as loss.

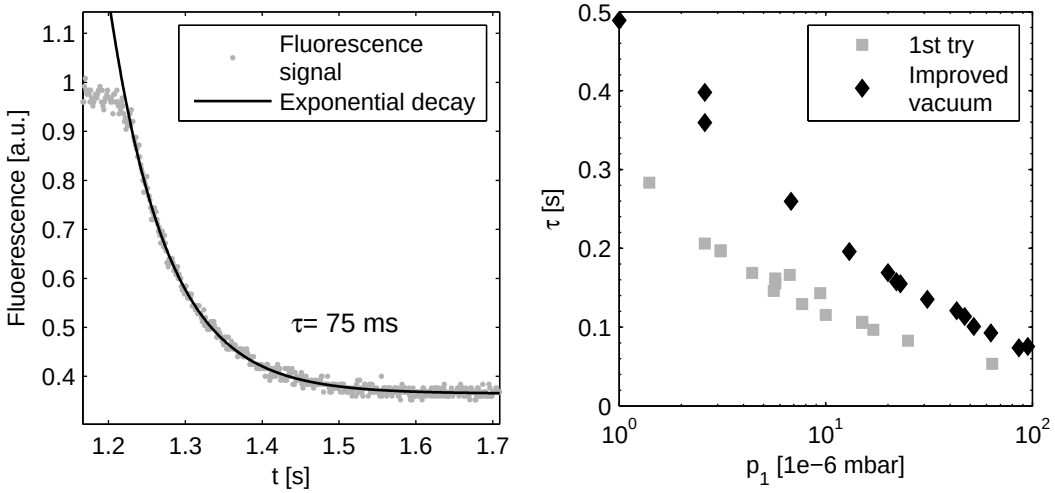

Figure 4.45.: Left-hand: Decay of a small ^{38}MOT at a source chamber pressure of 10^{-4} mbar. Right-hand: τ as a function of the source chamber pressure p_1 for the previous and the current vacuum setup.

150 ms or above.
γ only takes into account contributions from those atoms that are not trapped, and several factors contribute to this collision rate. Firstly, there is residual gas in the apparatus whose partial pressure p_{bg} is given by the apparatus temperature and the pumping speeds.
Secondly there are collisions with argon atoms. These could either occur with directed atoms in the beam or with atoms from isotropic directions due to background argon. Both contributions should scale linearly with the source pressure. The total collision rate is therefore

$$\gamma = \gamma_{bg} + \gamma_{bg}^{Ar} + \gamma_{beam}^{Ar}. \tag{4.61}$$

Fig. 4.45 summarizes the results from lifetime measurements with a small ^{38}Ar MOT. The mean number of atoms in the MOT was approximately 100, thus collisions between trapped atoms do not play a role.
In order to derive the lifetime, the Zeeman slower laser is periodically switched off. Then, the loading rate is $R = 0$ and an exponential decay according to eq. 4.58 is observed. For the original vacuum setup the lifetimes where found to be too short for efficient detection. Therefore, additional pumping stages where implemented and the distance between the MOT chamber and its vacuum pump was reduced. Now, efficient detection is still possible for higher source pressures up to $1.5 \cdot 10^{-5}$ mbar[23].
Plugging an expression corresponding to eq. 4.5 into 4.61 results in

$$\gamma = \gamma_{bg} + \left(n_{bg}^{Ar} \cdot \bar{v}_{bg} + n_{beam}^{Ar} \cdot \bar{v}_{beam} \right) \cdot \sigma_{mg}^{MOT}, \tag{4.62}$$

which allows to compute the metastable ground state cross section for atoms in the MOT. With the conductivity L between MOT chamber and pump, the pumping speed S, the

[23] Since recently, the MOT coils tend to heat up the apparatus. This leads to large residual gas pressures in the MOT. It limits the lifetime to about 100 ms, thus reducing detection efficiency by about 10%. This issue will be resolved in the near future.

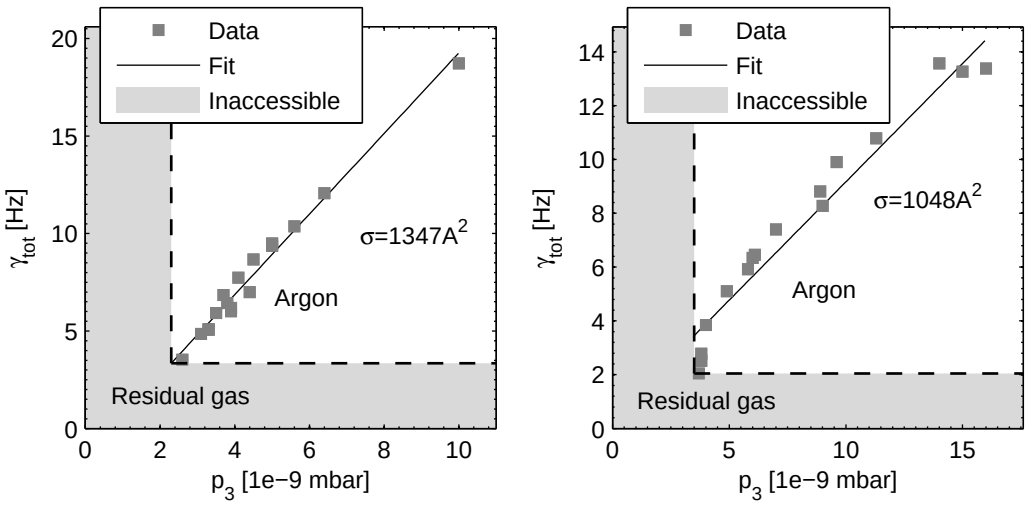

Figure 4.46.: Loss rate γ in the MOT. This allows for determination of the scattering cross section of ground state atoms and trapped metastable atoms as $\gamma = k \cdot \sigma_{mg} \cdot p$. Left-hand: Previous vacuum setup. Right-hand: Improved vacuum setup. Grey shaded areas are inaccessible due to residual gas pressure.

beam area A_{beam} and the $T_{bg} = 300$ K, the previous equation writes as function of pressure

$$\gamma = \gamma_{bg} + \sigma_{mg}^{MOT} \cdot \left(\frac{S+L}{L} \cdot \bar{v}_{bg} + \frac{S}{A_{beam}} \right) \cdot \frac{p_{3,real}^{Ar}}{k_B \cdot T_{bg}}, \tag{4.63}$$

where $p_{3,real}^{Ar}$ is the real argon pressure in the pump chamber, $p_{3,real}^{Ar} = 1.3 \cdot (p_{3,apparent} - p_{bg,residual})$. For experimental convenience the plots in fig. 4.46 use the apparent pressure. They comprise results for the two afore mentioned vacuum setups and the slope of $\gamma(p)$ yields σ_{mg}^{MOT}. The experimentally determined cross section

$$\sigma_{mg}^{MOT} = 1198 \pm 211 \text{ Å}^2 \tag{4.64}$$

obtained from MOT lifetime measurements is by a factor of 4.0 ± 0.7 larger than the value previously found by diffusion measurements ([93, 94], eq. 4.4). However, this factor agrees well with measurements in metastable neon ($\sigma_{mg}^{MOT} = 556$ Å^2 [124], $\sigma_{mg} = 158$ Å^2 [125, 94]). Similarly, a dependence of the cross section on the collision energy serves as explanation for this deviation.

4.7.7. Optimization

The MOT was first adjusted for a high ^{38}Ar loading rate. In order to achieve the maximum possible, the beam aperture diameter is 34 mm while the waist is 16.5 mm. Zeeman slower current, Zeeman and booster laser frequencies and intensities were adjusted such that the maximum loading rate is achieved.
Determining the loading rate is non-trivial for loading rates in the range of $R = 10^{11} - 10^{12}$ atoms/s. The reason is the two-body loss coefficient that rapidly limits the maximum number of atoms for the high R. However, the figure of merit is not the stable argon

loading rate but that of ^{39}Ar.
Accordingly the apparatus was further optimized with an enriched ^{39}Ar sample. Hence, the repumper intensities and frequencies could be tuned to produce the largest possible ^{39}Ar MOT.
This procedure is not without risk. It has still to be determined whether outgassing of the enriched sample from the vacuum apparatus limits further measurements. However, it has been found that it is not an issue when the apparatus runs in flow mode and does not operate in recycling. Thus, the ^{39}Ar count rate for recent samples derived in the next chapter is valid and does not arise from contamination.

5. Single atom detection

5.1. Particle detection

A physicist's toolbox contains quite a number of methods for the detection of single particles. These mostly employ specific properties of the particles to be investigated such as radioactive decay, formation of ions, charge, mass, etc.. In the introduction of this thesis techniques such as AMS or LLC have already been briefly discussed. The following section tries to give an overview of the existing detection techniques for metastable noble gas atoms.

5.1.1. Faraday cup

One of the simplest detectors for high energetic particles is the Faraday cup. In a typical setup, it consists of a cup-shaped metal surface at negative potential with an insulated wire on the cylindrical axis.
Incident particles release electrons from the cup if their energy is high enough to overcome the work function of the electrode's material. In the case of an argon atomic beam apparatus this holds for UV photons, argon ions and metastable argon atoms. The electrons are then accelerated towards the wire and can be measured as a current between wire and ground.
The efficiency of this detector depends on the geometry of the cup, the materials used, and the surface polishing quality. An overview of related issues and an application example is provided in [126], where 15% efficiency is found to be a reasonable estimate.

5.1.2. Channeltron & microchannel plate

High energetic particles can also be detected with channeltrons and microchannel plates (MCPs). These two detectors make use of secondary emission of electrons. The incident particle's energy induces an electron avalanche by releasing an initial electron from the electrode. Like in the Faraday cup, the particle's energy has to be higher than the electrode's work function.
The electrons are further accelerated by a potential gradient along the electrode and multiple secondary emission processes can occur. Typically, a MCP detector setup consists of a stack of one or more MCPs at high potential (kV) and a subsequent electron detector. A higher number of MCP's in the stack leads to a higher electron current per particle but can result in reduced spatial resolution. In recent experiments in this work group [33, 34] a resistive anode served as position sensitive detector for metastable argon atoms.
The major drawbacks of these detectors for detection of single ^{39}Ar atoms at the expected

rate of 1 atom/h are obvious. Each detected particle produces only one electron pulse, thus the background pulse rate has to minimized. UV photons from the source have to be suppressed strongly, necessitating either deflection of the atomic beam or usage of a fast atomic beam shutter. Both methods will further reduce the already low efficiency of these detectors.
Apart from this photon induced background, any parasitic current from the detector has to be avoided, as the signal is afterwards amplified with a sensitive charge amplifier. In [40] the background was reduced to a few counts per minute which is still several orders of magnitude too large.
Even if the background count rate was negligible, further complications would arise in the discrimination of metastable ^{39}Ar from the abundant metastable argon atoms. So far, the previously mentioned atomic beam deflection seems the only feasible mechanism. The experimental effort, however, is not substantially less than for a magneto-optical trap which offers much higher detection efficiency and a lower background count rate.

5.1.3. Single atom fluorescence detection

Atoms in motion

Already as early as in 1977 single atoms have been detected by the photon burst method (PBM) [127, 128][1]. The technique works as follows: single atoms pass a near/on-resonant laser beam at about saturation intensity. The transit time is on the order of 10 µs for typical parameters. Given the scattering rates of favorable cycling transitions of $\approx$ 10MHz only about 100 photons are scattered per atom.
These fluorescence photons are collected by an elliptical mirror setup (up to 50% collection efficiency) and imaged onto a photomultiplier tube (PMT, quantum efficiency $\approx$ 10%). Whenever an atom is detected, a characteristic burst of photons appears on the detector. This can be clearly discriminated from the otherwise random distribution of background photon counts.
Signals are analyzed by integrating the photon count rate over a time window equal to the mean transit time through the laser beam. Then, a threshold is set above which the elevated count rate is identified as a single atom.
The theoretical limit for isotopic selectivity depends on the ratio of the frequency shift between isotopes to the linewidth of the transition, and on the threshold level. Practically, a limit is given by the background light, scattered from the laser beam due to imperfections in the optical setup. Isotopic selectivities as large as 10^{10} have been realized but in turn result in a very low detection efficiency ([130, 131]).

Photon burst mass spectrometry

A possible combination of mass spectrometers with the photon burst method could be used to further boost the isotopic selectivity of each method [132]. Given the isotopic selectivity of a simple mass spectrometer ($10^3 - 10^5$) and that of PBM (up to 10^{10}), the necessary selectivity for ^{39}Ar detection seems within the accessible range. Nevertheless,

[1] [129] provides a very instructive review article.

such a combined method again needs larger experimental effort and will probably result in a low detection efficiency. Still, compared with purely mass-spectrometric methods such as AMS or a purely laser-based method like ATTA these are favorable.

Trapped atoms

Interestingly, also as early as in 1977, the possibility of observing fluorescence light from trapped atoms has been proposed as a more promising method. The advantage is that the observation time per atom is by orders of magnitude larger. This offers much higher isotopic selectivity due to the larger number of accumulated fluorescence photons [133]. Trapping times in the range of seconds allow for about 10^7 scattered photons per atom. In principle, an elliptical mirror setup as above could also be employed here. Nevertheless, when detection efficiency is considered, large trapping beams are needed which reduce the observable solid angle. With a high numerical aperture objective ($NA > 0.3$) and a photon detector with high quantum efficiency ($> 50\%$) about 1% of the scattered light can be detected. Assuming perfect transmission of all optical components, the expected photon count rate per atom is up to 10^5 s^{-1}. Again, reduction of the background light is crucial and non-trivial in such a trap setup.

5.2. Detectors for few photons

Focusing on the detection of atoms by fluorescence, a quick introduction to some of the commercially available detectors for low photon count rates might be helpful. Here, three types of detectors are discussed, namely those that are actually employed in this experiment. The photomultiplier is used for characterization measurements of the atomic beam, as the high flux of atoms yields satisfying results. Single atom detection is realized with an avalanche photo diode and a CCD camera.

5.2.1. Photomultiplier tube

Photons incident on the entrance window of a photomultiplier tube (PMT) induce emission of electrons by the photo effect. Several electrodes ("dynodes") further accelerate these electrons and serve for secondary emission. Thus, the initially weak current is amplified and each detected photon leads to a well detectable current at the output of the PMT.
The main advantages of PMTs are the large active area ($1 - 100$ cm^2) and the adjustable gain by varying the dynode voltage. The quantum efficiency, however, is relatively low ($\approx 10\%$) and the devices are sensible to overexposure.

5.2.2. Avalanche photo diode

Semiconductor-based avalanche photo diodes (APDs) offer larger quantum efficiencies of 60% or more in the visible spectral range. They can have background count rates as low as a few tens of photons/s but feature only a small active area (tenths of mm^2).

Compact temperature controlled single photon counting modules (SPCM) are commercially available. These have a built-in circuit that levels the output to TTL pulses for each photon detected. Small pulse widths and detector dead times allow for fast counting at rates up to 10 MHz.
The modules used in this experiment feature a standard fiber port for optical fibers. This facilitates the implementation into the experiment. Besides this, optical fibers have much smaller acceptance angles than the APD which is convenient for suppression of background light.
A major experimental drawback is the limited size of the APD which complicates observation of atoms in a trap. In a MOT, atoms typically still cover distances of 100 µm which is similar to the size of the APD. Therefore, mechanical adjustment of the imaging optics and especially the position of the detector relative to the MOT center has to be stable on length scales of µm for well reproducible imaging.
In this experiment a Perkin & Elmer SPCM-AQRH-13 module is used. The quantum efficiency is around 50 % at 812 nm and the active area is $(180\ \mu m)^2$. An optical multimode fiber with core diameter of 200 µm ($NA \approx 0.37$) guides the collected photons from the experimental chamber to the detector[2]. The collecting fiber end is mounted on a 3-axis stage with micrometer screws that allows for optimization of position. The angle optimization is not critical and is done by bare eye (fiber plug parallel to optical axis).
The TTL pulses from the SPCM are recorded by a National Instruments PCI 6601 counter card. Integration time during data acquisition is 1 ms but during data analysis it is increased to 40 ms.

5.2.3. CCD, EMCCD

Charge-coupled devices (CCD) and more advanced designs (electron multiplying CCD, EMCCD) comprise advantages of both previously mentioned detector types. Yet increasing chip sizes of CCDs provide large active areas with quantum efficiencies higher than 90% for top models. There exist several temperature-controlled CCD-cameras with frame rates sufficient for clear time-resolved detection of single atoms.
These highly efficient devices clearly form ideal detectors. High-efficiency and low readout noise are combined with a large area facilitating adjustment. Unfortunately, these high-end scientific cameras are roughly by one order of magnitude more expensive than other detectors. Market prices for fast, high q.e. EMCCDs are found to range around 20 kEUR, thus limiting the wider application in science.
The model used here is a Hamamatsu C8484-05C with about 28 % quantum efficiency and an effective pixel size of $(6.45\ \mu m)^2$. The frame rate is limited to 50 frames/s, resulting in 20 ms time resolution. Image acquisition is realized within a Matlab environment such that it is synchronized with the APD data.

[2] Several fiber core sizes have been tested throughout the experiment. A core size of about 100 µm allows for detection of stable argon with much lower signal-to-noise. For ^{39}Ar 200 µm works better as the MOT is larger.

5.3. Fluorescence imaging

The conditions for successful single atoms detection by fluorescence are distinctly different from those for highly efficient loading of the MOT. Namely, there is an optimum set of parameters for each of the two modes. A small detuning leads to a high scattering rate per atom, while larger detunings increase the velocity capture range of the MOT. As mentioned above, this discrepancy is overcome by adding an additional frequency to the Zeeman slower beam. This decelerates atoms moving towards the MOT on the MOT's magnetic field gradient. A high scattering rate is then realized by near-resonant trapping beams.
Large saturation in the MOT beams is preferable for loading as it increases the capture range by power broadening. The capture region can also be increased due to the Gaussian power distribution in the beams.
However, detection of single atoms works better with medium to low intensities. There are basically two reasons for this. Firstly, large saturations correspond to high power, which increases the photon background from stray light. Secondly, it leads to power broadening, which in turn corresponds to a smaller spatial gradient in the net force on the atoms. Thus, the MOT becomes larger in size which results in a lower imaging efficiency. Both effects lead to a reduced signal-to-noise ratio for single atoms.

5.3.1. Design

The previous discussions provide clear requirements for a collector lens system. It has to have the largest possible numerical aperture given the mechanical restrictions of the experimental chamber and the size of the trap beams.
Once the light has been collected, it has to be imaged onto the detector. The design of the combined imaging system is governed by several boundary conditions. Firstly, in imaging systems the product of numerical aperture and image size is preserved. Thus, steep focusing down of the collected light will result in a small image. Secondly, for optimum signal-to-noise the image NA has to match the numerical aperture of the optical fiber used. Thirdly, bearing in mind that, on the one hand, there are practically no small-core-large-NA fibers available on the market and that, on the other hand, the fiber core size still has to be comparable to the APD size (which is about the MOT size), a 1:1 imaging system seems the optimum solution.
With the help of the lens design tool OSLO an objective made of standards lenses was designed, see fig. 5.1. The collector lens has a numerical aperture of 0.3 and a working distance of 41 mm. The minimum working distance d is given by the size of the MOT beams: $d >= r_{lens} + \sqrt{2}R_{beam}$. Here, R_{beam} is the aperture limited beam radius of 17 mm. The combined lens system consists of a total of six anti-reflection coated lenses (Melles-Griot). The combination of menisci and convex spherical singlets compensate for spherical aberrations. The bi-convex and the concave lens in the middle further reduce aberrations. By fine-tuning the distances between the lenses, the objective could also produce a diffraction limited image. This, however, is not necessary for the given purpose and the distance were chosen such that the setup is kept as simple as possible.

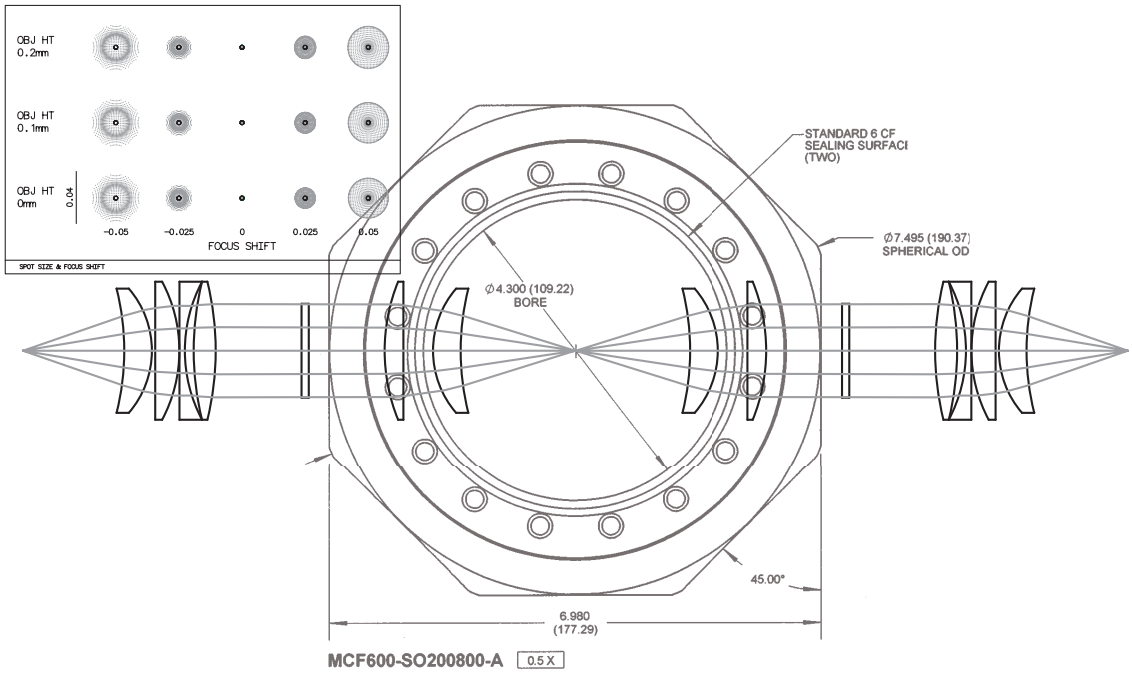

Figure 5.1.: Sketch of the imaging system relative to the experimental chamber. Two identical objective allows for simultaneous measurements with an APD and a CCD. The top-left inset provides results from OSLO where the black circles illustrate the diffraction limited spot size ("Airy disc").

5.3.2. Realization

The two first lenses that form the collector are mounted inside the vacuum chamber via a non-magnetic stainless steel tube. They are ground from 50 mm diameter down to 34 mm. Additional bore holes in the tube are necessary for pumping. The four remaining lenses are mounted outside the vacuum in a standard 2 inch lens tube (Thorlabs). 1:1 imaging was tested and provided satisfying results[3].
Background light is suppressed by applying black vacuum paint (AZ Technology MLS-85-SB) to the chamber walls. Stainless steel tubes (also painted black) on the vacuum side of the trapping beam viewports further reduce stray light.[4].
Substantial background is also produced by ^{40}Ar atoms that pass the trap beams (about 100-200 kcps on the APD, depending on metastable flux and laser power). These can be easily suppressed by using an additional laser at about 801.699nm. It is coupled into one of the MOL fibers and pumps ^{40}Ar to the ground state by driving the $1s_5$-$2p_8$ transition.

[3]This is done by setting up an identical lens system on the opposite side of the chamber and focusing a small MOT both onto the fiber (optimized for highest count rate) and the CCD camera (clearest image). So, both detectors are optimized on the MOT signal. Then, the fiber core (already illuminated by stray light) is also clearly visible on the CCD which shows that each of the two identical objectives work well.

[4]However, there is still room for improvement as the stray light is found to be mainly due to scattering from the viewports. They are already AR coated but higher grade surface quality might be helpful.

5.4. Estimation of the expected single atom count rate

Atoms in the MOT center will not only be cooled via transitions between stretched ground and excited states. The magnetic field vanishes in the MOT center and the quantization axis is not anymore defined properly.
Rather, the atoms are continuously pumped between the two stretched ground states $m_g = \pm F_g$ ($m_g = \pm J_g$ for even isotopes) while oscillating from one side of the MOT to the other. Therefore the saturation intensity for trapped atoms is not as defined in eq. 4.22 but by a factor of 2-3 larger (comp. [109] and own measurements).
Given the power of the MOT beam, $P = 5$ mW, and the MOT detuning, $\Delta_{MOT} = -4.2$ MHz, the intensity in the center of the MOT beams can be calculated. Per beam it is

$$I_0 = \frac{2 \cdot P}{\pi w_0^2} = 1.17 \frac{\text{mW}}{\text{cm}^2} \tag{5.1}$$

as the beam waist about 16.5 mm. For a saturation intensity of $I_s' = 3 \cdot I_s$ the saturation parameter is $s = 0.27$ and leads to an expected photon scattering rate of

$$\gamma_p = \frac{\Gamma}{2} \cdot \frac{1.62}{1 + 1.62 + \left(\frac{2 \cdot \Delta_{MOT}}{\Gamma}\right)^2} = 6900 \text{ kHz}. \tag{5.2}$$

In order to derive the photon count rate for one atom in the trap the efficiency of each step of the imaging system has to be known. Firstly, photons have to be transmitted through the objective which has a $NA = 0.25$, thus $\eta_{NA} = (0.25/2)^2 = 0.016$. Secondly, the transmission of the optical system is given by the reflection on the lenses' and window's surfaces. With a typical $T = 0.99$ for an AR coating this results in $\eta_{obj} = 0.99^{14} = 0.87$. The image to fiber efficiency is obtained from eq. 4.55, $\eta_{image,even} = 0.9$ and $\eta_{image,odd} = 0.49$.
Ideally, the uncoated optical fiber transmits $\eta_{fiber} = 0.96^2 = 0.92$. The same holds for the collimation lens in the APD fiber port, $\eta_{APD,T} = 0.92$. The fiber core of 200 µm diameter is slightly larger than the APD size of 180 µm which leads to $\eta_{APD,size} = 0.9^2 = 0.81$. Finally, the APD has a limited quantum efficiency of $\eta_{APD,q.e.} = 0.5$ at 812 nm.
Hence, the total photon detection efficiencies are $\eta_{even} = 0.0047$ and $\eta_{odd} = 0.0026$. By multiplication the latter with the above scattering rate the expected count rates per atom are

$$cr_{even,exp} = 32 \text{ kcps and } cr_{odd,exp} = 17 \text{ kcps} \tag{5.3}$$

This predicted count rate is found to be well reproduced by the experiment, see below.

5.5. Single atom identification

5.5.1. Determination of the ^{39}Ar loading rate

Given the ^{39}Ar loading rate R_{39}, the probability $p(k)$ to observe k ^{39}Ar atoms in the MOT during a time interval T_{det} is governed by a Poisson distribution,

$$p(k) = \frac{\lambda^k \cdot e^{-\lambda}}{k!}, \tag{5.4}$$

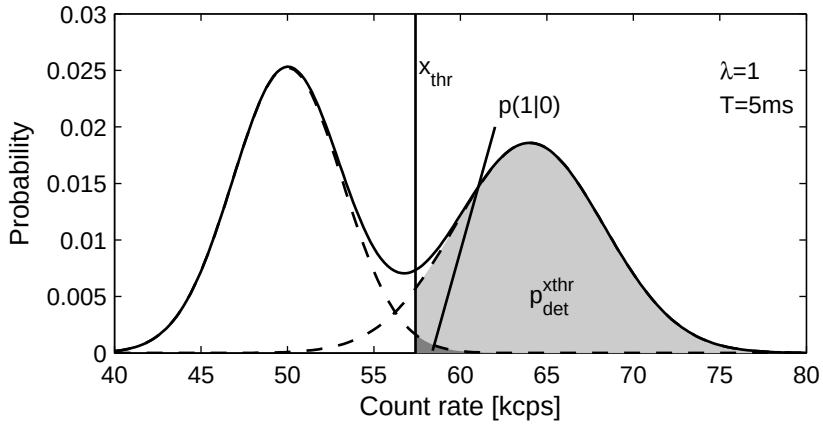

Figure 5.2.: Illustration of the threshold criterion. A count rate histogram is shown for $\lambda = 1$ (p(1) = p(0)). Here, $T = 5$ ms, $cr_{bg} = 50$ kcps and $cr_{sig} = 14$ kcps. Distributions for more than one atom are excluded.

where λ is the expectation value for the number of atoms during this interval,

$$\lambda = R_{39} \cdot T_{det}. \tag{5.5}$$

Likewise, the ^{39}Ar loading rate R_{39} can be derived from the probability $p(1)$ to detect one atom in the time interval T_{det}. Using eq. 5.4, the following expression has to be solved for λ:

$$\lambda \cdot e^{-\lambda} = p(1). \tag{5.6}$$

The accurate solution is given by the Lambert W-function but as $p(1)$ is on the order of 10^{-4} the following approximation holds down to an relative accuracy of about 10^{-4}:

$$\lambda = -W(-p(1)) \to p(1) \qquad (p(1) \ll 1)\,. \tag{5.7}$$

Hence, the loading rate R_{39} can be derived from the measured probability $p(1)$ and the detection interval T_{det},

$$R_{39} = \frac{p(1)}{T_{det}}. \tag{5.8}$$

5.5.2. ^{39}Ar detection probability

For each number k of atoms in the MOT the observed photon counts on the detector per integration time T follow a Poisson distribution. However, given the large number of photons this can be approximated by a Gaussian distribution with mean value μ_k and standard deviation $\sigma_k \geq \sqrt{\mu_k}$. Due to the small λ these observed μ_k are equidistant[5].
A simple threshold criterion is employed for atom identification: Whenever the detector signal x is larger than a certain x_{thr} with $x_{thr} > \mu_0$ for $\Delta t \geq T$, this counts as one atom. An illustration of the criterion can be seen in fig. 5.2. Δt corresponds to the exponentially distributed MOT lifetime,

$$p(\Delta t) = \frac{1}{\tau} \cdot e^{-\Delta t/\tau}, \tag{5.9}$$

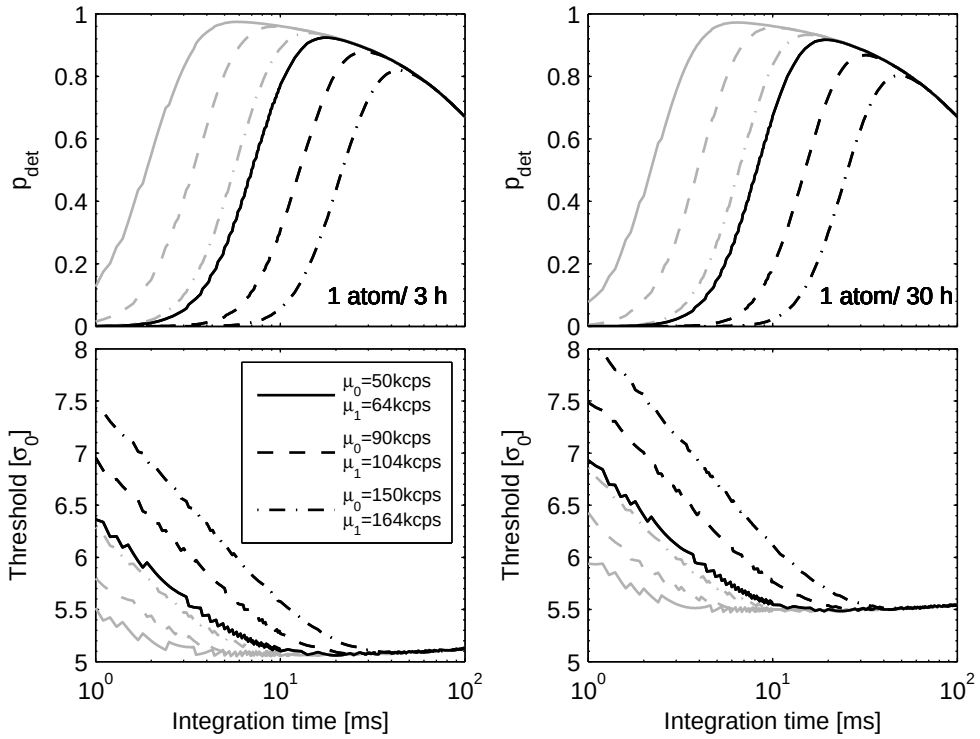

Figure 5.3.: Detection probability and threshold for a typical $\tau = 250$ ms. Left-hand: Loading rate 1 atom per 3 hours. Right-hand: Loading rate 1 atom per 30 hours. Grey lines: results for stable argon with a higher count rate per atom of 27 kcps. The threshold is normalized to the standard deviation of the background photon counts for each integration time.

where τ is the mean lifetime for atoms in the MOT. Hence, only a fraction of the atoms can actually be detected. This is governed by two statistical processes. Firstly, atoms with lifetimes shorter than T lead to a reduced signal, thus

$$p_{det}^{\tau} = \int_{T}^{\infty} \frac{1}{\tau} \cdot e^{-t/\tau} \mathrm{d}t = e^{-T/\tau}. \tag{5.10}$$

Strictly speaking, the integral only provides a lower limit for p_{det}. Some atoms might have lifetimes shorter than T but still lead to a signal above the threshold.
Secondly, the Gaussian distribution further reduces the detection probability as only atoms with a count rate above the threshold are counted. So, the detectable fraction due to this process is

$$p_{det}^{x_{thr}} = \int_{x_{thr}}^{\infty} \frac{1}{\sqrt{2\pi}\sigma_1} \cdot e^{-\frac{(x-\mu_1)^2}{2\sigma_1}} \mathrm{d}x = \frac{1}{2} - \frac{1}{2} \cdot \mathrm{erf}\left(\frac{x_{thr} - \mu_1}{\sqrt{2}\sigma_1}\right). \tag{5.11}$$

The standard deviation σ_0 is close to the Poisson noise but σ_1 is larger as further noise is introduced. This is mostly probably due to the MOT region being slightly larger than the image fiber end. It leads to σ_1 being larger by a factor of about 1.2.
Consequently, the probability to actually count an atom in during the integration time T is (results: see fig.5.3):

$$p(1,T) = p(1) \cdot p_{det} := p(1) \cdot p_{det}^{\tau} \cdot p_{det}^{x_{thr}}, \tag{5.12}$$

whereas the probability for false detection of an atom in the same interval is

$$p(1|0) = p(0) \cdot \int_{x_{thr}}^{\infty} \frac{1}{\sqrt{2\pi}\sigma_0} \cdot e^{-\frac{(x-\mu_0)^2}{2\sigma_0}} \mathrm{d}x = p(0) \cdot \left[\frac{1}{2} - \frac{1}{2} \cdot \mathrm{erf}\left(\frac{x_{thr} - \mu_0}{\sqrt{2}\sigma_0}\right)\right]. \tag{5.13}$$

The number of falsely detected atoms should be well below the aimed-at statistical error of the atom counts. For $n_{det} \geq 100$ the relative error is $\sigma_n^{rel} = \sqrt{n}/n \leq 10\%$), hence the limit for false counts is set to 1%. This is fulfilled when following inequality holds

$$p(1|0) \leq 0.01 \cdot p(1,T). \tag{5.14}$$

Plugging in eqs. 5.12 and 5.13 allows for calculation of x_{thr} as a function of the background and signal photon counts, and ^{39}Ar loading rate. Fig. 5.3 comprises results for different photon counts rates. In order to maximize $p(1|T)$, the threshold could be set to the minimum allowed by eq. 5.14.
There is always one problem with this approach as a priori knowledge of λ would be necessary. However, this is the quantity to be measured. But in the end, this is not a major problem as calculations yield a very weak dependence[6] of x_{thr} on λ.

5.6. Single Ar atoms

In order to optimize the single atom detection, it is adjusted with ^{38}Ar. Therefore, the loading rate of the MOT has to be reduced significantly. After optimization of the overlap

[5] Large densities in the MOT would lead to resonant re-absorption of scattered photons.
[6] A factor 10 decrease in ^{39}Ar flow only moderately increases the threshold by about $0.5\sigma_0$ for parameters close to those in the experiment.

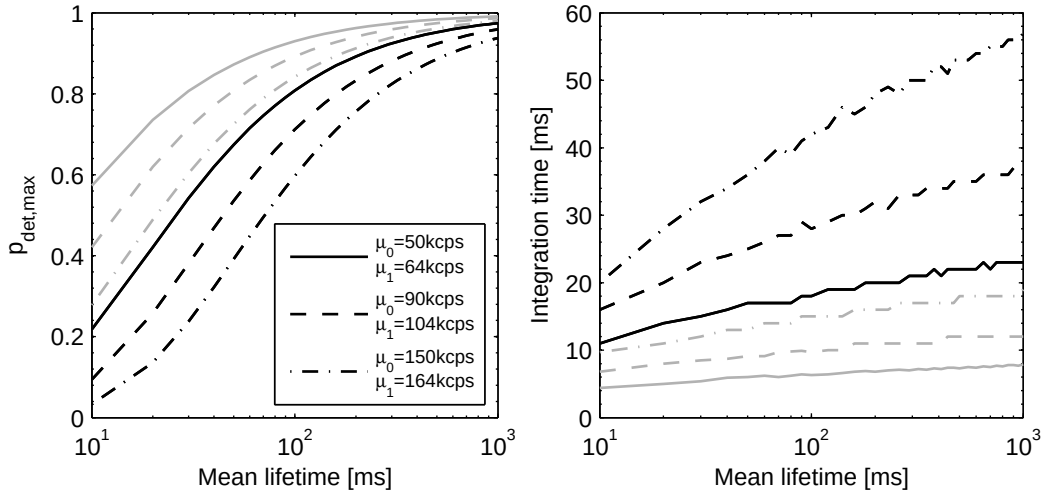

Figure 5.4.: Left-hand: Maximum detection efficiency for a loading rate of 1atom/3h. Different background photon rates and scattering rates per atom lead to different threshold values, thus limiting the number of detectable atoms. Right-hand: Optimum integration time to achieve highest detection efficiency. Discontinuities are due to numerical discretization.

between MOT and imaging fiber core, a signal as in fig. 5.5 emerges.
The photon count rate increases and decreases in quasi-discrete steps. This step-like character is further illustrated by the count rate histogram. It consists of several equally spaced Gaussian peaks corresponding to a varying number of atoms in the MOT.
Thorough analysis of the fluorescence trace allows to compute important parameters of the MOT. On the one hand, the probability for each number of atoms follows a Poisson distribution and can be reproduced by integrating each of the peaks separately. From this, the mean number of atoms λ can be derived.
λ can also easily be calculated differently, but still with help of the histogram. As in the previous section, the count rates for "background" and "1 atom" are denoted μ_0 and μ_1, respectively. λ is then obtained by averaging the APD count rate cr over time:

$$\lambda = \frac{\overline{cr} - \mu_0}{\mu_1 - \mu_0}. \tag{5.15}$$

On the other hand, the correlation length of the fluorescence signal, as obtained from autocorrelation, provides an accurate measure of the MOT lifetime τ, see fig. 5.7[7].
With the help of τ and the total measurement time T_{run} the number of atoms detected is estimated as

$$n_{det} = \frac{T_{run}}{\tau} \cdot \lambda. \tag{5.16}$$

Isotopically enriched samples with a relative ^{39}Ar abundance of 10^{-9} provide means to optimize the detection for this isotope. Fig. 5.6 demonstrates detection of single ^{39}Ar atoms. For this measurement, the flux was reduced to make the background peak clearly visible. Having all parameters optimized, the mean number of atoms in the trap ranges around 10 with a lifetime of 150 ms.

[7]Whenever an atom is in the MOT, the APD count rate is higher while the background photon rate is uncorrelated. Thus, the correlation length is a direct measure of τ.

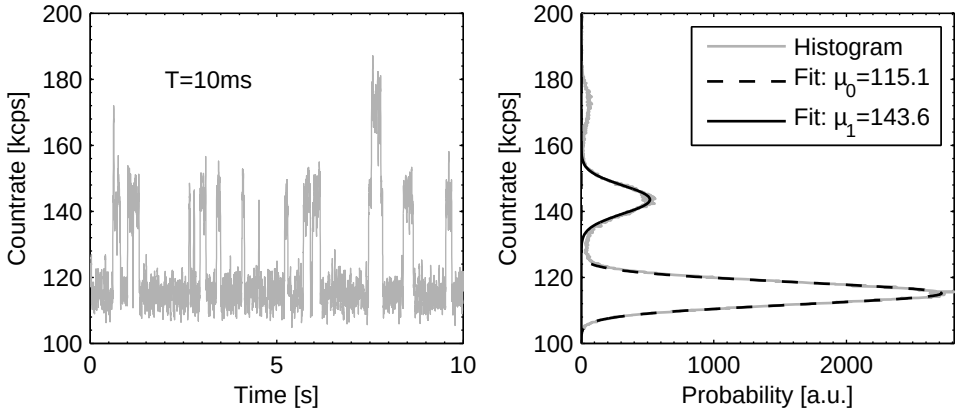

Figure 5.5.: Left-hand: Fluorescence signal of ^{38}Ar atoms on the APD. For clearness, only part of a longer run is shown. Right-hand: The histogram of the full run further reveals the stepwise increase of the photon count rate. The spacing between the histogram peaks corresponds to the single atom photon count rate which is 28.5 kcps for ^{38}Ar (and the other stable isotopes). Deviation from pure Gaussians in-between the peaks is due to the integration.

Given the approximate concentration[8] of 10^{-9}, the expected count rate with a recent atmospheric sample can be estimated:

$$R_{rec} \approx R_{enr} \cdot \frac{8.5 \cdot 10^{-16}}{10^{-9}} = \frac{10}{0.15\text{s}} \cdot 8.5 \cdot 10^{-7} = \frac{1\text{atom}}{4.9\text{h}} \tag{5.17}$$

Given the large uncertainties involved, especially in the concentration of the enriched sample, the agreement with the results presented in the section below is already remarkable. As already calculated above, the single atom signal for ^{39}Ar is weaker than for stable isotopes. For each ^{39}Ar atom about 16.8 kcps are detected, whereas 28.5 kcps are detected for each ^{38}Ar, which agrees well with the prediction from the MOT in sec. 5.4.

5.7. ^{39}Ar detection in atmospheric argon

The previous sections comprised measurements and estimations from stable isotopes and enriched samples. However the level structure of ^{39}Ar is very different from the stable isotopes. And additionally, the errors in flux measurement and enrichment factor only allow for a rough estimation of the expected ^{39}Ar count rate.
Hence, measurements with atmospheric argon from a gas bottle have been carried out. In a total run-time of 61 hours 18 atoms have been clearly identified, see fig. 5.8:

$$R_{39} = \frac{18 \pm \sqrt{18}\ \text{atoms}}{62\ \text{h}} = 0.29 \pm 0.07 \frac{\text{atoms}}{\text{h}} \tag{5.18}$$

Nevertheless, this might be underestimated. Hence, fig. 5.9 compares the histogram of the time lag between atoms (binning: 2 hours) with the results from an exponential curve.

[8] The sample is produced from neutron irradiated biotite samples, each containing about 1 nLSTP ^{39}Ar. The extracted gas sample is expanded to a volume of ≈ 1 L. Then, argon from a gas bottle is added until a pressure of 1bar is reached. This results in 1 nLSTP ^{39}Ar in 1 LSTP Ar, hence the ^{39}Ar concentration is 10^{-9}.

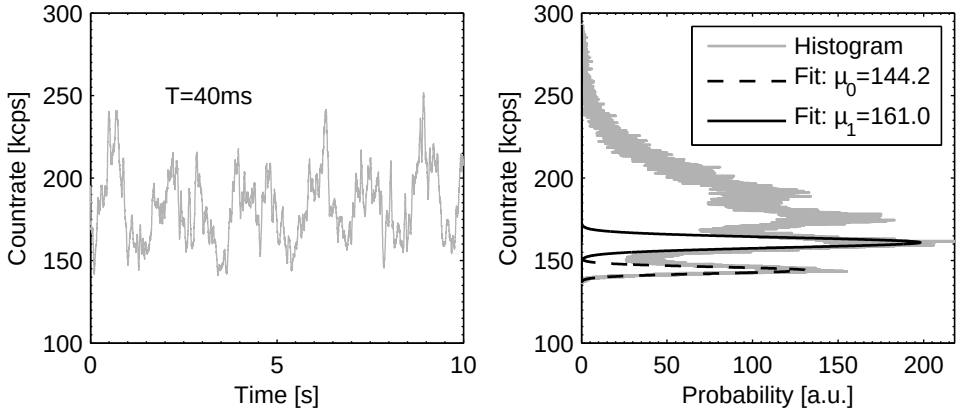

Figure 5.6.: Left-hand: Single atom fluorescence with an enriched ^{39}Ar sample. Again, only part of a longer run is shown. Right-hand: The histogram of the full run still demonstrates the stepwise increase of the photon count rate. However, this is only possible with much longer integration time. The derived ^{39}Ar photon count rate is 16.8 kcps. The underground in-between the peaks is again due to the integration.

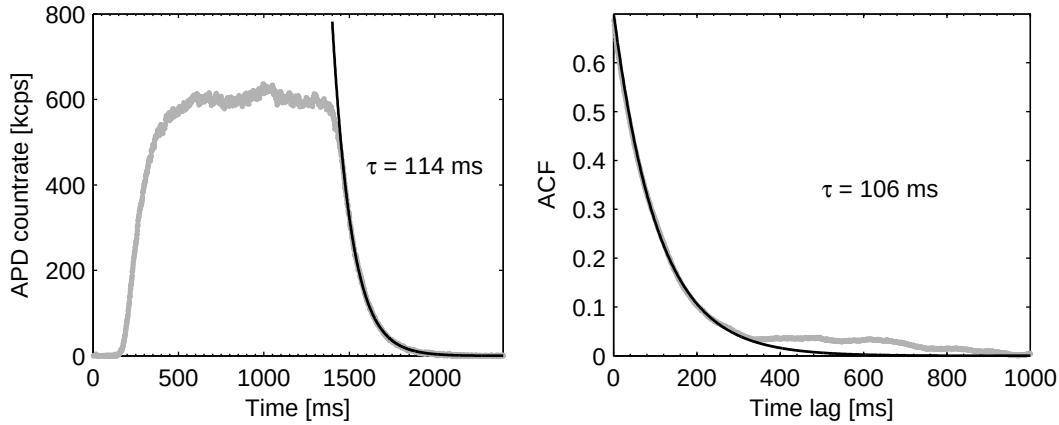

Figure 5.7.: Left-hand: Lifetime τ in a small MOT, source chamber pressure $p_1 = 1.4 \cdot 10^{-5}$ mbar. The lifetime is slightly too large due to the averaging process. This also leads to a small tail on the left slope. Right-hand: τ as inferred from the autocorrelation function (ACF) of single atom measurements. The position of the broad peak at $t = 400..800$ ms corresponds to the time lag between atoms. Altogether, the lifetime is rather short due to the previously discussed vacuum limitations.

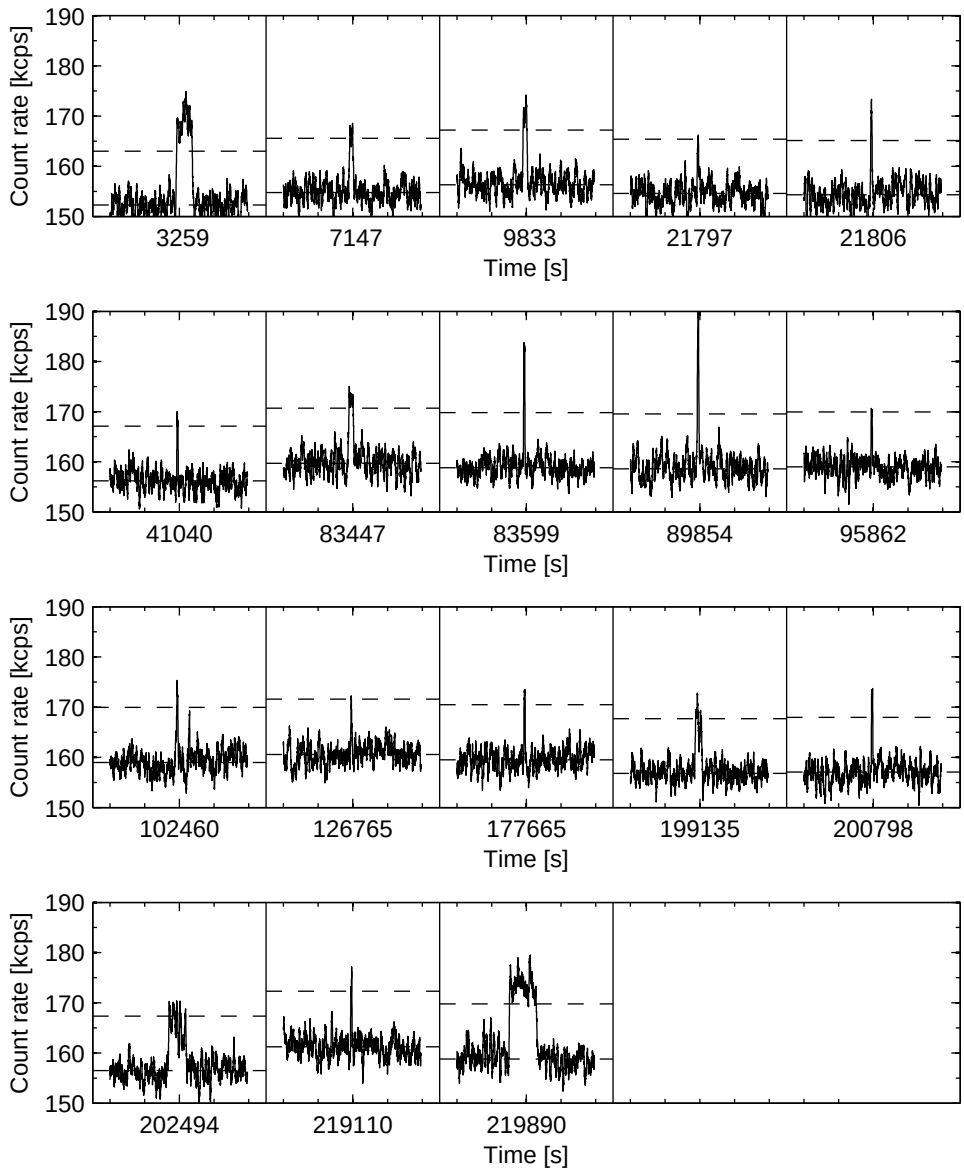

Figure 5.8.: Signal of single ^{39}Ar atoms in a sample of atmospheric argon. In total, 18 atoms were detected in 61 hours. The x-axis minor ticks indicate seconds as each frame corresponds to a 5 second window around a certain point of time. Horizontal lines indicate the background count rate and the 5.5σ threshold for 40 ms integration time.

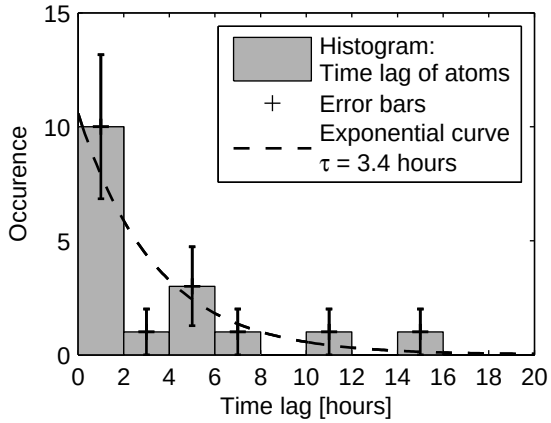

Figure 5.9.: Histogram of time lags between detected atoms. The exponential curve is motivated by the Poisson process of atoms entering the MOT and reproduces the histogram reasonably well.

This is justified by the underlying Poisson process. From R_{39} as above follows that the mean time lag between two atoms should be ≈ 3.4 h which is plugged into the exponential decay curve. The agreement is good considering the small number of detected atoms and supports the derived value of the atom count rate.

5.8. Recent (possible) improvements

5.8.1. Liquid nitrogen cooled source

The recent implementation of a liquid nitrogen (lN_2) cooled metastable atom source leads to an improvement by more than a factor of 2 in loading rate. The modified atomic beam source features an alumina (aluminum oxide ceramic) tube instead of the previously used glass tube. The tube is mounted in a stainless steel double-walled vessel that is directly cooled by lN_2. Alumina is advantageous due to the much better thermal conductivity compared to glass (about 30 times higher than for glass).
Two mechanisms have to be taken into consideration: Firstly, the atoms emitted from the source have a narrower transversal velocity distribution. Hence, the collimator can cool a larger fraction of the atoms.
Likewise the mean longitudinal velocity is reduced. Therefore, the Zeeman slower efficiency is increased and practically all atoms can be slowed down. Fig. 5.10 illustrates the effect of lN_2 cooling the source. The gain can be derived approximately from the maximum ratio of peak heights, as the width of a histogram peak is not affected by the increased loading rate and the probability for two atoms in the MOT is still low.

5.8.2. Additional collimator repumper sidebands

In order to further increase the loading rate additional repumper sidebands for the collimator are tested. Again, the possible improvement relies on different effects. On the one

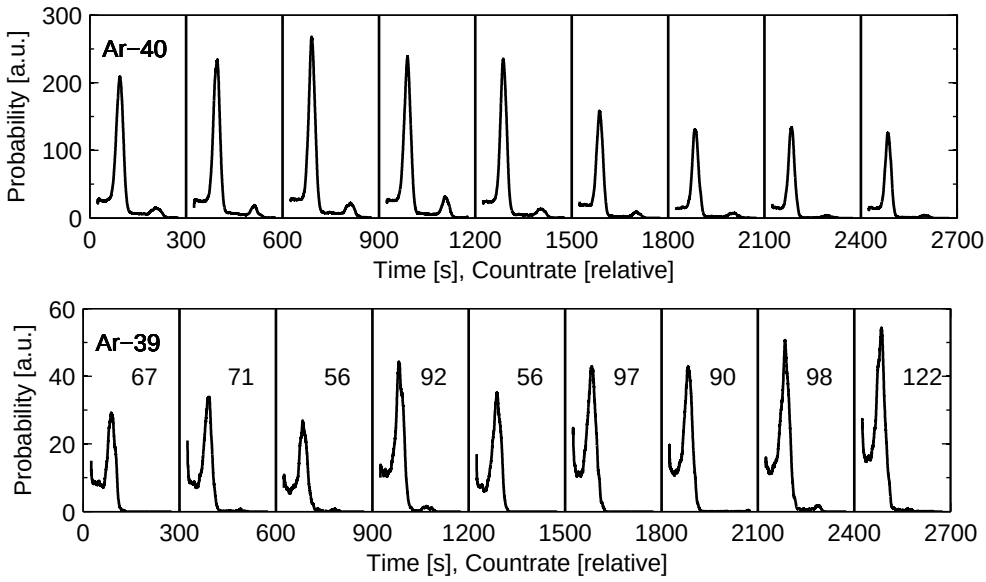

Figure 5.10.: Loading rate improvement with a liquid nitrogen cooled source. Each frame shows the histogram peaks for one and two atoms in the MOT, the background peak is omitted. Time intervals for each frame are given by the time on the x-axis. The upper time series is for ^{40}Ar where lN_2 cooling was switched off at $t = 900$ s. The bottom series represents ^{39}Ar measurements, the cooling was switched on at $t = 0$ s. Numbers in each subframe correspond to the manually counted number of detected atoms.

hand, the metastable atoms are initially distributed over all F states. Hence, pumping all the atoms from $F = \frac{9}{2}..\frac{3}{2}$ to $F = \frac{11}{2}$ should lead to a higher loading rate. On the other hand, as can be seen in fig. 3.3, the loss probability is especially high in the collimator due to the large saturation of the beams.
A summary of preliminary results for all repumper sidebands is provided in fig. 5.11. From fig. 3.3 it follows that practically no atoms should be found in $F = 11/2$ after the collimator ($\bar{t}_{coll} \approx 0.3$ ms) when no repumping light is applied. However, this is not reproduced by the measurement. It can be explained by optical pumping with the Zeeman slower beam. The ZSL first and second repumper light is resonant with repumper transitions of atoms with the mean longitudinal velocity. Hence, they can partially substitute the collimator repumpers. Still, the first and second collimator repumper lead to a gain in loading rate as they are optimized for repumping those atoms that are collimated.
The third and fourth repumper, however, do not yet yield satisfactory results, they even decrease the loading rate. The reason for this behavior has not yet been identified but the possibility of systematic errors due to instability of the repumper laser cannot be excluded. Another possibility lies in the laser setup. A FPI scan of the collimator tapered amplifier output reveals additional sidebands that may arise from interference between different spectral modes. These could well lead to undesired optical pumping to the wrong states and will therefore be investigated in the immediate future.

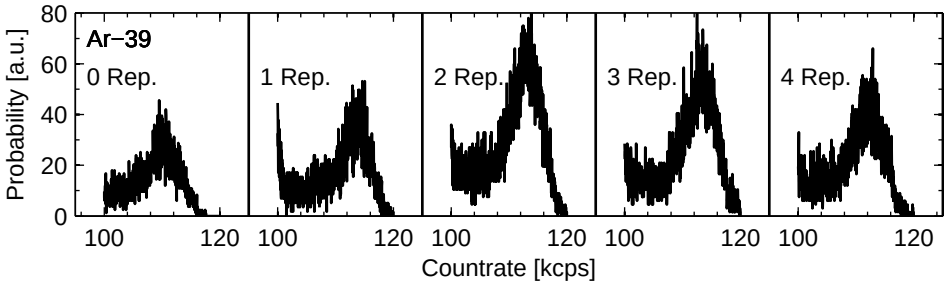

Figure 5.11.: Single atom histogram peaks for different number of repumper sidebands. The gain with the first two repumpers is about 2.5 while the third and fourth repumper decrease the loading rate. For explanation see text.

5.8.3. Enhanced signal quality

The single atom signal quality has recently been improved by -as already mentioned- painting the trap chamber with low-reflectance vacuum compatible paint. Previously, the photon background from stray light was about $150 - 160$ kcps. With the optimized trap chamber, it is currently as low as 65 kcps for identical experimental parameters.
Furthermore, the removal of the inverted magnetron vacuum gauge in the MOT pump chamber significantly decreased the offset magnetic field in the MOT region. This results in much more localized atoms and a single atom photon count rate of around 19 kcps for ^{39}Ar, see cover page.
Keeping in mind the results for detection probability and optimum integration time as depicted in fig. 5.3, integration times of around 10 ms should be sufficient for clear single atom identification. Likewise, the detection probability is increased by about 15 %.

6. Summary

6.1. Results achieved

In the course of this experimental work, an apparatus for counting individual metastable ^{39}Ar atoms has been realized. Prior to the actual detection of atoms, hyperfine spectroscopy of the designated optical transition for laser cooling and trapping has been successfully performed. The hyperfine coefficients and the isotope shift of the cooling transition $1s_5$-$2p_9$ have been obtained by fitting the theoretically expected hyperfine transitions with the observed spectrum.
Accordingly, a high power laser system with all sidebands necessary for highly efficient laser manipulation of ^{39}Ar has been designed and set up. This included calculations regarding the probability for losses due to optical pumping to different hyperfine states. Furthermore, tapered amplifier laser diodes have been employed to provide the optical power needed for efficient laser cooling.
A high-throughput atomic beam apparatus featuring a radio-frequency driven gas discharge for production of metastable argon atoms has been assembled. It employs multiple schemes for both transversal and longitudinal deceleration of the atomic beam, such as a collimation stage, a magneto-optical lens and a Zeeman slower.
The production of metastable atoms in the gas discharge source has been modeled by a two-step model. In the first step, the plasma parameters such as electron temperature and electron density are calculated for the special case of a pressure-gradient plasma. Based on these parameters, the production and emission of metastable argon atoms were computed in the second step of the model. This was done by solving the continuity equation for atoms moving along the cylindrical axis of the discharge tube.
Although the model is very simplified, the results show good agreement with experimental findings. Hence, it may serve for further improvement of the metastable production efficiency.
Likewise, extensive calculations and simulations of the transversal and longitudinal cooling stages have been performed. Accordingly, the corresponding experimental realizations have been optimized for highest efficiency.
The actual detection of ^{39}Ar was realized with a magneto-optical trap, into which atoms from the collimated intense beam of slow atoms are loaded. Single ^{39}Ar atoms in the trap have been unambiguously identified by fluorescence detection of photons scattered from the trapping beams.
The loading rate of atoms into the trap has been increased substantially by employing an additional near-resonant sideband of the Zeeman slower laser beam. This allows for higher final velocities of the Zeeman slower, effectively reducing the atomic beam divergence. At the same time, it extends the longitudinal velocity capture range of the magneto-optical trap. Furthermore, a basic one-dimensional calculation of atoms being loaded into the trap

has been carried out and clearly shows the advantages of the additional slowing frequency. In addition, the fluorescence background from ^{40}Ar atoms in the trap chamber was eliminated by optically pumping these atoms to the ground state. These two innovations permit simultaneous loading and detection of ^{39}Ar atoms, thus rendering the toggling scheme used in similar experiments unnecessary.
During a long time measurement over 62 hours with atmospheric argon, 18 ^{39}Ar atoms have been detected. In order to further improve identification of ^{39}Ar atoms, measures to reduce the stray light background in the chamber have been undertaken and yield a background photon count rate that is by more than a factor of 2 lower.
Recently, a liquid nitrogen cooled atomic beam source has been implemented. First measurements suggest that the ^{39}Ar loading rate is increased by at least a factor of 2.
The results from this work show that ^{39}Ar count rates of at least one atom per hour for recent argon are within reach. Ultimately, this would allow for ^{39}Ar-dating of small natural water samples with sample size well below 10 liters. Hence, radiometric age determination of oceanographic samples or even ice cores on time scales of 50 - 1000 years BP seems feasible.

6.2. Outlook

Although the apparatus performance is already very high, some issues are not yet resolved and several improvements may further increase the ^{39}Ar detection rate. In the following, these are briefly discussed and possible solutions are suggested.
The most important issue is that of argon outgassing from the apparatus. As mentioned earlier, isotopically enriched argon samples had to be used for optimization of the apparatus for ^{39}Ar detection. Currently, it is observed that the ^{39}Ar detection rate with an atmospheric sample increases during operation in recycling mode. In a first attempt to reduce outgassing, the inverted magnetron gauges were removed from the vacuum apparatus. This already decreased ^{39}Ar outgassing by about a factor of 10. However, this will hopefully be completely resolved in the near future. If ^{39}Ar is found to be emitted from the whole apparatus and not from a single contaminated vacuum part, the sample reservoir in the vacuum apparatus could simply be enlarged, thus leading to lower relative contaminations.
After solving this issue, the ^{39}Ar loading rate has to be improved. As mentioned above, the metastable source might be optimized by increasing the electron density close to source exit with an additional electrode. Although the source seems to operate close to its optimum pressure, further gain in loading rate might still be possible by higher throughput.
Additionally, admixture of heavy noble gases such as xenon could also boost the metastable production efficiency. In a recent publication of the ANL group, this was demonstrated for a spectroscopy cell, [134]. Still, the parameters for a metastable source are different and measurements remain to be done.
Currently, the collimator gain is by about a factor of 2 lower than the predicted value. Hence, this should be thoroughly investigated again as it bears potential gain.
Another open issue lies in the measurement of a blank sample. Ideally, a sample of very old argon would be recycled for several days and would not yield any ^{39}Ar counts. And, strictly speaking, as long as this has not been realized, the previously derived ^{39}Ar detec-

tion rate cannot be taken for certain.
At the moment, the fluorescence detection of single atoms is limited by three factors. Firstly, the stray light background from the trap beams should be further reduced. This could be achieved by highest-grade anti-reflection coated viewports. Secondly, a full Bayesian approach to single atom identification might lead to much better identification of atoms than the currently applied threshold criterion. Thirdly, the lifetime of atoms in the MOT should be increased. This can be done by further optimization of the vacuum conductances and the pumping stages. And, as the power dissipation in the MOT coils leads to an increased residual gas pressure in the MOT chamber, improved coils are necessary.
This would also allow for a steeper magnetic field gradient in the MOT and could thus lead to more localized atoms. Especially, the ^{39}Ar atoms could be better imaged onto the fiber end. This again would facilitate identification of individual atoms.

A. Constants

Table A.1.: Relevant physical constants as recommended by the "International Council for Science: Committee on Data for Science and Technology (CODATA)" [135]

Name	Symbol	Value	Unit
Atomic mass constant	m_u	$1.660538782(83) \cdot 10^{-27}$	kg
Atomic unit of mass	m_e	$9.10938215(45) \cdot 10^{-31}$	kg
Boltzmann constant	k_B	$1.3806504(24) \cdot 10^{-23}$	JK^{-1}
Speed of light in vacuum	c	299792458	m/s
Electric constant (permittivity)	ε_0	$8.854187817 \cdot 10^{-12}$	F m^{-1}
Magnetic constant (permeability)	μ_0	$12.566370614 \cdot 10^{-7}$	NA^2
Planck constant	h	$6.62606896(33) \cdot 10^{-34}$ $4.13566733(10) \cdot 10^{-15}$	Js eVs
Bohr magneton	μ_B	$927.400915(23) \cdot 10^{-26}$ $5.7883817555(79) \cdot 10^{-5}$	J/T eV/T
Wavelength $1s_5$-$2p_9$ (vacuum)	λ	811.7542	nm
Saturation intensity $1s_5$-$2p_9$	I_s	1.44	mW/cm^2
Linewidth $1s_5$-$2p_9$	γ Γ	5.85 $2\pi \cdot 5.85$	MHz MHz
Electrical resistivity copper	ρ_{Cu}	$1.68 \cdot 10^{-8}$	Ωm
Thermal conductivity copper	ρ_{Cu}	401	$W/m \cdot K$
Van der Waals radius argon	r_{Ar}	188	pm

Table A.2.: Compilation of relevant isotopes of argon, data taken from [42]. Dashes indicate unavailable data.

Isotope	Mass $[m_u]$	Nat. ab.	Nucl. spin I	μ_I $[\mu_N]$	$T_{1/2}$	Decay
^{35}Ar	34.975257	–	3/2	0.633	1.77 s	EC to ^{35}Cl
^{36}Ar	35.96754552	0.003365(30)	0	0	–	–
^{37}Ar	36.966776	–	3/2	1.15	35.0 d	EC to ^{37}Cl
^{38}Ar	37.9627325	0.000632(5)	0	0	–	–
^{39}Ar	38.962314	$8.5 \cdot 10^{-16}$	7/2	−1.3	268 y	β^- to ^{39}K
^{40}Ar	39.9623837	0.996003(30)	0	0	–	–
^{41}Ar	40.964501	–	7/2	–	1.82 h	β^- to ^{41}K
^{42}Ar	41.9650	–	0	0	33 y	β^- to ^{42}K
^{43}Ar	42.9657	–	–	–	5.4 m	β^- to ^{43}K
^{44}Ar	43.963650	–	0	0	11.87 m	β^- to ^{44}K

Table A.3.: Isotopic shifts for different argon isotopes and two transitions. Eq. (2.6) yields the shift of ^{39}Ar relative to ^{40}Ar and holds as the value for calculation from ^{36}Ar and ^{38}Ar is the same within the errors. The measured value agrees with the calculated value within errors.

Isotope	Transition	$\Delta\nu$ [MHz]	ref.
36-40	$1s_5 - 2p_6$	$-494.9 \pm .6$	[49]
38-40	$1s_5 - 2p_6$	$-229.5 \pm .4$	
39-40	$1s_5 - 2p_6$	-107.1 ± 7.0	
36-40	$1s_5 - 2p_9$	$-450.1 \pm .9$	[48]
38-40	$1s_5 - 2p_9$	-208.1 ± 1.5	
39-40	$1s_5 - 2p_9$	-97.4 ± 6.4	Eq.(2.6) for ^{36}Ar
39-40	$1s_5 - 2p_9$	-97.1 ± 6.4	Eq.(2.6) for ^{38}Ar
39-40	$1s_5 - 2p_9$	$-94.6 \pm .4$	This experiment

Table A.4.: Data for the hyperfine constants of the $1s_5$ and $2p_9$ levels of ^{39}Ar as estimated and measured experimentally. The larger errors on the B's result from eq. (2.4) being much less sensitive to B than to A. Statistical errors are given, due to the calibration with a FPI the additional relative systematical error of $1.1 \cdot 10^{-3}$ has to be minded.

	Estimation	This work	ANL [45]
A_s [MHz]	-286.1 ± 1.4[a]	$-285.9 \pm .14$	$-285.36 \pm .13$
B_s [MHz]	118 ± 20[a]	118.7 ± 1.5	117.8 ± 1.2
A_p [MHz]	-117 ± 20[b]	$-134.6 \pm .12$	-134.36 ± 0.08
B_p [MHz]	103 ± 10[c]	113.1 ± 1.8	113.1 ± 1.4

[a] see [49]: analysis using data from ^{37}Ar
[b] estimated from the hfs constants of ^{37}Ar
[c] estimated from the hfs constants of ^{21}Ne

B. Symbols

Table B.1.: Notation of symbols used throughout this thesis. As the nomenclature is inconsistent in several cases [136] was used as reference for these. Some duplications could not be avoided, but usually relate to very different topics. Dashes indicate dimensionless quantities

Symbol	Name	Typical units
A	Magnetic dipole hyperfine constant	MHz
B	Electric quadrupole hyperfine constant	MHz
C	Hyperfine constant C	–
V	Volume	m^3,l
l	Length	m
v	Velocity	m/s
r	Radius	m
R	Radius as distance from source	m
d	Diameter, Distance	m
A	Area	m^2
N	Number (of atoms)	–
t	Time	s
n	Number density	$1/m^3$
$\Delta\Omega$	Solid angle	sr
p	Pressure	N/m^2, mbar
T	Temperature	K
L	Conductance of vacuum tubing	L/s
S	Pumping speed	L/s, m^3/h
Q	Throughput, Flow	atoms/s
Φ	Flux	$\text{atoms} \cdot m^{-2}s^{-1}$
I	Electric current	A
U	Voltage	V
R	Electrical resistance	Ω
P	Power	W
m	Mass	kg

Table B.2.: Notation of symbols, continued

m	Magnetic quantum number	–
S	Spin quantum number	–
L	Orbital angular momentum q.n.	–
K	Intermediate coupling q.n.	–
J	Total electronic angular momentum q.n.	–
I	Nuclear magnetic moment q.n.	–
F	Total atomic angular momentum q.n.	–
$_{g,\ e}$	Subscript ground/excited state	–
$g_{S(L,K,J,F)}$	Landé g-factor	–
μ_{eff}	Effective magnetic moment	–
B	Magnetic field	T, Gauss
A'	Magnetic field gradient	T/m, Gauss/cm
Optical freq.	ν ω	Hz $2\pi \cdot$ Hz
Resonance freq.	ν_0 ω_0	Hz $2\pi \cdot$ Hz
Detuning	δ Δ	MHz $2\pi \cdot$ MHz
I	Intensity	$\mathrm{W/m^2}$, $\mathrm{mW/cm^2}$
λ	Mean free path	m
γ_p	Scattering rate	$\mathrm{s^{-1}}$
γ'	Power broadened linewidth	MHz
p	Probability density	$\frac{1}{\mathrm{MHz}}, \frac{1}{\mathrm{m/s}}$
I_0	Laser intensity at maximum	$\mathrm{W/m^2}$
R	Laser beam radius, 13.5% of I_0	m
w	Laser beam waist: $2\sigma \equiv R$	m
NA	Numerical aperture, 5% radius	–
R	Loading rate	Hz
γ	Background collisions rate	Hz
τ	Lifetime	s
β	Two-body loss coefficient	Hz

C. Formulae

Hyperfine formula [47]

$$\Delta E = \frac{A}{2}C + \frac{B}{4}\frac{\frac{3}{2}C(C+1) - 2I(I+1)J(J+1)}{I(2I-1)J(2J-1)} \tag{C.1}$$

Empiric relation for isotope shifts

$$\Delta\nu_{40}^{39}(1s_5 - 2p_9) = \frac{\Delta\nu_{40}^{iso}(1s_5 - 2p_9)}{\Delta\nu_{40}^{iso}(1s_5 - 2p_6)}\Delta\nu_{40}^{39}(1s_5 - 2p_6) \tag{C.2}$$

Normal isotope mass shift

$$\Delta\nu = \frac{m_e}{m_p} \cdot \frac{M_2 - M_1}{M_2 \cdot M_1} \tag{C.3}$$

Saturation intensity

$$I_s = \pi hc/(3\lambda^3\tau) \tag{C.4}$$

Saturation parameter

$$s = I_0/I_s \tag{C.5}$$

Doppler shift, velocity along direction of propagation

$$\Delta E_{Doppler} = -k \cdot v \cdot \hbar \tag{C.6}$$

Zeeman shift

$$\Delta E_{Zeeman} = \mu' \cdot B \tag{C.7}$$

Effective magnetic moment

$$\mu' = (m_e g_e - m_g g_g)\mu_B \tag{C.8}$$

Power broadened linewidth

$$\gamma' = \sqrt{1+s} \cdot \gamma \tag{C.9}$$

Photon scattering rate

$$\gamma_p = \frac{\Gamma}{2} \cdot \frac{s}{1 + s + (\frac{2\delta}{\gamma})^2} \tag{C.10}$$

Landé g-factors

$$g_S = 2.00231930436 \tag{C.11}$$

$$g_L = 1 \tag{C.12}$$

$$g_J = g_L \frac{J(J+1) - S(S+1) + L(L+1)}{2J(J+1)} + g_S \frac{J(J+1) + S(S+1) - L(L+1)}{2J(J+1)} \tag{C.13}$$

$$g_I = \mu_I / I \tag{C.14}$$

$$g_F = g_J \frac{F(F+1) - I(I+1) + J(J+1)}{2F(F+1)} + g_I \frac{F(F+1) + I(I+1) - J(J+1)}{2F(F+1)} \tag{C.15}$$

Doppler limited MOT temperature

$$T_D = \frac{\hbar\Gamma}{2k_B} \tag{C.16}$$

Recoil limit

$$T_r = \frac{(\hbar k)^2}{2k_B m} \tag{C.17}$$

Planck energy

$$E = h \cdot \nu = \hbar \cdot \omega \tag{C.18}$$

Gaussian distribution for variable x

$$p_{gauss}(x) = \frac{1}{\sqrt{2\pi}\sigma_x} \cdot e^{-\frac{(x-x_0)^2}{2\sigma_x^2}} \tag{C.19}$$

Maxwell-Boltzmann probability density in 3D

$$p_{MBD3}(x) = \sqrt{\frac{2}{\pi}} \left(\frac{m}{k_B T}\right)^{3/2} v^2 e^{-\frac{mv^2}{2k_B T}} \tag{C.20}$$

Maxwell-Boltzmann probability density in 1D

$$p_{MBD1}(x) = \sqrt{\frac{m}{2\pi k_B T}} e^{-\frac{mv^2}{2k_B T}} \tag{C.21}$$

Moments and characteristic parameters of above distributions for a thermal gas, velocity replaces variable x.

$$\sigma_v = \sqrt{\frac{k_B T}{m}},$$

$$\overline{v}_{MBD} := \langle v \rangle_{MBD} = \sqrt{\frac{8k_B T}{\pi m}},$$

$$\overline{v^2}_{MBD} := \left\langle v^2 \right\rangle_{MBD} = \sqrt{\frac{3k_BT}{m}},$$

$$\widehat{v}_{MBD} = \{v | p_{MBD}(v) = max(p_{MBD}(v))\} = \sqrt{\frac{2k_BT}{m}} \tag{C.22}$$

Lorentz curve, full-width-half-maximum γ, center at x'=t

$$p_{lor}(x) = \frac{1}{2\pi} \cdot \frac{\gamma}{(\gamma/2)^2 - (x-t)^2} \tag{C.23}$$

$$p_{voigt}(x) = \int_{-\infty}^{\infty} p_{gauss}(x) \cdot p_{lor}(x - x')dx' \tag{C.24}$$

Mean free path in thermal gas

$$\lambda = \frac{1}{n \cdot \sigma} = \frac{1}{n \cdot \sqrt{2}\pi \cdot (2r_{Ar})^2} = \frac{k_BT}{p \cdot \sqrt{2}\pi \cdot (2r_{Ar})^2} \tag{C.25}$$

Biot-Savart law

$$\mathbf{B} = \int \frac{\mu_0}{4\pi} \frac{I \mathrm{d}\mathbf{I} \times \mathrm{d}\hat{\mathbf{r}}}{|r|^2} \tag{C.26}$$

Bibliography

[1] H.H. Loosli and H. Oeschger. Detection of ^{39}Ar in atmospheric argon. *Earth and Planetary Science Letters*, 5:191 – 198, 1968.

[2] C. Y. Chen, Y. M. Li, K. Bailey, T. P. O'Connor, L. Young, and Z.-T. Lu. Ultrasensitive Isotope Trace Analyses with a Magneto-Optical Trap. *Science*, 286(5442):1139–1141, 1999.

[3] H.H. Loosli, M. Möll, H. Oeschger, and U. Schotterer. Ten years low-level counting in the underground laboratory in Bern, Switzerland. *Nuclear Instruments and Methods in Physics Research Section B: Beam Interactions with Materials and Atoms*, 17(5-6):402 – 405, 1986.

[4] Intergovernmental Panel on Climate Change. Fourth Assessment Report: Climate Change. Technical report, IPCC, 2007.

[5] World Water Assessment Programme. 3rd United Nations World Water Development Report: Water in a Changing World. Technical report, UNESCO, 2003.

[6] W.S. Broecker and T.H. Peng. *Tracers in the Sea*. Eldigio Pr.

[7] W. Aeschbach-Hertig. private communication. please contact for details, 2006-2011.

[8] W. Aeschbach-Hertig. Physics of Aquatic Systems II, lecture notes, 2009.

[9] Ph. Collon, M. Bichler, J. Caggiano, L. Dewayne Cecil, Y. El Masri, R. Golser, C. L. Jiang, A. Heinz, D. Henderson, W. Kutschera, B. E. Lehmann, P. Leleux, H. H. Loosli, R. C. Pardo, M. Paul, K. E. Rehm, P. Schlosser, R. H. Scott, W. M. Smethie, and R. Vondrasek. Development of an AMS method to study oceanic circulation characteristics using cosmogenic ^{39}Ar. *Nuclear Instruments and Methods in Physics Research Section B: Beam Interactions with Materials and Atoms*, 223:428 – 434, 2004. Proceedings of the Ninth International Conference on Accelerator Mass Spectrometry.

[10] H.H. Loosli and H. Oeschger. ^{39}Ar, ^{14}C and ^{85}Kr measurements in groundwater samples. *IAEA Vienna: Isotope Hydrology*, 2:931, 1978.

[11] H.H. Loosli. A dating method with ^{39}Ar. *Earth and Planetary Science Letters*, 63(1):51 – 62, 1983.

[12] I. D. Moore, K. Bailey, J. Greene, Z.-T. Lu, P. Müller, T. P. O'Connor, Ch. Geppert, K. D. A. Wendt, and L. Young. Counting Individual ^{41}Ca Atoms with a Magneto-Optical Trap. *Phys. Rev. Lett.*, 92(15):153002, 2004.

[13] S. Hoekstra, A. K. Mollema, R. Morgenstern, H. W. Wilschut, and R. Hoekstra. Single-atom detection of calcium isotopes by atom-trap trace analysis. *Phys. Rev. A*, 71(2):023409, Feb 2005.

[14] W. Jiang, W. Williams, K. Bailey, A. M. Davis, S.-M. Hu, Z.-T. Lu, T. P. O'Connor, R. Purtschert, N. C. Sturchio, Y. R. Sun, and P. Mueller. ^{39}Ar Detection at the 10^{-16} Isotopic Abundance Level with Atom Trap Trace Analysis. *Phys. Rev. Lett.*, 106(10):103001, Mar 2011.

[15] P. Schlosser, M. Stute, H. Dorr, C. Sonntag, and K.O. Munnich. Tritium/^{3}He dating of shallow groundwater. *Earth and Planetary Science Letters*, 89:353, 1988.

[16] V.N. Nijampurkar, B.S. Amin, D.P. Kharkar, F. Oldfield, and D. Lal. Dating groundwaters of ages younger than 1000-1500 years using natural Silicon-32. *Nature*, 210:478, 1966.

[17] H.B. Clausen. Dating of polar ice by ^{32}Si. *Journal of Glaciology*, 12:411, 1973.

[18] V.N. Nijampurkar, D.K. Rao, F. Oldfield, and I. Renberg. The half-life of ^{32}Si: a new estimate based on varved lake sediments. *Earth and Planetary Science Letters*, 163:191, 1998.

[19] L.K. Fifield and U. Morgenstern. Silicon-32 as a tool for dating the recent past. *Quarternary Geochronology*, 4:400, 2009.

[20] E. Mazor. Paleotemperatures and other hydrological parameters deduced from gases dissolved in groundwaters, Jordan Rift Valley, Israel. *Geochem. Cosmochim. Acta*, 36:1321, 1972.

[21] U. Beyerle, R. Purtschert, W. Aeschbach-Hertig, D. Imboden, H. Loosli, R. Wieler, and R. Kipfer. Climate and groundwater recharge during the last glaciation in an ice-covered region. *Science*, 282:731, 1998.

[22] J. A. Corcho Alvarado, R. R. Purtschert, F. Barbecot, C. Chabault, J. Rueedi, V. Schneider, W. Aeschbach-Hertig, R. Kipfer, and H. H. Loosli. Constraining the age distribution of highly mixed groundwater using ^{39}Ar: A multiple environmental tracer (^{3}H/^{3}He, ^{85}Kr, ^{39}Ar, and ^{14}C) study in the semiconfined Fontainebleau Sands Aquifer (France). *Water Resour. Res.*, 43, 2007.

[23] J. A. Corcho Alvarado, Barbecot, R. Purtschert, M. Gillon, W. Aeschbach-Hertig, and R. Kipfer. European climate variations over the past half-millennium reconstructed from groundwater. *Geophys. Res. Lett.*, in press, 2009.

[24] T. Kluge, T. Marx, D. Scholz, S. Niggemann, A. Mangini, and W. Aeschbach-Hertig. A new tool for palaeoclimate reconstruction: Noble gas temperatures from fluid inclusions in speleothems. *Earth and Planetary Science Letters*, 269:408, 2008.

[25] C.C. Jr. Langway and B.L. Hansen. Drilling through the ice cap: Probing climate for a thousand centuries. *Bulletin of the Atomic Scientists*, page 62, 1970.

[26] U. Morgenstern, C.B. Taylor, Y. Parrat, H.W. Gäggeler, and B. Eichler. ^{32}Si in precipitation: evaluation of temporal and spatial variation. *Earth and Planetary Science Letters*, 144:289, 1996.

[27] H. H. Loosli. ^{39}Ar: A tool to investigate ocean water circulation and mixing. *Handbook of Environmental Isotope Chemistry*, 3:385 – 392, 1989.

[28] W.S. Broecker and T.-H. Peng. Comparison of ^{39}Ar and ^{14}C for waters in the deep ocean. *Nucl. Instr. and Meth. in Phys. B*, 172:473, 2000.

[29] E. Nolte, W. Rühm, H.H. Loosli, I. Tolstikhin, K. Kato, T.C. Huber, and S.D. Egbert. Measurements of fast neutrons in Hiroshima by use of ^{39}Ar. *Radiat. Environ. Biophys.*, 44:261, 2006.

[30] D. Acosta-Kane et al. Discovery of underground argon with low level of radioactive ^{39}Ar and possible applications to WIMP dark matter detectors. *Nuclear Instruments and Methods in Physics Research A*, 587:46, 2008.

[31] Lord Rayleigh and W. Ramsay. Argon, a new constituent of the atmosphere. *Proc. R. Soc. Lond.*, 57(6):265–287, 1894.

[32] W.G. Mook. Environmental Isotopes in the Hydrological Cycle: Principles and Applications. Technical report, Centre for Isotope Research, Groningen, 2001.

[33] E. Kierig. *AC-Control of Single Particle Tunneling*. PhD thesis, Faculty of Physics and Astronomy, University of Heidelberg, 2008.

[34] J. Tomkovič, M. Schreiber, J. Welte, M. Kiffner, J. Schmiedmayer, and M.K. Oberthaler. Single spontaneous photon as a coherent beamsplitter for an atomic matter-wave. *Nature Physics*, 7:379, 2011.

[35] R. Stützle, D. Jürgens, A. Habenicht, and M.K. Oberthaler. Dissipative light masks for atomic nanofabrication. *Journal of Optics B*, 5:S164, 2003.

[36] R. Stützle, M.C. Göbel, Th. Hörner, E. Kierig, I. Mourachko, M.K. Oberthaler, M.A. Efremov, M.V. Fedorov, V.P. Yakovlev, K.A.H. van Leeuwen, and W.P. Schleich. Observation of nonspreading wave packets in an imaginary potential. *Phys.Rev.Lett.*, 95:110405, 2005.

[37] F. Haupert. *A Moiré-Deflectometer for AEgIS*. PhD thesis, Faculty of Physics and Astronomy, University of Heidelberg, 2011.

[38] D. Schneble. *Trapping and Manipulation of Laser-Cooled Metastable Argon Atoms at a Surface*. PhD thesis, Faculty of Mathematics and Physics, University of Stuttgart, 2002.

[39] J. Welte. Single Atom Detection By Fluorescence. Master's thesis, Faculty of Physics and Astronomy, University of Heidelberg, 2007.

[40] M. Schreiber. Experimentelle Realisierung eines Delayed Choice Experiments mit metastabilen Argonatomen. Master's thesis, Faculty of Physics and Astronomy, University of Heidelberg, 2008.

[41] R. W. Stoenner, O. A. Schaeffer, and S. Katcoff. Half-Lives of Argon-37, Argon-39, and Argon-42. *Science*, 148(3675):1325–1328, 1965.

[42] Webelements.com. http://www.webelements.com/argon/isotopes.html, 2010.

[43] G. A. Hebner. Spatially resolved, excited state densities and neutral and ion temperatures in inductively coupled argon plasmas. *Journal of Applied Physics*, 80(5):2624–2636, 1996.

[44] J. Welte, I. Steinke, M. Henrich, F. Ritterbusch, M. K. Oberthaler, W. Aeschbach-Hertig, W. H. Schwarz, and M. Trieloff. Hyperfine spectroscopy of the $1s_5 - 2p_9$ transition of ^{39}Ar. *Review of Scientific Instruments*, 80(11):113109, 2009.

[45] W. Williams, Z.-T. Lu, K. Rudinger, C.-Y. Xu, R. Yokochi, and P. Müller. Spectroscopic study of the cycling transition $4s[3/2]_2 - 4p[5/2]_3$ at 811.8 nm in ^{39}Ar: Hyperfine structure and isotope shift. *Phys. Rev. A*, 83:012512, 2011.

[46] I. Steinke. Hyperfine spectroscopy of the $1s_5 - 2p_9$ transition in ^{39}Ar. Master's thesis, Faculty of Physics and Astronomy, University of Heidelberg, 2009.

[47] H. Kopfermann. *Kernmomente*. Akadem. Verl.-Ges., Frankfurt am Main, 1956.

[48] G. D'Amico, G. Pesce, and A. Sasso. Field shift analysis of visible and near infrared argon transitions. *J. Opt. Soc. Am. B*, 16(7):1033–1038, 1999.

[49] A. Klein, B.A. Brown, U. Georg, M. Keim, E Lievens, R. Neugart, M. Neuroth, R.E. Silverans, L. Vermeeren, and ISOLDE. Moments and mean square charge radii of short-lived argon isotopes. *Nuclear Physics A*, 607(7):1–22, 1996.

[50] W. Traub, F. L. Roesler, M. M. Robertson, and V. W. Cohen. Spectroscopic Measurement of the Nuclear Spin and Magnetic Moment of ^{39}Ar. *J. Opt. Soc. Am.*, 57(12):1452–1458, 1967.

[51] M.M. Robertson and J.E. Mack. Nuclear Spin and Magnetic Moment of ^{37}Ar. *Physical Review*, 140(4B):B820, 1965.

[52] X. Husson and J. P. Grandin. Hyperfine structures in the $2p^5 3p$ configuration of ^{21}Ne. *Journal of Physics B*, 11:1393–1398, April 1978.

[53] R.-J. Champeau and J.-C. Keller. Isotope shift of ^{20}Ne, ^{21}Ne and ^{22}Ne and hyperfine structure of ^{21}Ne in the lines 6096 Å and 6074 Å of neon I. *Journal of Physics B*, 6(4):L76–L79, 1973.

[54] T. W. Ducas, M. S. Feld, Jr. L. W. Ryan, N. Skribanowitz, and A. Javan. Hyperfine Structure of Excited States and Quadrupole Moment of ^{21}Ne Using Laser-Induced Line-Narrowing Techniques. *Phys. Rev. A*, 5(1):1036–1043, 1972.

[55] L. Julien, M. Pinard, and F. Lalo. Hyperfine structure and isotope shift of the 640.2 and 626.6 nm lines of neon. *J. Physique Lett.*, 41(1):479–482, 1980.

[56] G. M. Grosof, P. Buck, W. Lichten, and I. I. Rabi. Quadrupole Moment of ^{21}Ne. *Phys. Rev. Lett.*, 1(6):214–215, Sep 1958.

[57] S. Liberman. Étude empirique des configurations basses de ne i et de la structure hyperfine du neon 21. *Physica*, 69(2):598 – 610, 1973.

[58] J. C. Hess and H. J. Lippolt. Compilation of K/Ar measurements on HD-B1 standard biotite. *Bull. Liais. Inform. IUGS Subcom. Geochronol., Paris*, 12:19–23, 1994.

[59] W.H. Schwarz and M. Trieloff. Intercalibration of ^{40}Ar-^{39}Ar age standards NL25, HB3gr hornblendes, GA-1550, SB-3, HD-B1 biotite and BMus/2 muscovite. *Chem. Geol.*, 241:218, 2007.

[60] C.I. Sukenik and H.C. Busch. A rf discharge cell for saturated absorption spectroscopy of metastable argon. *Rev. Sci. Instrum.*, 73:493, 2002.

[61] X. Du, K. Bailey, Z.-T. Lu, P. Mueller, T. P. O'Connor, and L. Young. An atom trap system for practical ^{81}Kr dating. *Review of Scientific Instruments*, 75(10):3224–3232, 2004.

[62] G. Camy, D. Pineaud, N. Courtier, and Hu Chi Chuan. Recent developments in high resolution saturation spectroscopy obtained by means of acousto-optic modulators. *Revue de Physique Appliquee*, 17:357, 1982.

[63] S. Laue, M. Schüler, and H. Westphal. *private communication and "Die Oszillatoren 50..70MHz und 140 MHz", Abschlussbericht Mixed Signal Baugruppen*, 2006.

[64] H. J. Metcalf and P. van der Straten. *Laser cooling and trapping.* Springer, New York ; Berlin ; Heidelberg [u.a.], 1999.

[65] M. Henrich. Design and Realization of a Laser System for ATTA of ^{39}Ar. Master's thesis, Faculty of Physics and Astronomy, University of Heidelberg, 2010.

[66] C. Kaup. Single-Atom Detection of ^{39}Ar. Master's thesis, Faculty of Physics and Astronomy, University of Heidelberg, 2011.

[67] J. Welte, F. Ritterbusch, I. Steinke, M. Henrich, W. Aeschbach-Hertig, and M. K. Oberthaler. Toward the realization of atom trap trace analysis for ^{39}Ar. *New Journal of Physics*, 2010.

[68] J. M. Weber, K. Hansen, M. W. Ruf, and H. Hotop. Penning ionization of C_{60} and C_{70}. *Chemical Physics*, 239(1-3):271 – 286, 1998.

[69] H. Hotop. private communication.

[70] B. Brutschy and H. Haberland. A high-intensity beam of metastable helium atoms with good velocity resolution. *Journal of Physics E: Scientific Instruments*, 10:90–94, 1976.

[71] M. DeKieviet, M. Durr, S. Epp, F. Lang, and M. Theis. Source for atomic beams of metastable gases: Design and performance. *Review of Scientific Instruments*, 75(2):345–348, 2004.

[72] J. Kawanaka, M. Hagiuda, K. Shimizu, F. Shimizu, and H. Takuma. Generation of an intense low-velocity metastable-neon atomic beam. *Applied Physics B: Lasers and Optics*, 56:21–24, January 1993.

[73] Y. Ding, K. Bailey, A. M. Davis, S.-M. Hu, Z.-T. Lu, and T. P. O'Connor. Beam of metastable krypton atoms extracted from a microwave-driven discharge. *Review of Scientific Instruments*, 77(12):126105, 2006.

[74] Y. Ding, S.-M. Hu, K. Bailey, A. M. Davis, R. W. Dunford, Z.-T. Lu, T. P. O'Connor, and L. Young. Thermal beam of metastable krypton atoms produced by optical excitation. *Review of Scientific Instruments*, 78(2):023103, 2007.

[75] C. Y. Chen, K. Bailey, Y. M. Li, T. P. O'Connor, Z.-T. Lu, X. Du, L. Young, and G. Winkler. Beam of metastable krypton atoms extracted from a rf-driven discharge. *Review of Scientific Instruments*, 72(1):271–272, 2001.

[76] L. Young, D. Yang, and R. W. Dunford. Optical production of metastable krypton. *Journal of Physics B: Atomic, Molecular and Optical Physics*, 35(13):2985–2992, 2002.

[77] Alkor. http://www.alkor.net/LiF.html, 2011.

[78] F. Grüner, S. Becker, U. Schramm, T. Eichner, M. Fuchs, R. Weingartner, D. Habs, J. Meyer-Ter-Vehn, M. Geissler, M. Ferrario, L. Serafini, B. Van der Geer, H. Backe, W. Lauth, and S. Reiche. Design considerations for table-top, laser-based VUV and X-ray free electron lasers. *Appl. Phys. B*, 86:431, 2007.

[79] H. Daerr, M. Kohler, P. Sahling, S. Tippenhauer, A. Arabi-Hashemi, C. Becker, K. Sengstock, and M.B. Kalinowski. A novel vacuum ultra violet lamp for metastable rare gas experiments. *Rev. Sci. Instrum.*, 82:073106, 2011.

[80] A. Krischke. *Rothammels Antennenbuch*. DARC Verlag, 2001.

[81] C. Coleman. *An Introduction to Radio Frequency Engineering*. Cambridge University Press, 2001.

[82] P.M. Evjen. Application Note AN003: SRD Antennas. Technical report, Chipcon AS, 2001.

[83] M.A. Lieberman and A.J. Lichtenberg. *Principles of plasma discharges and materials processing*. John Wiley & Sons, Inc., 1994.

[84] M. A. Lieberman. A mini-course on the principles of plasma discharges, 2003.

[85] D. Leonhardt, C.R. Jr. Eddy, V.A. Shamamian, R.F. Fernsler, and J.E. Butler. Argon metastables in a high density processing plasma. *Journal of Applied Physics*, 83:2971, 1998.

[86] H. Hirata, M. Tadokoro, N. Nakano, Z.L. Petrovic, and T. Makabe. Two-Dimensional Images of Radiative and Metastable Excited State Radial Profiles for an Inductively Coupled Plasma in Argon. *IEEE Transactions on Plasma Physics*, 27:50, 1999.

[87] A. Bogaerts and R. Gijbels. Modeling of metastable argon atoms in a direct-current glow discharge. *Physical Review A*, 52:3743, 1995.

[88] M. Roberto. Effect of the argon metastable quenching by ionization reactions in an RF argon discharge. *Brazilian Review of Vacuum Applications*, 21:1, 2002.

[89] C.M. Ferreira, J. Loureiro, and A. Ricard. Populations in the metastable and the resonance levels of argon and stepwise ionization effects in a low-pressure argon positive column. *J. Appl. Phys.*, 57:82, 1985.

[90] S. Rauf and M.J. Kushner. Argon metastable densities in radio frequency Ar, Ar/O_2 and Ar/CF_4 electrical discharges. *J. Appl. Phys.*, 82:2805, 1997.

[91] G.R. Scheller, R.A. Gottscho, D.B. Graves, and T. Intrator. Quenching rates of Ar metastables in radio frequency glow discharges. *J. Appl. Phys.*, 64, 1988.

[92] C. Penache, M. Miclea, A. Bräuning-Demian, O. Hohn, S. Schössler, T. Jahnke, K. Niemax, and H. Schmidt-Böcking. Characterization of a high-pressure microdischarge using diode laser atomic absorption spectroscopy. *Plasma Sources Sci. Technol.*, 11:476, 2002.

[93] W. Wieme and J. Lenaerts. Diffusion of metastable atoms in rare gases. *Physica*, 98:229, 1980.

[94] S. Chapman and T.G. Gowling. *The Mathematical theory of non-uniform gases.* Cambridge Univ. Pr., Cambridge.

[95] G. A. Hebner and P. A. Miller. Behavior of excited argon atoms in inductively driven plasmas. *Journal of Applied Physics*, 87(12):8304–8315, 2000.

[96] C.M. Ferreira and J. Loureiro. Electron transport parameters and excitation rates in argon. *J. Phys. D: Appl. Phys.*, 16:1611–1621, 1983.

[97] D.M. Lymberopoulos and D.J. Economou. Fluid simulations of glow discharges: Effect of metastable atoms in argon. *J. Appl. Phys.*, 73:3668, 1993.

[98] N.L. Bassett and D.J. Economou. Effect of Cl_2 additions to an argon glow discharge. *J. Appl. Phys.*, 75:1931, 1994.

[99] W.L. Borst. Excitation of metastable argon and helium atoms by electron impact. *Physical Review A*, 9(3):1195–1200, 1974.

[100] N.J. Mason and W.R. Newell. Total cross sections for metastable excitation in the rare gases. *J. Phys. B*, 20:1357, 1987.

[101] E.V. Karoulina and Y.A. Lebedev. Computer simulation of microwave and DC plasmas: comparative characterisation of plasmas. *J. Phys. D: Appl. Phys*, 25:401, 1992.

[102] A.V. Phelps and J.P. Molnar. Lifetimes of Metastable States of Noble Gases. *Physical Review*, 89:1202, 1953.

[103] H.A. Hyman. Electron-impact excitation of metastable argon and krypton. *Physical Review A*, 18:441, 1978.

[104] H.A. Hyman. Electron-impact ionization cross sections for excited states of the rare gases (Ne, Ar, Kr, Xe), cadmium, and mercury. *Physical Review A*, 20:855, 1979.

[105] NIST. CODATA Internationally recommended values of the Fundamental Physical Constants. Technical report, NIST, 2010.

[106] K. Bartschat and V. Zeman. Electron-impact excitation from the $3p^5 4s$ metastable states of argon. *Physical Review A*, 59:2552, 1999.

[107] F. Ritterbusch. Realization of a collimated beam of metastable atoms for ATTA of ^{39}Ar. Master's thesis, Faculty of Physics and Astronomy, University of Heidelberg, 2009.

[108] P. Meystre. *Atom optics*. Springer, New York ; Berlin ; Heidelberg [u.a.], 2001.

[109] D. A. Steck. Rubidium 87 D Line Data. Technical report, Oregon Center for Optics and Department of Physics, University of Oregon, 2001.

[110] A. Aspect, N. Vansteenkiste, and R. Kaiser. Preparation of a pure intense beam of metastable helium by laser cooling. *Chemical Physics*, 145:307–315, 1990.

[111] M. Störzer. Realisierung eines langsamen, intensiven Strahls metastabiler Argonatome. Master's thesis, Universität Konstanz, Fachbereich Physik, 1993.

[112] R. Gaggl, L. Windholz, and C. Neureiter. Laser-Cooling of a Sodium Atomic Beam by Means of Strong Electric Fields. *Laser Physics*, 4(5):866–871, 1994.

[113] Strohmeier, P. and Kersebom, T. and Krüger, E. Na-atom beam deceleration by a mode-locked laser. *Opt. Commun.*, 73:451, 1989.

[114] W. D. Phillips, J. V. Prodan, and H. J. Metcalf. Laser cooling and electromagnetic trapping of neutral atoms. *JOSA B*, 2(11):1751–1767, 1985.

[115] W. Ertmer, R. Blatt, J. L. Hall, and M. Zhu. Laser Manipulation of Atomic Beam Velocities: Demonstration of Stopped Atoms and Velocity Reversal. *Phys. Rev. Lett.*, 54(10):996–999, Mar 1985.

[116] R. Blatt, W. Ertmer, P. Zoller, and J. L. Hall. Atomic-beam cooling: A simulation approach. *Phys. Rev. A*, 34(4):3022–3033, Oct 1986.

[117] C. C. Bradley, J. G. Story, J. J. Tollett, J. Chen, N. W. M. Ritchie, and R. G. Hulet. Laser cooling of lithium using relay chirp cooling. *Optics Letters*, 17(5):349–351, 1992.

[118] W. D. Phillips and H. Metcalf. Laser Deceleration of an Atomic Beam. *Phys. Rev. Lett.*, 48(9):596–599, Mar 1982.

[119] S.K. Mayer, N.S. Minarik, M.H. Shroyer, and D.H. Mclntyre. Zeeman-tuned slowing of rubidium using σ^+ and σ^- polarized light. *Optics Communications*, 210(3-6):259 – 270, 2002.

[120] T. E. Barrett, S.l W. Dapore-Schwartz, M. D. Ray, and G. P. Lafyatis. Slowing atoms with $\sigma-$ polarized light. *Phys. Rev. Lett.*, 67(25):3483–3486, Dec 1991.

[121] Y. B. Ovchinnikov. A Zeeman slower based on magnetic dipoles. *Optics Communications*, 276(2):261 – 267, 2007.

[122] P. N. Melentiev, P. A. Borisov, and V. I. Balykin. Zeeman Laser Cooling of ^{85}Rb Atoms in Transverse Magnetic Field. *Journal of Experimental and Theoretical Physics*, 98(4):667–677, 2004.

[123] C. J. Foot. *Atomic physics*. Number 7 : Atomic, optical, and laser physics in Oxford master series in physics ; 7 : Atomic, optical, and laser physics ; Oxford master series in physics. Oxford University Press, Oxford [u.a.], 1. publ. edition, 2005.

[124] K.J. Matherson, R.D. Glover, D.E. Laban, and R.T. Sang. Absolute metastable atom-atom collision cross section measurement using a magneto-optical trap. *Rev. Sci. Instr.*, 78:073102, 2007.

[125] L.W.G. Steenhuijsen. Investigations on Afterglows of Neon Gas Discharges. *Beitr. Plasmphys.*, 21:301, 1980.

[126] H. Filter. Methoden zur Flussbestimmung von metastabilen Argonatomen. Master's thesis, Faculty of Physics and Astronomy, University of Heidelberg, 2011.

[127] G.W. Greenslees, D.L. Clark, S.L. Kaufman, D.A. Lewis, J.F. Tonn, and J.H. Broadhurst. High resolution laser spectroscopy with minute samples. *Opt. Commun.*, 23:236, 1977.

[128] V.I. Balykin, V.S. Letokhov, V.I. Mishin, and V.A. Semchishen. Laser fluorescence detection of single atoms. *Pis'ma Zh. Eksp. Teor. Fiz.*, 26:492, 1977.

[129] V.I. Balykin, G.I. Bekov, V.S. Letokhov, and V.I. Mishin. Laser detection of single atoms. *Sov. Phys. Usp.*, 23:651, 1980.

[130] V.I. Balykin, V.S. Letokhov, and V.I. Mishin. Multi-Photoelectron Fluorescence Selective Detection of Single Atoms by Laser Radiation. *Appl. Phys.*, 22:245–250, 1980.

[131] R.D. LaBelle, C.S. Hansen, M.M. Mankowski, and W.M.Jr. Fairbank. Isotopically selective atom counting using photon burst detection. *Phys. Rev. A*, 54:4461, 1996.

[132] W.M.Jr. Fairbank. Photon burst mass spectrometry. *Nuclear Instruments and Methods in Physics Research B*, 29:407, 1987.

[133] V.S. Letokhov, V.G. Minogin, and B.D. Pavlik. Cooling and trapping of atoms and molecules by a resonant light field. *Sov. Phys. JETP*, 5, 1977.

[134] K. Rudinger, Z.-T. Lu, and P. Mueller. The role of carrier gases in the production of metastable argon atoms in a rf discharge. *Review of Scientific Instruments*, 80(3):036105, 2009.

[135] NIST. NIST Atomic Spectra Database. Technical report, NIST, 2010.

[136] Wolframalpha.com. http://www.wolframalpha.com, 2010.